WARWICK
THE UNIVERSITY OF WARWICK

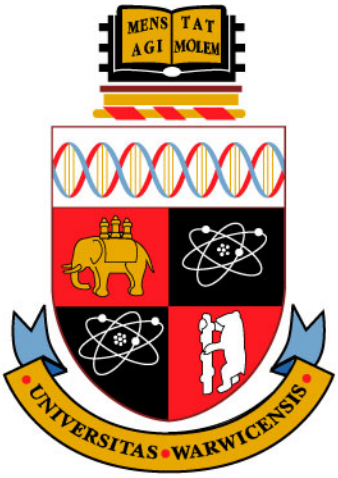

In-Situ Lithium-ion Battery Power Line Communication with Quadrature Amplitude Modulation

by

Mahyar Jafari Koshkouei

Thesis submitted in partial fulfilment of the requirements
for the degree of
Doctor of Philosophy in Engineering

WMG
The University of Warwick

December 2022

Contents

List of Figures

List of Tables

List of Abbreviations

AC	Alternating current
AGC	Automatic gain control
API	Application programming interface
ARQ	Automatic Repeat Request
ASK	Amplitude shift keying
AWGN	Additive white gaussian noise
BER	Bit error ratio
BEV	Battery electric vehicle
BMS	Battery management system
BPSK	Binary phase shift keying
C-rate	Charge rate
CAN bus	Controller area network
CMS	Cell management system
DC	Direct current
DDM	Data-driven model

ECC	Error Correcting Code
ECM	Equivalent circuit model
EIS	Electrochemical impedance spectroscopy
EMI	Electromagnetic interference
EVM	Error vector magnitude
FDMA	Frequency division multiple access
FSK	Frequency Shift Keying
FSPL	Free-space Path Loss
ICEV	Internal combustion engine vehicle
ISI	Intersymbol Interference
LCO	Lithium cobalt oxide
LFP	Lithium iron phosphate
Li-Po	Lithium-polymer
Li-ion	Lithium-ion
LMO	Lithium manganese oxide
LTO	Lithium titanate
MIMO	Multiple input multiple output
NaNiCl	Sodium nickel chloride
NaS	Sodium-sulfur
NCA	Lithium nickel cobalt aluminum oxide

NiCd Nickel-cadmium

NiMH Nickel-metal hydride

NMC Lithium nickel manganese cobalt oxide

OFDM Orthogonal frequency division multiplexing

OOK On-off Keying

PCB Printed circuit board

PHEV Plug-in hybrid electric vehicle

PHY Physical

PLC Power line communication

PLL Phase-locked Loop

PSK Phase shift keying

QAM Quadrature amplitude modulation

QPSK Quadrature phase shift keying

RMS Root Mean Square

SEM Semi-empirical model

SER Symbol error ratio

SMA SubMiniature Version A

SNR Signal to noise ratio

SoC State of charge

SoH State of health

SUV Sports utility vehicle

VISA Virtual instrument standard architecture

VNA Vector network analyser

VST Vector signal transceiver

Acknowledgements

I would like to express my sincere gratitude to my supervisors, Dr. Matthew Higgins, Dr. Erik Kampert and Mr. Andrew Moore, for their guidance, support, and encouragement throughout my PhD. I am deeply grateful for their invaluable insights and constructive feedback, which have greatly contributed to the development and success of this thesis.

I am grateful to my friends for their support and friendship throughout my studies. Their encouragement and camaraderie have been a constant source of motivation and strength.

I would also like to acknowledge the support of U.K. Engineering and Physical Sciences Research Council (EPSRC) for funding my research.

I am grateful to Dr. Mona Faraji Niri for providing the raw battery drive profile data used within simulations presented in Chapter 4.

Finally, I would like to thank my Mother, Father, and my Sister for their love and support throughout my studies. Their unwavering belief in me and constant encouragement have been a source of motivation and strength. I am forever grateful for their presence and support.

Declaration

I confirm that the contents of this thesis is my own work unless otherwise stated. This work has not been submitted for any other degree.

Mahyar Jafari Koshkouei

Abstract

battery electric vehicles (BEVs) are an important alternative to internal combustion engine vehicles (ICEVs) owing to reduced greenhouse and poisonous emissions overall when using renewable energy resources. The current challenges with BEVs are that they offer reduced driving range and need frequent charging in comparison to the refuelling rate of ICEVs. The performance of BEVs must thus be improved.

Smart batteries improve the performance and safety of energy storage systems through insights using techniques such as cell instrumentation, which is based on embedded sensors to gather enhanced cell characteristic data, such as internal cell temperature. This information is used to improve safety by reducing cell degradation and by mitigating critical events such as thermal runaway.

Embedding sensors within cells requires a wired connection to an external system for receiving and processing the data. Using a wire harness may cause electrolyte leakage and will add weight and complexity to the battery, reducing safety, energy density and increasing the cost of manufacture. Integrating power line communication (PLC) functionality within a smart cell will enable the processing and transmission of data, allowing for coordinated cell-to-cell performance and safety measures to take place within the battery. This requires no additional wires on the cell, as the existing power bus is used as a communication channel.

This thesis studies the PLC performance within a lithium-ion (Li-ion) battery for the purpose of operation within a reconfigurable large-scale energy storage system. Such research enables in-situ battery communication that allows for unprecedented improvements in cell performance and safety. Considerations of noise reduction, communication performance, and the benefits of using quadrature amplitude modulation (QAM) as a modern modulation scheme to increase data throughput, will be made throughout, as well as a review of the multitude of benefits such PLC systems make to the safety and performance of a BEV battery pack.

Publications Associated with this Research

- M. J. Koshkouei, E. Kampert, A. D. Moore and M. D. Higgins, 'Evaluation of an in situ QAM-based power line communication system for lithium-ion batteries,' *IET Electrical Systems in Transportation*, vol. 12, no. 1, pp. 15–25, 2021. DOI: 10.1049/els2.12033
- M. J. Koshkouei, E. Kampert, A. D. Moore and M. D. Higgins, 'Impact of battery state of charge on in-situ power line communication within an intelligent electric vehicle,' in *2022 IEEE 25th International Conference on Intelligent Transportation Systems (ITSC)*, IEEE, Oct. 2022. DOI: 10.1109/itsc55140.2022.9921800
- M. J. Koshkouei, E. Kampert, A. D. Moore and M. D. Higgins, 'Impact of lithium-ion battery state of charge on in situ QAM-based power line communication,' *Sensors*, vol. 22, no. 16, p. 6144, Aug. 2022, ISSN: 1424-8220. DOI: 10.3390/s22166144
- M. J. Koshkouei, E. Kampert, A. D. Moore and M. D. Higgins, 'In-situ QAM-based power line communication for large-scale intelligent battery management,' in *2022 7th International Conference on Robotics and Automation Engineering (ICRAE)*, IEEE, Nov. 2022. DOI: 10.1109/icrae56463.2022.10056199
- Under Review: M. J. Koshkouei, E. Kampert, A. D. Moore and M. D. Higgins, 'Battery configuration dependence to PLC using high-order QAM,' *under review*, 2022

- E. Kampert, M. J. Koshkouei, Y. K. Mo and M. D. Higgins, 'OTA 5G and beyond channel evaluation in a manufacturing environment,' in *2022 3rd URSI Atlantic and Asia Pacific Radio Science Meeting (AT-AP-RASC)*, IEEE, May 2022. DOI: 10.23919/at-ap-rasc54737.2022.9814165

- Y. Liu, V. Sanchez, P. J. Freire, J. E. Prilepsky, M. J. Koshkouei and M. D. Higgins, 'Attention-aided partial bidirectional RNN-based nonlinear equalizer in coherent optical systems,' *Optics Express*, vol. 30, no. 18, p. 32 908, Aug. 2022. DOI: 10.1364/oe.464159

Chapter 1

Introduction

Limiting the effects of climate change requires immediate action in reducing emissions of greenhouse gasses such as carbon dioxide. The use of renewable energy resources is seen as a crucial step to achieve this, demonstrated through a great momentum to research in this field and incorporation of such technology within infrastructure.

Renewable energy sources include solar energy which can be converted to electricity using photovoltaic modules. The potential of solar energy is great, with the total energy available for use on Earth from solar radiation documented as approximately 3.8 yottajoules [8], which is four orders of magnitude higher than the annual global energy consumption of 581 exajoules [9]. Alternative renewable energy sources that indirectly rely on solar radiation include hydropower, wind power, wave power, and bioenergy. Examples of renewable energy sources are shown in Figure 1.1. There are many other non-solar renewable sources of energy, including tidal energy and geothermal energy [8].

Hydropower is the process of generating electricity from the kinetic energy of a water source to turn a turbine. This method of generating electricity is intermittent, as rain itself is irregular and can be difficult to predict. This disadvantage is common with all renewable energy sources that rely on solar radiation. In fact, photovoltaic modules can only generate electricity during the day, and the rate of generation is impacted by the weather. In addition to the problem of uncertain electricity generation, the demand for electricity is subject to fluctuate based on both commercial and domestic user needs.

(a) Wind farm near Leeds, U.K. [10].

(b) Small hydroelectric plant in the Lake District, U.K.

(c) The Planta Solar 10 solar thermal power station in Spain [11].

(d) Wave energy converter in Orkney, U.K. [12].

Figure 1.1: Examples of renewable energy sources.

To match the changing demands for electricity given the unpredictable renewable electricity generation, energy storage systems can be used to act as a buffer between energy production and consumption in a technique referred to as 'load balancing'. One such system is pumped-storage hydroelectricity, where water is pumped into a reservoir at high elevation during times of low demand, and this stored water is released through a turbine to generate electricity during times of high demand [13]. The disadvantages of this technique are the lack of suitable locations for the construction of such pumped-storage systems which require two reservoirs separated by sufficient height, and the significant cost of construction and operation.

An alternative load balancing system is the use of large-scale rechargeable bat-

teries, such as those that use lithium-ion (Li-ion) cells, to charge during periods of low demand and discharge during high demand [14]. In contrast to a pump-storage system, a battery storage system can be installed in most places and have a very rapid response time. However, a pumped-storage system can reach an energy capacity of 3600 MW [15], whereas an average battery storage system connected to the smart grid provides much less power, typically 50 MW [16]. The smart grid concept uses modern technologies to improve reliability, sustainability and security of the electricity network. As such, the smart grid provides many advantages over the traditional grid, including improvements in demand response using smart metering infrastructure and data communication.

In addition to the use of Li-ion energy storage systems on the smart grid, the battery electric vehicle (BEV) also typically uses Li-ion cells. To reduce output of carbon emissions in transportation, the BEV can be charged with renewable energy. Some countries, such as France and the United Kingdom (UK), plan to cease the sale of new internal combustion engine vehicles (ICEVs) by 2035, with other countries indicating similar plans [17], [18]. These plans have incentivised a major push into the development of BEVs which are currently unable to outperform existing ICEVs in market share due to their comparatively long charging times, reduced travel distances on a single charge, and perceived high purchase and running costs [19], [20].

The success of the reduction in climate change and hence the production and use of renewable resources heavily depends on the performance of renewable energy storage systems. Such systems include portable electronics, BEVs and large-scale energy storage [21].

An important disadvantage of some renewable energies is their dependence on solar radiation, and in-turn the weather which is unpredictable and changing with the effects of climate change. These effects reduce the performance of renewable energy generation systems such as the photovoltaic cell and the wind turbine. Hence, large-scale energy storage systems are required to store power from these intermittent sources of energy for later use as demand requires [22].

BEVs have a reduced impact on climate change when powered from renewable resources in comparison to traditional ICEVs, including lower toxic gas emissions, higher energy density, and lower running costs which in turn improve accessibil-

ity [23]–[26]. However, as stated before, there are substantial limitations of using and adopting existing BEVs including limited driving range on a single charge in comparison to ICEVs. To encourage the adoption of these greener systems that do not release greenhouse gases into the atmosphere, these limitations in load balancing capabilities on the traditional grid and the limitations of battery electric vehicles must be addressed.

To mitigate these disadvantages in BEVs, established literature demonstrates improvements to energy storage systems, such as fast charging techniques, improved battery safety, capacity, and efficiency [27]. The BEV energy storage system typically utilises Li-ion cells due to their high energy and power density, lack of memory effect, and high efficiency, in comparison to other battery chemistries, such as nickel-metal hydride and lead acid [28]. Nevertheless, a Li-ion cell is sensitive to a variety of factors, such as ambient and internal temperatures, working voltages, and charge/discharge current rates. Operating a Li-ion cell outside of its small safety window will shorten its lifetime and performance, and further abuse may cause thermal runaway, fire, or even explosion [29]–[31].

To improve the safety of Li-ion cells, a battery management system (BMS) is typically used. The BMS adds over-charge, over-discharge, and over-current protections, to mitigate thermal runaway and other failures. Further features of the BMS include cell balancing, state of charge (SoC) monitoring, and state of health (SoH) monitoring [32]. Improving the performance of Li-ion cells also improves the performance of the BEV and the smart grid. However, the safety features of the BMS may impact the potential improvements to the performance of Li-ion cells. Further research must be performed to improve the performance of Li-ion cells whilst also improving the safety of their use.

The effectiveness of the BMS on the SoH of Li-ion cells may be increased by improving the quality and quantity of cell characteristic data available at run-time. This can be achieved through the use of thermo-electrochemical instrumentation of the cell [33], [34]. One such technique includes embedding fibre optics within the Li-ion cell to monitor core cell temperature [35]. Using this additional information, the BMS could then recognise the various tolerances of the cells within the pack, and use this knowledge to apply enhanced real-time coordination features to specific cells,

such as self-reconfiguration [36] and temperature regulation [37]. This intelligence improves performance by taking advantage of cells that are highly tolerant of harsh environments, and improve safety without abusing cells that have lower tolerances. By further combining this instrumentation technique with a constant-temperature constant-voltage charging scheme, charging times may be reduced by up to 20 % [38].

1.1 Research Motivation and Contributions

Instrumented cells depend on an external system to monitor and analyse sensor data. Therefore, an embedded system must be integrated within an instrumented cell to create a smart cell that can perform monitoring and analysis of in-situ sensors independently of external systems. The performance of these smart cells can be further improved by utilising a communication system, allowing for distributed functionality without the use of a BMS [39]. Such a communication system typically requires a wire harness independent of the bus bar to use as a communication bus. This wire harness increases the weight and complexity of the battery pack, and thus reduces its overall efficiency. Therefore, to avoid such disadvantages, power line communication (PLC) has been selected for potential use within smart cells, with the existing bus bar also utilised as a communication channel [40].

PLC is a communication technology that uses existing power lines for data transmission and is an alternative to traditional wired and wireless communication technologies, such as Ethernet and Wi-Fi, respectively. In fact, since PLC does not require new wiring, it is easy to install and can be used in power outlets common in the homes, buildings, and other facilities. In comparison to Wi-Fi, PLC offers improved signal coverage, especially in large buildings where Wi-Fi signals may not reach every corner. Despite not requiring additional wiring, PLC is capable of very high data rates, with the HomePlug AV2 specification capable of up to 1.5 Gbit/s [41].

However, the PLC channel suffers from interference caused by electrical appliances such as switching power supplies and motors. Furthermore, the power line network may use varying conductor types, cross sections joints, and termination impedances which make the power line a challenging medium to operate in [42]. The impedance will also change as the load on the power line changes, due to consumer

use for example. Impedance mismatch causes a multipath effect, whereby the signal propagates onto additional paths causing it to arrive at the receiver at different time intervals which can cause a reduction or amplification in signal amplitude or even nullification if the signals arrive 180 degrees out of phase. These effects can cause data corruption and/or loss. The existing standards HomePlug and IEEE 1901 are designed to overcome these harsh conditions of the PLC. Further details of these existing standards are provided in Section 2.7.

Contributions to PLC research continue in improving the utilisation of cleaner technologies, such as with smart grid and BEVs connectivity, which enhances the performance and safety of energy storage and delivery systems. Such research takes us a step closer to achieving the aims of zero-emission transport by 2035 and then climate neutrality by 2050 [43]. To this end, using cell instrumentation, the accuracy of cell characterisation for understanding and identifying their limitations and capabilities is increased. As already stated, various technical developments have already achieved improvements in terms of battery performance and safety, including reduced charging times by utilising smarter sensor-dependent charging schemes, improved safety by detecting high temperature within the core of the cell, and increased cell health by improving cell balancing techniques [44].

In order to understand the Li-ion cell as a physical channel through which communication signals can propagate, characterisation must be performed since the Li-ion is a different environment to the traditional home or building power network that existing standards such as HomePlug and IEEE 1901 target. This characterisation is important as it will determine the most appropriate communication parameters for an in-situ battery PLC network, such as carrier frequency, bandwidth, and quadrature amplitude modulation (QAM) order. There is limited literature on the analysis and use of a battery as a communication channel for PLC. Therefore, the battery must be characterised to understand its physical properties before a PLC system with the most appropriate parameters can be selected.

One such cell characterisation technique is electrochemical impedance spectroscopy (EIS), which uses alternating current (AC) in a typical frequency range from 1 mHz to 10 kHz to determine the cell impedance which represents its frequency-dependent properties of resistance and reactance. Established literature has shown

that EIS can be used to estimate the cell's SoH, SoC, and even its internal temperature [45]. These techniques have not yet been fully integrated within commercial large-scale energy storage systems due to the impact to the system size, weight, and complexity. The use of cell management systems (CMSs) allows for these techniques by exploiting cell instrumentation and online EIS measurements, but only for a single cell at any one time. As large-scale energy storage systems are made up of many individual cells, existing techniques are limited to determining the safety and performance of each cell as an independent system. Hence, a knowledge gap exists in determining a suitable method of communication between each independent smart cell to create a mesh network of smart cells that can work as a whole system. When a battery is working as a whole system, the smart cells will be able to provide additional benefits to the energy storage system, including coordination of safety and performance measures such as battery reconfiguration to improve cell balancing capabilities and to remove faulty cells from the power bus. As such, the data that is expected to be communicated between smart cells within an in-situ PLC smart battery system include cell voltage, current, and temperature, but in the future this may be expanded to include battery configuration parameters, SoC and SoH estimations, and further variables that have not yet been identified.

In addition to the selection of a communication method, the characteristics of the Li-ion cell for the purpose of communication have yet to be understood and identified. Existing methods of Li-ion cell characterisation must be altered to allow for testing of high signal (carrier) frequencies suitable for communication. Typical EIS frequencies are only suitable for low data rate communication, and, some of these frequencies may display changes in communication performance due to changes in cell SoC, SoH and temperature. Such testing has not yet been performed to determine changes in cell characteristics with SoC, high carrier frequencies, and battery configuration.

In this thesis, PLC is selected as a potential candidate for an in-situ smart battery communication system given that the existing power bus (such as the battery bus bar) within the battery can simply be used as a communication channel as opposed to a dedicated communication bus that uses an additional wire harness. Despite the general advantages to the use of PLC, knowledge gaps persist on this topic, where it is not known whether very high data rates may be achieved within a large-scale battery

and whether high carrier frequencies up to 6 GHz can be used on the communication system without influencing the properties of the cell. This is beneficial, as a smart large-scale battery may utilise thousands of smart cells which will be communicating status and sensor data to other smart cells within the battery and also to external systems such as the BEV. Such sensor data may include internal and surface temperature, cell voltage required for battery balancing and reconfiguration. Since the scale of such batteries is large, the amount of data that must be communicated with other smart cells will increase dramatically. It is important to examine the expected response time and data rates of reporting sensor data, as these will affect the time taken to react to any critical alerts raised from a smart cell. In addition, as the communication system's data rate is proportional to the allocated bandwidth around the carrier frequency, for reliable communication it is required that the cell characteristics remain constant over that bandwidth. Hence, to locate these appropriate frequency ranges within the technically accessible spectrum, the cell characteristics need to be evaluated over a large range of carrier frequencies. Therefore, the PLC system is yet to be tested to ensure that the communication system will not be saturated with data and result in a delay reporting certain critical warnings from smart cells. Increasing the data rate and decreasing the round trip time of sensor data on an in-situ battery communication system will increase the capability of mitigating critical events such as thermal runaway. To this end, in this thesis the use of modern modulation schemes, such as QAM, will be considered for use within the smart battery system, to allow for improvements to communication performance, such as increased data rates.

The research and implementation of the smart cell is in its infancy, as there has not yet been an established definitive standard or implementation of smart cell techniques in production. As such, this research examines the performance of a prospective PLC system with a passive Li-ion cell. The findings of the experiments presented in this thesis may then be used to determine the performance of future in-situ smart battery PLC systems within existing Li-ion cell chemistries. The experimental procedures used in this thesis can be used to investigate potential new cell models and chemistries, and predict their communication performance in a system with varying SoCs and configurations. The experimental procedures used in this thesis can be used to investigate potential new cell models and predict their communication performance

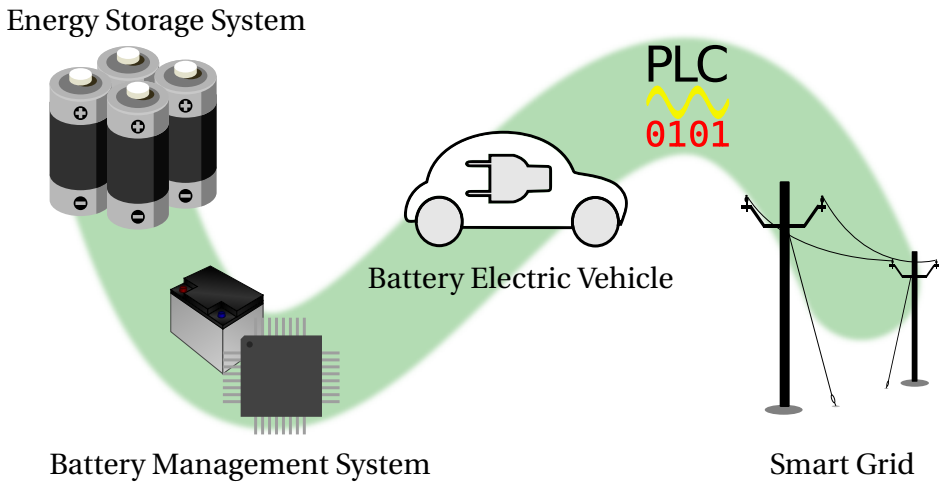

Figure 1.2: High-level overview of vehicular systems and services connected by PLC. The bidirectional PLC network is shown in green.

in a system with varying configurations based on the analysis of the impedance and scattering parameter measurements.

Figure 1.2 highlights an additional benefit of using PLC within an energy storage system. It is shown that PLC can be further extended to form a part of a larger network that allows for bidirectional communication between each smart cell within an energy storage system to the smart grid. Such research is useful as it enables improved understanding of local energy consumption habits which the smart grid can use to improve energy demand response.

Established literature has not yet identified changes in PLC performance when transmitted through Li-ion cells at various SoC, when configured in a variety of different battery configurations, and when under a certain load. Hence, the overarching aim of the research presented in this thesis is to evaluate the performance of PLC through Li-ion cells, and to determine appropriate parameters for a PLC system for use within large-scale energy storage systems, such as those used within BEVs and the smart grid.

To achieve this aim, the following objectives will be explored:

- Define the requirements of a communication system capable of operating within large-scale energy storage.
- Determine the electrical parameters for the characterisation of Li-ion cells

relevant to PLC.

- Evaluate existing methodologies for the characterisation of a Li-ion cell as a communication channel.
- Propose improvements to Li-ion cell characterisation methods to increase reproducibility and accuracy of communication performance test results.
- Determine the performance of a Li-ion battery when used as a communication channel in a variety of circumstances:
  - when the Li-ion battery is under load, such as through driving a BEV;
  - when the Li-ion battery is at different SoC due to charging or discharging;
  - and when the Li-ion battery is configured differently such that the number of cells connected in series and in parallel are changed.
- Propose new experimental methodologies for testing the performance of PLC in Li-ion cells at high carrier frequencies and QAM orders of up to 6 GHz and 1024-QAM, respectively.
- Propose appropriate parameters of carrier frequency, QAM order, and battery configuration for a PLC system for use within Li-ion batteries.

1.2 Thesis Outline

This thesis is comprised of seven chapters. In Chapter 1, I have presented the research context and rationale, providing a summary of the motivations for the primary aim and objectives. This chapter captures the existing limitations in energy storage systems and a discussion on how instrumented smart cells combined with a PLC system may be used to address such limitations.

In Chapter 2, a narrative literature review of relevant existing methodologies and experimentation of Li-ion smart cells is presented, accompanied with a critical analysis on the use of such techniques including their advantages and limitations. Also in

this chapter the specifications of various existing batteries are summarised and compared. Moreover, the rationale behind the selection of the Li-ion battery is discussed and justified.

The common detail that binds all of the experimental chapters are presented in Chapter 3. In this chapter I present my methodology and explain the choice of methods and techniques used to accomplish the research objectives.

In Chapter 4, existing experimental results of a Li-ion cell's impedance characteristics for signal frequencies of 100 kHz to 200 MHz are exploited and analysed in order to create a realistic battery model. This model is used to determine the effectiveness and optimal properties of PLC with QAM, as a means of in-situ battery communication for BEVs in combination with a real-world dynamic drive profile to simulate the internal electrical environment within a BEV. In addition, the use of signal conditioning techniques for improving the PLC performance within this simulated environment is discussed. My published work [1] is based on the data presented within this chapter.

In Chapter 5, the changing characteristics of the Li-ion cell at various SoC are measured, analysed and compared to understand their effectiveness on the communication channel of a PLC system for carrier frequencies of 10 MHz to 6 GHz. Moreover, the use of QAM is investigated to determine its effectiveness as a state-of-the-art modulation method for the same carrier frequency range. Published works [2], [3] are based on this chapter.

In Chapter 6, the performance of a PLC system with carrier frequencies of 10 MHz to 6 GHz is evaluated for its changes in scattering parameters and transmission error ratios for a single cell, two cells in parallel, two cells in series, and a combination of two cells in parallel and series, configurations of Li-ion batteries. Furthermore, QAM orders of up to 1024 are tested for their usability and reliability within such environments. Published works [4], [5] are based on this chapter.

Chapter 7 will bring together all of the presented overall findings in the preceding chapters, providing a narrative of the overall work and concluding remarks on the research presented. Future works are also proposed for further advancements in this research field.

Chapter 2

Background

The electrochemical battery was invented in 1781 when Alessandro Giuseppe Antonio Anastasio Volta created the "Voltaic Pile" using copper, silver, and cardboard soaked in brine [46]. This Voltaic Pile initiated a series of scientific achievements, including Michael Faraday's studies of electromagnetism. This technology has continued to evolve, with further improvements to battery technology and the use of batteries in telegraphs, and, even within electric vehicles in the 1900's [47]. Further advancement continue to be made in the 21st century, with new battery chemistries, such as lithium-ion (Li-ion). New techniques including cell instrumentation have received much attention for their potential in improving energy storage capabilities. This chapter presents a review of the available literature on such technologies that are discussed and utilised within this research.

2.1 The Lithium-ion Battery

Primary batteries, commonly referred to as non-rechargeable batteries, were mostly dominant for use within the market for small devices such as within toy cars and remote controls until the 1970s when secondary batteries, also known as rechargeable batteries such as lead-acid and nickel-cadmium (NiCd), became the mainstay, replacing the vast majority of primary batteries[48]. This trend begins to demonstrate the shift in the market and consumer usage of single-use products, in favour of those equipped with recharging capability and thus multi-use products thought to be a

more sustainable alternative. The energy density of NiCd cells reached a limit towards the end of the 1980's, which triggered a growing effort in developing the next level in secondary batteries. In 1991, Sony Corporation introduced the lithium-ion (Li-ion) cell to the market [48]. This Li-ion cell was based on the works by J. Goodenough who had used lithium cobalt oxide as a cathode to achieve nearly twice the open-circuit voltage than previously achieved with this cell type [49], [50]. A brief history of early Li-ion batteries, including the development of the cathode and anode materials, has been presented in [51]. Since the creation of the Li-ion battery, there have been many developments on this technology to improve battery performance and safety [52]. Such developments include the selection of a safer and more stable cathode and anode. In the late 1990s, it was found that a 40 % increase in energy density could be achieved by using an lithium cobalt oxide (LCO) cathode, and simply charging it to a higher voltage of 4.5 V rather than the typical limit of 4.2 V. This, however, decreased the cycle stability and the safety of the Li-ion cell significantly [53]. Towards the end of the 20th century, the lithium-polymer (Li-Po) battery was designed with a gel substance used as an electrolyte as opposed to the liquid electrolyte used at the time [54]. This technology reduced the volume of liquid within the Li-ion cell, and removed the need for heavy casings on the cell, thereby increasing the energy density of the battery. In addition, not only does the polymer electrolyte offer advantages of being less flammable than a liquid electrolyte, it has also been shown to limit the formation of lithium dendrites on the electrode. These dendrites are deposits of lithium that may form on the lithium anode during cell charging and discharging, which cause capacity loss and may eventually pierce the separator between the anode and cathode, resulting in an internal short circuit that causes catastrophic failure and fire [55]. There continues to be significant research focused on improving the safety and performance of Li-ion batteries, including the reduction of dendrite formation using a solid electrolyte separator [56] and the use of different Li-ion cell chemistries as explained later in this section.

In the current work environment, the Li-ion battery is normally selected for use within energy storage systems due to a number of key factors, chiefly, the relative high operating voltage, no memory effect, low self-discharge, high power density, high energy density, long cycle life and high efficiency in comparison to other battery

Table 2.1: Comparison of battery chemistries [58].

Battery Type	Energy Density (Wh/L)	Power Density (W/L)	Nominal Voltage (V)	Life Cycle	Depth of Discharge (%)	Round Trip Efficiency (%)	Estimated Cost (USD/kWh)
Lead-acid	50-80	10-400	2.0	1500	50	82	105-475
NaS	140-300	140-180	2.08	5000	100	80	263-735
NaNiCl	160-275	150-270	-	3000	100	84	315-488
NiCd	60-150	80-600	1.3	2500	85	83	-
Li-ion	200-400	1500-10,000	3.2-3.8[59]	10,000	95	96	200-1260

chemistries [57]. Comparisons of Li-ion cells to other battery chemistries, such as nickel-metal hydride (NiMH) and NiCd, are presented in Table 2.1.

Various Li-ion chemistries have been produced, with each offering a different advantage in comparison to the other. Such differences are collated and presented in Table 2.2. It is shown that lithium nickel manganese cobalt oxide (NMC) has high specific energy and power properties, whilst also maintaining a good level of performance and safety. Hence, NMC is typically the preferred choice of Li-ion battery chemistry for battery electric vehicles (BEVs) [60]. However, despite having a comparatively reduced performance, lithium iron phosphate (LFP) is also a candidate for use within heavy-duty vehicles due to the high discharge rate, long cycle life, and improved safety, in comparison to NMC. The discharge and charge rates are presented in 'C-rate', which is the rate at which a battery is charged or discharged relative to its capacity.

The Li-ion battery is manufactured in different shapes and sizes. The well known normal shapes are typically cylindrical or prismatic. Cylindrical cells are so called owing to their characteristic round winding jelly roll enclosed within a hard case, whereas prismatic cells use a flat winding enclosed within a hard case or a pouch [62]. A prismatic cell enclosed within a pouch is referred to as a 'pouch cell'. Energy storage systems within BEVs typically use many cylindrical cells, such as the 18650 model which has a diameter of 18mm and a length of 65mm, or a custom sized pouch cell. An overview of the cell types described herein is shown in Figure 2.1.

Now that the most commonly found cell types have been presented, the next

Table 2.2: Comparison of common Li-ion battery chemistries [59].

Parameter	Lithium cobalt oxide (LCO)	Lithium manganese oxide (LMO)	Lithium nickel manganese oxide (NMC)	Lithium iron phosphate (LFP)	Lithium nickel cobalt aluminium oxide (NCA)	Lithium titanate (LTO)
Specific power	L	M	M	H	M	M
Specific energy (Wh/kg)	150-240	100–150	150–220	90–120	200–300	50–80
Safety	L	M	M	H	L	H
Life Cycle	500–1000	300–700	1000–2000	1000–2000	500	3000–7000
Cost	L	L	L	L	M	H
Performance	M	L	M	M	M	H
Nominal voltage (V)	3.6	3.7	3.6	3.2	3.6	2.4
Typical Charge rate	0.7–1C	0.7–1C	0.7–1C	1C	1C	1C
Typical Discharge rate	1C	<10C	<2C	<25C	1C	<10C
Thermal runaway	150 °C	250 °C	210 °C	270 °C	150 °C	High safety

L: Low; M: Medium; H: High.

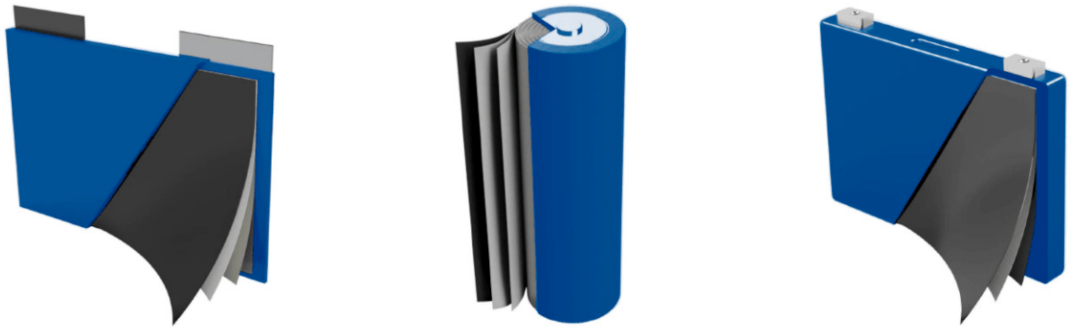

Figure 2.1: An overview of Li-ion cell types showing the layers of the jelly roll. From left to right: Pouch, Cylindrical, and Prismatic cells [61].

Table 2.3: Battery configurations of common consumer worldwide available electric vehicles as of February 2019. Estimated configurations are enclosed within parenthesis.

Model	Type	Size	Battery Power (kWh)	Battery Pack Configuration
Tesla Model 3	BEV, luxury saloon	Large	50/62/75 [63], [64]	96S-31P-21700 or (96S-38P-21700) or 96S-46P-21700, NMC
BYD Yuan EV360	BEV, compact crossover SUV	SUV	43.2 [65]	(96S-40P-18650)
Nissan Leaf	BEV, compact hatchback	Medium	24/30 [66]	96S-2P-Custom Li-ion Pouch Cell
BYD Tang PHEV	PHEV, compact crossover SUV	SUV	18.4 [67]	(30S-52P)-LFP
Baojun E100	BEV, two-seat city car	Mini	24 [68], [69]	(31S-68P-18650)
Mitsubishi Outlander PHEV	PHEV, compact crossover SUV	SUV	13.8 [70]	80S-(14P)-(18650) [71]
Renault Zoe	BEV, compact hatchback	Small	41 [18]	96S-2P Custom Li-ion Pouch Cell [72]
Chery eQ EV	BEV, city car	Mini	22.3 [73]	(31S-63P-18650)
Geely Emgrand EV	BEV, saloon	Large	41/52 [74]	(96S-39P) or (96S-49P), LFP [75], NMC [76]
BYD e5	BEV, saloon	Large	60.48 [77] / 48 [75] / 43 [76]	65Ah [78], LFP [75], [76] (96S-46P)

segment to tackle is the possible configuration of the battery pack. To support this in a clear visual presentation, the battery pack configurations of popular BEVs are presented in Table 2.3. It can be clearly identified from the table shown that NMC 18650-model cylindrical cells are one of the most common in BEV energy storage configurations. Furthermore, since the nominal voltage of a NMC cell is 3.6 V, many of the popular BEVs listed in Table 2.3 use 96 cells in series to produce a nominal internal voltage of 350 V. One drawback identified in recent times has resulted in a shift to using LFP Li-ion chemistry instead of NMC, which is due to the reduced cost of manufacture and increased safety, despite the reduced energy density [79].

2.2 Battery Management and Safety

The Li-ion battery is damaged by over-charging and deep discharging, over-current during charging and discharging, and by internal and external short circuits. Hence a battery management system (BMS) is required to monitor battery status and mitigate such failures [80]. The BMS performs real-time monitoring of the battery state of charge (SoC) to provide such mitigations [81]. A critical review of the BMS in the context of BEVs has been presented in [82], in which the requirements for using a BMS has been listed as in Table 2.4. An estimation of the state of health (SoH) of the Li-ion battery may also be used to measure ageing, such as in capacity and performance, which decline over time and reduce the maximum power output of the battery [83].

The safety features provided by the BMS for Li-ion batteries are required, due to the damaging mentioned in the previous paragraph, however, the BMS typically restricts opportunities in performance optimisation of Li-ion batteries due to estimations of a worse case scenario based upon existing characterisations of Li-ion cells. Such estimations include that of the SoC. A critical review of the methods of estimating the Li-ion SoC has been presented in [58]. Further techniques for SoC and SoH estimations have been discussed in [85], which include battery modelling, Kalman filters, intelligent algorithms, and neural network algorithms. Improved characterisation of the Li-ion cell may reduce the impact of safety strategies on the performance of Li-ion cells by providing closer tracking of further cell characteristics, such as SoC and SoH, enabling greater BMS intelligence use when assessing cell risk profile. A review of BMS

Table 2.4: A summary of the requirements for using a BMS [82].

Requirement	Reasoning
Cell Monitoring	To keep the battery cells within safe operating limits, parameters such as cell voltage, temperature, and current must be monitored.
Battery Safety and Protection	No cell in the battery must exceed the safety critical limits regarding voltage and temperature.
Estimation of SoC and SoH	SoC and SoH are important indicators for battery systems as they serve as a basis for functionalities such as range prediction, balancing, etc.
Ensure Isolation	The BMS must guarantee isolation between the high voltages of the energy storage and the rest of the vehicle.
Balancing	To mitigate over-charging and deep-discharging, the cells within the battery must be balanced.
Charge Control	Batteries have limitations for the charge current and voltage. These have to be considered during the charging process as exceeding them may cause critical safety events, such as fire.
Thermal Management	For safety purposes, but also to increase the efficiency, the battery must be operated in an optimal temperature range. The performance of the Li-ion decreases significantly when used below freezing temperature [84]. For this purpose, it can be cooled as well as heated.
Communication with the Car	The BMS is responsible for sharing important parameters like the SoC of the battery with the other vehicle's components. Furthermore, power requirements of the drive train are received.
Battery Disconnection	In emergency case or when the vehicle is parked the BMS disconnect the battery from the main system.
Control reconfigurable battery system switches	A significant number of switches are controlled to reconfigure the energy storage system. Depending on the reconfigurable battery system type and its functionality, the switching operation must be performed with high synchronicity.

developments and standards has been presented in [86].

Research is ongoing into the characterisation of the Li-ion cell, providing further techniques in improving the performance of the BMS and the Li-ion battery.

2.3 Improvements to Lithium-ion Battery Performance

Extensive research is required to improve Li-ion batteries, including safety, efficiency, power delivery, and also in the reduction and mitigation for battery ageing. In the paragraphs that follow, important studies as in established literature on improvements to Li-ion battery performance are discussed. Further methods of improving Li-ion battery performance including cell instrumentation and sensing is described in Section 2.4 and the use of embedded systems to create smart cells is explored in Section 2.5.

2.3.1 Fault Diagnosis

One of the main requirements of the BMS is fault diagnosis, which ensures the safe and reliable use of the battery pack by detecting faults and minimising the effects of such faults. A review of fault diagnostic algorithms has been presented in [87], and fault diagnosis methods for external and internal faults have been presented in [82]. These works have highlighted the trend that recent studies demonstrate a model-based approach to sensor fault diagnosis, whereby thermal and electrical models of a Li-ion battery were developed to verify a novel sensor fault diagnosis scheme [88].

2.3.2 Lithium-ion Cell Modelling

Modelling the Li-ion cell allows for predicting battery behaviours, such as calendar ageing and performance. One popular approach to Li-ion cell modelling is the equivalent circuit model (ECM), which is used to model the electrical behaviour of the battery [82]. Alternative approaches to modelling relationships of the battery include the semi-empirical model (SEM) which draws on mathematical functions, and the data-driven model (DDM) which utilises existing data. These three modelling techniques for the calendar ageing prediction of Li-ion cells have been studied in [89].

2.3.3 SoC Identification

The identification of the SoC of a Li-ion cell is required for the mitigation of over-charging and deep discharging. In [90], a SoC estimation method based upon a gas-liquid dynamic model using a Cubature Kalman filter with state constraints was proposed which showed a SoC error of less than 2 %. In [91], an SoC estimation method considering the effects of temperature at −10 °C, 25 °C and 50 °C using an adaptive dual extended Kalman filter was demonstrated to yield higher accuracy than without the use of the Kalman filter. A relationship between the SoC of a Li-ion pouch cell and the sound velocity of applied ultrasonic signals has been demonstrated in [92]. It was shown that the sound velocity is influenced by the temperature, charging/discharging current, and voltage of the pouch cell. A review of Li-ion battery SoC estimation models has been given in [93].

2.3.4 SoH Identification

The identification of the SoH of a Li-ion cell is used to determine the reliability and safety of the system by comparing the current condition of the battery to an ideal battery. The SoH is used to anticipate battery ageing, which is affected by time, environmental factors such as temperature, and use. In [94], an online battery model using a novel algorithm was demonstrated to provide an estimation of battery capacity and internal resistance with an average error of 1.2 % and 4 %, respectively. The battery capacity and internal resistance are parameters to determining the battery SoH. In this work, it has also been stated that determining the SoH may be used to recycle cells for 'battery second life'. An improved radial basis function neural network to estimate battery SoH has been proposed in [95]. It has been shown that this method was able to estimate SoH with a maximum error of ±4 %, which is an improvement over traditional neural network-based algorithms. In [96], the relationship between battery degradation and battery SoH were established using constant current charging data, the Pearson correlation coefficient, and a long short term memory neural network was used for model training to achieve an accurate SoH estimation. Predicting SoC and SoH of Li-ion cells using machine learning and deep learning approaches have been reviewed in [97]. A survey of SoH estimation methods using modelling has been presented in [98].

2.3.5 Battery Reconfiguration

Large scale energy storage systems are normally designed to a specified number of cells connected in parallel and series. However, using switches embedded within the energy storage system, the battery may be reconfigured. This battery reconfiguration can improve safety and performance through the intelligent use of the cells, such as:

Cell Balancing

The conditions within the energy storage system may not be uniform for all cells. Many factors including manufacturing tolerances, different self-discharge rates, and uneven temperatures within the energy storage system have an effect on the ageing process of the cell, which begin to cause SoC and SoH balancing issues within the battery [36], [82].

Cell Disconnection

Battery reconfiguration allows for the disconnection of specific cells within the energy storage system, allowing for faulty cells to be disconnected without replacing the entire battery.

Topology Switching

A reconfigurable battery is capable of changing the output voltage and current of the energy storage system by modifying the configuration of the battery. Such technique may eliminate the need for a DC-DC power supply in systems that require a stable output voltage. In [36], a self-reconfigurable battery topology was proposed and demonstrated with 9 Li-ion cells to guarantee an output voltage without the use of a DC-DC converter.

The self-reconfiguration of batteries compared to conventional batteries has been shown to improve the lifetime of cells by 16 % and increase the energy output by 16.8 % [99]. Two SoH-aware reconfiguration algorithms were evaluated analytically and experimentally via emulation in [100], to show a 10 % to 60 % improvement in capacity delivery compared to alternative approaches to reconfiguration that were oblivious to SoH.

2.4 Cell Instrumentation and Sensing

Some research has been carried out to obtain applicable techniques in fast charging Li-ion cells [101]. Such techniques include the instrumentation of the Li-ion cell for measuring the core temperature of the cell that may then be used for accurate cell modelling and analysis.

In [102], a thermocouple matrix was embedded within a Li-ion pouch cell to determine the internal core temperature. Whilst the embedded sensor was able to detect the internal temperature of the cell, further work is required to mitigate electrolyte leakage which occurred due to the weakening adhesion of the embedded sensor.

In [103], a thin optical fibre was used for temperature sensing and placed on the top and bottom surfaces of a Li-ion pouch cell, and also in between two other pouch cells. During a 1 C-rate discharge cycle (i.e. the cell is fully discharged in one hour with a current through the battery that is equal to the theoretical current draw under which the battery would deliver its nominal rated capacity in one hour), temperature hot spots on the surface of the pouch cells were found with temperature variations of up to 8 °C. In this direction, a Rayleigh scattering based optical fibre has been utilised to improve the temperature sensing accuracy of the optical fibre placed on the surface of a Li-ion pouch cell [104]. In this work, it was found that during a 5 C-rate discharge at an ambient temperature of 10 °C a maximum in-plane temperature variation of 11.8 °C was recorded with the optical fibre-based temperature sensing method. In comparison, the traditional thermocouple-based temperature sensing method recorded a maximum in-plane temperature variation of only 2.9 °C, which was a vast underestimation in surface temperature, and showed a comparative insensitivity to hot spots. In other work, an optical fibre with Bragg gratings embedded within a Li-ion cylindrical cell was used to measure the core temperature [105]. It was shown that the core temperature and the surface temperature were different during mild cell cycling (i.e. repeated charging and discharging), which indicates candidacy for improved cell characterisation. To improve the use of optical fibres for internal temperature sensing of Li-ion cells during operation, further study is required. This is inclusive of the ability to differentiate changes in fibre Bragg grating signals from temperature and strain with the cell [106]. In addition, the size of the optical fibre must

be minimised to reduce the interference that the sensor may have on the function of the Li-ion cell. Further optical fibre temperature sensing techniques can be found in [34].

In [33], it was found that after modifying a Li-ion by embedding temperature sensors, the safety limits of the internal core temperature had been surpassed. In addition, the charging time may be decreased as a higher charging current may be utilised without exceeding the manufacturers' specification on thermal stability.

A methodology for in-situ cell instrumentation has been presented in [107]. In this work, thermocouples were embedded within 21700-model Li-ion cylindrical cells, and it was shown that not only the internal temperature was noticeably higher than the surface temperature, but also after cycling using a profile derived from a BEV, and this difference in temperature would increase as the SoH decreased. The steps taken to instrument the Li-ion cell can be summarised as: first, discharging the cell to minimise the effects of safety hazards (such as damaging the jelly roll) that may be caused by the insertion of sensors within the cell. Next, a hole is created on the top of the cell using a bench pillar drill and then the sensors are inserted into the cell through the hole. Finally, the hole is sealed using using a nylon screw. A reference performance test was conducted throughout this procedure to verify that the method of instrumentation did not negatively impact the cell. It was found that the state of the instrumented cell had negligible change due to the instrumentation procedure and also after two months of storage.

2.5 Smart Cells

For these stated in-situ sensing techniques, an external system is necessary to collect and process the acquired data for each Li-ion cell. For large-scale batteries that incorporate many individual cells, such as those used within BEVs, a direct connection of sensors from each cell to an external system, such as the BMS using a wire harness, is an overhead within a battery, potentially impairing performance, energy density and robustness in a harsh environment, requiring extra space, higher wire termination count and additional weight. As already stated, embedding a sensor within the Li-ion cell may cause electrolyte leakage due to weakening adhesives. Instead of using

an external acquisition system to record and process this in-situ sensor data, an embedded system may be integrated within the cell in addition to embedded sensors. Embedding some BMS functionality within an instrumented Li-ion cell is known as the cell management system (CMS) and are typically named 'smart cells'. The advantages of smart cells include higher operational flexibility, fault tolerance, safety management, equalisation, and life management and history [108].

A decentralised system of three smart cells, each a Li-ion cell with an embedded system, has been designed and tested without the use of an external BMS including the smart cell performing estimations of cell voltages during operation [109]. Also for large-scale batteries, a communication system would provide additional benefits as was recommended, following the distributed cell management experiments.

A self-balancing system of eight smart cells has also been designed and demonstrated using controller area network (CAN bus) communication between each smart cell for sharing cell voltage and SoC information [110]. A two-wire power communication bus for smart Li-ion cells has been presented in [111], where the embedded systems within cells are additionally powered from the communication bus.

Ongoing research attempts to remove the need for any additional wire harness within a battery pack for cell-to-cell and cell-to-BMS communication. These techniques include the use of wireless communication and power line communication (PLC), which may be utilised to communicate with other smart cells as part of a mesh network, or with a BMS. A modular BMS with a wireless communication system has been designed in [112] with a particular focus on low power consumption. A wireless communication system embedded within a single 18650-model cylindrical Li-ion cell was simulated, built and demonstrated [113]. In this study, a wireless communication range of up to 10 m has been demonstrated and the use of an SubMiniature version A (SMA) connector and also an SMA connector with a wire loop antenna was tested. A capacitive coupling technique for transmitting data from an in-situ cell temperature sensor to an external system has been demonstrated in [114].

Further research is required to determine the effectiveness of in-situ cell wireless communication systems within large-scale batteries.

2.6 Use of Passive Cells in Smart Cell Research

A smart cell has not yet been widely produced, as research is ongoing in realising the capabilities of the smart system and also in designing a safe procedure of manufacture for embedding a computer system and sensors within a cell. Existing literature on advancements in instrumented cell technology presented in Section 2.4 demonstrates the use of a commonly available passive cell, that is subsequently enhanced into an instrumented cell by embedding sensors. Such literature present a methodology on the embedding of the sensors within the cell and other cell modifications, which requires opening the cell, inserting the desirable components (such as a PLC modem and a microcontroller) within the cell, and then sealing the opening.

Recent literature has shown that the process of instrumentation during and after manufacture has negligible effects on the state of the Li-ion cell. For instance, it has been shown in [105] that an electrochemical impedance spectroscopy (EIS) of the modified instrumented cell demonstrated no change in impedance due to the procedure. Using this fact, it can be concluded that performing PLC channel analysis on a passive cell and an instrumented cell of the same type will not show any significant different. The integration of sensors within an instrumented cell requires significant tooling and careful methodology to accomplish. Since the aim of this research is to determine the performance of an in-situ battery PLC system, it is not necessary to perform such testing on an instrumented cell. In addition, the integration of an embedded computer system within a Li-ion cylindrical cell has not yet been reliably achieved in existing literature.

Hence, this research will use a passive cell to conduct such experimentation, as the physical properties of the Li-ion are not expected to change after a computer system and sensors are embedded within it, based on existing literature that demonstrates the installation of in-situ sensors. The findings of this research, based on the experimentation of a passive cell, will still be suitable for future smart cells.

2.7 Power Line Communication

PLC enables the transmission of data over existing power line infrastructure. Since the existing electrical power distribution network is used to carry data signals, PLC is

seen as a cost-effective and versatile means of communication. PLC is widely used in homes and buildings and is standardised through HomePlug and IEEE 1901, allowing its use in a wide range of applications, including smart grid systems, home automation, internet access, and industrial control.

HomePlug 1.0 was the first PLC specification for in-home high-speed networking and was released in 2001 to overcome the harsh conditions of the power line channel [115]. The physical (PHY) layer of the HomePlug 1.0 specification describes the detection of channel conditions to allow for the selection of suitable subcarriers for orthogonal frequency division multiplexing (OFDM) and phase shift keying (PSK) modulation methods, such as binary phase shift keying (BPSK). OFDM is a technique that divides wideband into multiple narrowband subcarriers, each of which modulating signals at a different carrier frequency that is mathematically orthogonal to the carrier frequencies of the other subcarriers [116]. This makes OFDM suitable for use within the harsh conditions of the power line channel as it has high bandwidth efficiency and has increased resistance to constructive and destructive interference. Such interference includes multipath fading, whereby multiple instances of a transmitted signal reach the receiver via different paths. Hence, HomePlug 1.0 uses OFDM with 84 equally spaced subcarriers of 24.414 kHz between 4.5 MHz to 20.7 MHz, offering a maximum throughput on the PHY layer of 13.78 Mbit/s [42].

Since the release of the HomePlug 1.0 specification, many PLC specifications and standards have been published, including HomePlug AV which was introduced in 2005 and allows the selection of quadrature amplitude modulation (QAM) (which is explained in more detail in Section 2.9) up to 1024-QAM, and 1155 OFDM subcarriers in a wider frequency range of 1.8 MHz to 30 MHz, to offer a maximum PHY throughput of 200 Mbit/s [117]. In 2010, the IEEE 1901 standard was released, which adds an additional frequency band of 30 MHz to 50 MHz, allowing for a peak PHY rate of 500 Mbit/s. In the same year, the HomePlug Green PHY standard was released as a low-speed (10 Mbit/s) and robust alternative to HomePlug AV, which exclusively utilises quadrature phase shift keying (QPSK) with a robust (ROBO) mode of OFDM, targeting smart energy communication utilities such as smart meters, home appliances and BEVs [118]. In 2012, HomePlug AV2 was released, increasing the maximum PHY rate to 2024 Mbit/s by employing 3455 carriers in the range of 1.8 MHz to 86.13 MHz, up to

4096-QAM, and by using multiple input multiple output (MIMO) with beamforming, a method of increasing performance by utilising multiple transmitters and receivers [41], [119]. These capabilities were added whilst remaining backwards compatible with previous Homeplug and IEEE 1901 devices.

A single-wire PLC system has been demonstrated between the frequency range of 130 MHz to 20 GHz in [120] for the purpose of smart grid communication, demonstrating the possibilities of much higher carrier frequencies for PLC than is specified within the established HomePlug and IEEE 1901 standards.

For the specific use of PLC in smart grid applications, the G3-PLC standard, by the G3-PLC Alliance, is used. G3-PLC is low-speed narrowband standard typically used in home automation and smart metering where the high-speed data rates provided by broadband standards of HomePlug and IEEE 1901 are not suitable [121]. In smart metering applications, it is typically expected that the data transmitted is little and at intervals of 15 min to an hour [122]. The typical carrier frequencies used in G3-PLC are typically between 3 kHz to 490 kHz, which is much lower than the carrier frequencies in the broadband PLC standards.

Similarly to the G3-PLC standard, the PRIME standard, by PRIME Alliance consortium, is a PLC standard for the "Advanced Meter Management & Smart Grid" [123].

As previously mentioned, PLC channels are susceptible to multipath interference, which arises from signal reflections, diffraction, and scattering. This multipath interference occurs when the transmitted signal reaches the receiver through multiple paths, resulting in delayed and attenuated versions of the original signal. This phenomenon leads to intersymbol interference (ISI) and degradation of the received signal quality [124]. The choice of multiplexing scheme in PLC systems is critical to mitigate the effects of multipath interference and ensure reliable data transmission. The PLC standards already mentioned in this section aim to provide robustness against ISI. As explained previously, the use of OFDM is common in PLC standards as its division of the communication signal into multiple narrowband subcarriers makes it robust against ISI caused by multipath interference. The subcarriers can be individually equalized to mitigate the effects of multipath interference, ensuring reliable data transmission.

Adaptive modulation techniques offer another approach to mitigate multipath

interference. These techniques dynamically adjust the modulation scheme based on the channel conditions. By continuously monitoring the channel characteristics, such as signal strength and multipath interference, the QAM order (explained further in Section 2.9) could be decreased or increased to optimize data transmission performance.

The selection of an appropriate modulation and multiplexing scheme in PLC systems considers the trade-off between spectral efficiency, robustness against multipath interference, and implementation complexity. By carefully analysing the multipath properties of the channel and choosing a modulation scheme that effectively combats multipath interference, PLC systems can achieve reliable and efficient data transmission over power lines.

In this thesis, the PLC will consider the use of the bus bar within a battery as a communication medium.

2.7.1 Noise Modelling

Noise is a significant factor in PLC channels that can degrade the quality of transmitted signals and affect the overall system performance. Understanding and accurately modelling the noise characteristics in PLC channels are crucial for designing robust communication systems. This noise that can affect the PLC channel can be categorised as coloured background noise (e.g. white noise), narrowband noise, periodic impulse noise asynchronous to the mains frequency, periodic impulsive noise synchronous to the mains frequency, and asynchronous impulsive noise, which are further explained in [125]. It is assumed that coloured background noise, narrowband noise, and periodic impulse noise asynchronous to the mains frequency form background noise as they do not change for lengthy periods of time, such as minutes or hours. Narrowband noise can be caused due to electromagnetic interference (EMI) caused by nearby devices and other communication systems operating in the same frequency range.

On the other hand, the periodic impulsive noise synchronous to the mains frequency and asynchronous impulsive noise are considered to be impulsive noise as they can change in the microsecond and millisecond range. Impulsive noise in PLC channels can be sourced from switching devices, electrical appliances, and external electromagnetic interference and manifests as short-duration and high-amplitude

disturbance that can significantly disrupt the received signal.

These various types of noise are defined as follows [126]:

Coloured background noise

Originates from incidental radiations emitted by typical household appliances and equipment. The power spectral density (PSD), the distribution of power across different frequencies in a signal, of this noise diminishes as the frequency increases, with a notable concentration observed below the 1 MHz range [127].

Narrow-band noise

Arises from broadcast radio signals, resulting in concentrated power within a limited bandwidth and fluctuates over the course of a day.

Periodic impulsive noise synchronous with the mains frequency

Short duration of noise originating from power supplies, usually due to switching rectified diodes. The frequency is that of the power mains or electric grid, such as 50 Hz or 60 Hz.

Periodic impulsive noise asynchronous with the mains frequency

Caused by switching power supplies and by AC/DC power converters and range between 50 kHz to 200 kHz [128].

Non-periodic asynchronous impulsive noise

Non-periodic and unpredictable noise caused by switching transients. Due to the irregular nature of this noise, it is challenging to anticipate and synchronise with impulse events.

An OFDM-based narrowband PLC system has been designed and tested within the frequency band of 42 kHz to 471 kHz to determine the background noise of the communication channel, and offers a noise reduction algorithm that reduces bit error ratio (BER) by approximately 35 % [128].

The effects of impulsive noise on the PLC channel has been modelled and analysed in [129] for the frequency range of 0.2 MHz to 20 MHz. It has been shown that noise was the most crucial factor in the performance of high-speed PLC networks. The increase in noise power could cause errors in data transmission in few instances

where a burst of noise exceeds 10 ms. It has been concluded that PLC systems must utilise the following features in order to reduce the impact of impulse noise:

- Sophisticated frame structures with well-adapted and balanced interleaving
- Forward error correction, such as by using error correcting code (ECC)
- Error detection
- Automatic repeat request (ARQ) schemes

2.8 In-Situ Battery Power Line Communication

As explained in Section 2.7, the HomePlug standard was introduced to overcome the harsh environment of the power line network within homes and building due to varying loads, conductor types, and paths. Similarly, a large-scale battery system within a BEV also suffers from the same properties that make the channel a harsh environment for PLC. However, as previously mentioned, PLC does not require an additional wire harness as the existing power bus is utilised for communication. In Section 2.5, methods of communication within a battery that require additional wire harnesses have been introduced, including a two-wire system [111]. In this section, the existing literature on communication methods within battery systems that do not require additional wiring harnesses are described. Because a wiring harness is not required, these systems are lighter in weight and less complicated to implement.

Similarly to the wireless communication approach as already described in Section 2.5, no additional wire harness is required within the battery for smart cell PLC. For instance, an instrumented smart cell system utilising PLC with four cylindrical 21700 model Li-ion cells arranged into two cells in parallel and two cells in series has been presented in [40]. In this study, bi-directional communication was demonstrated using an off-the-shelf PLC modem capable of carrier frequencies of 1 MHz to 5 MHz with a data rate up to 500 kbps during drive cycle experimentation and cell cycling. This PLC system was tested at cell SoCs of 100 %, 80 %, 50 % and 30 %. In [130], an instrumented Li-ion pouch cell was tested with an in-situ PLC system using a carrier frequency of 6.5 MHz. This system utilised a microprocessor and PLC transceiver and

Table 2.5: Comparison of smart battery communication methods.

Smart Battery Network Topology	Wire Harness Requirements	Complexity & Cost	Comments
None	One wire to each embedded sensor within each cell to an external BMS	High	The number of wires required for a battery of many smart cells to connected in this way adds significant weight, cost, and complexity to the battery system.
Two-Wire	Two wires to each smart cell	Medium	Two wires will add a small amount of weight and complexity to the system.
Wireless	None	Medium	Performance of the wireless network may be degraded due to the shielding caused by other cells in the battery. Modifications to the smart cell required to integrate a wireless antenna increase the complexity and cost of this method. This technique requires further research for its suitability in batteries.
PLC	None	Low	The bus-bar is used as the communication channel. This technique is under investigation in this thesis for its suitability in Li-ion batteries. The cost of this technique depends on the modem required.

was embedded within the Li-ion pouch cell during cell manufacture. This work has also shown that PLC had no effect on the electrochemical performance of the cell. In another work, four fully charged 18650-model Li-ion cells have been tested within a PLC system using three combinations of capacitive coupling techniques with two different cell brands, measuring the system impedance and received signal strength using a vector network analyser (VNA) and spectrum analyser, respectively [131]. In addition, carrier frequencies of 1 MHz to 3 GHz were tested, and it was found that the maximum signal attenuation was 65 dB. In [132], a VNA has been used to perform measurements on the scattering parameter S21 for a single Li-ion cell in a shunt-through configuration for frequencies of 1 kHz to 300 MHz. The cell impedance and the insertion loss were calculated using the recorded S21 transmission coefficient, and it was determined that the cell impedance had reached 40 Ω at 300 MHz.

In the following chapters, the effects of Li-ion cells on an in-situ battery PLC system will be shown, with a maximum carrier frequency of 6 GHz, using a vector signal transceiver (VST) to determine real PLC performance. Moreover, the use of QAM as a modern modulation scheme for high data throughput is evaluated for this system, of which such analysis has not yet been seen.

In addition, the Li-ion cells will be characterised as a communication channel through utilising a VNA to measure S21 scattering parameter. This study includes the analysis and draws a comparison with the performance of PLC on four distinct battery configurations alongside six different SoCs to enhance the reliability of the obtained data. This is in stark contrast to existing academic research works that only focus on the sole analysis of single arrangement of cells and fewer SoCs tested. A comparison of existing literature on in-situ Li-ion battery PLC is presented in Table 2.6.

Table 2.6: Summary of existing works on in-situ Li-ion battery PLC systems.

Experimental summary	Battery configurations	Communication parameters	Reference
Integration of a commercial PLC modem and temperature sensor within a Li-ion cell for a smart cell network.	2S2P	5 MHz, OOK, TI THVD8000 [133]	[40]
Use of existing commercial RF transceivers for high frequency PLC within batteries using capacitive coupling.	4S, 4P	868 MHz, TI CC1200 [134] and 2.4 GHz, TI CC2520 [135]	[136]
Implementation of an in-situ Li-ion PLC system for the purpose of integration within the cell during manufacture using a commercial PLC modem.	Single Cell	6.5 MHz, Yamar SIG60 [137]	[130]
Use of PLC in a system of four Li-ion cells to communicate cell sensor data to an external data logging system and verified using additional CAN and USB communication using a commercial PLC modem.	2S2P	5 MHz, OOK, TI THVD8000 [133]	[138]
Li-ion battery channel characterisation for an in-situ battery PLC system.	Single Cell	0.1 - 1000 MHz	[139]

Communication of cell instrumentation data to an external data logging system using a commercial PLC modem and wired serial connection to each cell.	4S2P	6.5 MHz, Yamar SIG60 [137]	[140]
Demonstration of communication between two PLC modems within a small-scale Li-ion battery pack.	6S	1-30 MHz, OOK	[141]
Li-ion battery modelling and PLC channel characterisation up to 30 MHz for simulation, verified using a real implementation using two PLC modems.	28 Cells	10 MHz, FSK	[142]
Performance analysis simulation of an in-situ battery PLC with QAM under a BEV driving load profile.	2S, 2P	0.1 - 200 MHz, QAM	Chapter 4
Performance of PLC and QAM with SoCs using a VST and VNA for in-situ battery communication performance and channel analysis, respectively.	SoCs of 20, 40, 60, 80, 95 %	10 - 6000 MHz, QAM	Chapter 5
Performance of PLC and QAM with varying battery configurations and SoCs using a VST and VNA for in-situ battery communication performance and channel analysis, respectively.	Single Cell, 2S, 2P, 2S2P	10 - 6000 MHz, QAM	Chapter 6

2.9 Quadrature Amplitude Modulation

QAM is a modulation scheme that utilises variations in both amplitude and phase of a carrier signal. By manipulating the amplitude and phase of the carrier signal, QAM allows for the efficient encoding of data, facilitating high data rates and improved spectral efficiency in comparison to alternative modulation schemes, such as FSK and amplitude shift keying (ASK). Due to these features, existing PLC standards such as HomePlug AV and IEEE 1901 discussed in Section 2.8 also make use of QAM.

The QAM modulation order is defined as 2 to the power of the number of transmitted bits per QAM-symbol, whereby for instance 16-QAM uses 4 bits of data in each symbol ($2^4 = 16$), allowing for 16 possible values per symbol. These QAM-symbols can be represented using a constellation diagram, which shows the relationship between the symbol and the in-phase (I) and quadrature (Q) components of the carrier signal [143]. This diagram uses I and Q to represent the in-phase and quadrature of QAM-symbols, which in turn depict the amplitudes of the cosine and sine components of the symbol, respectively [144]. These I and Q components are then vectorially summed to produce the resulting amplitude and phase of the QAM symbol. An example of a constellation diagram is provided in Figure 3.6a. Each QAM symbol in the constellation diagram corresponds to a specific combination of amplitude and phase, representing a unique set of data. The higher the modulation order of QAM the higher the data rate as the number of data bits represented by each symbol also increases. As previously mentioned in Section 2.7, HomePlug AV2 allows for up to 4096-QAM. However, the higher orders of QAM are also more susceptible to noise and channel impairments. Therefore, achieving a balance between data rate and error performance is a critical challenge in QAM-based systems.

The QAM signal $s_i(t)$ can be expressed as

$$s_i(t) = A_i \cos\left(2\pi f_c t + \phi_i\right), \quad i = 1, 2, \ldots, M \tag{2.1}$$

where A_i is the amplitude, ϕ_i is the phase of the ith signal with the M-ary modulation order. For improving the spectrum with pulse shaping, the QAM signal can be represented as

$$s_i(t) = A_i p(t) \cos\left(2\pi f_c t + \phi_i\right), \quad i = 1, 2, \ldots, M \tag{2.2}$$

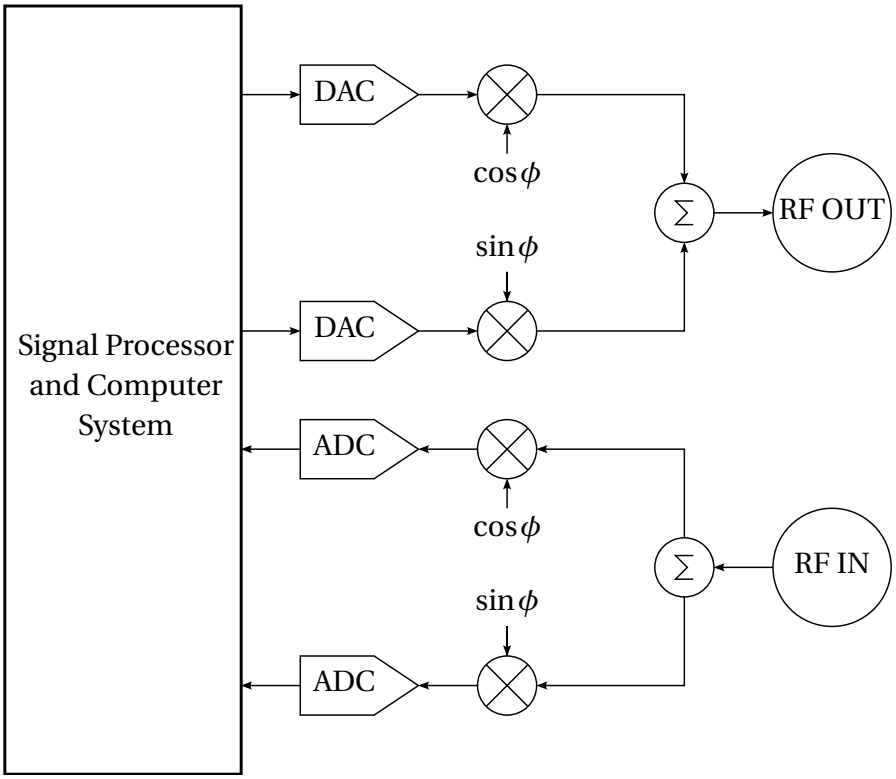

Figure 2.2: Overview of VST architecture [147].

where $p(t)$ is a smooth pulse defined as on [0,T]. By expansion of Equation (2.2), it can be written as

$$s_i(t) = A_{i1}\,p(t)\cos\left(2\pi f_c t\right) - A_{i2}\,p(t)\sin\left(2\pi f_c t\right) \tag{2.3}$$

where, $i = 1,2,\ldots,M$, and

$$A_{i1} = A_i \cos\phi_i \tag{2.4}$$

$$A_{i2} = A_i \sin\phi_i \tag{2.5}$$

The in-phase (I) and quadrature (Q) components of the QAM constellation are represented on axes using $p(t)\cos 2\pi f_c t$ and $-p(t)\sin 2\pi f_c t$, respectively. Further details of QAM can be found in established literature, including [145], [146].

An overview of the hardware architecture for a VST that modulates and demodulates QAM data streams is shown in Figure 2.2. The VST shown is very similar to the PXIe-5840 used in this research and discussed in more detail in Chapter 3. The

RF OUT part of the diagram shows the I/Q modulation, which are orthogonal, and the summing stage to the output port.

2.10 Synchronisation

Synchronisation is the process of ensuring that the transmitter and receiver are aligned in time and clock frequency. This is necessary in order for the receiver to decode the QAM symbols correctly. Time synchronisation ensures that the transmitter and receiver are sampling the signal at the same time, and frequency synchronisation ensures that the transmitter and receiver are tuned to the same frequency. Various methods exist for performing synchronisation. In this research, pilot symbols and phase-locked loops (PLLs) are used to perform synchronisation. As explained later in Section 3.3, these techniques are used for the QAM symbols to be correctly decoded by the receiver.

Pilot symbols are a sequence of reference symbols that are known to the receiver and that are inserted into the data stream transmitted [148]. These pilot symbols are used to mitigate the effects of multipath fading and phase distortion, which can degrade the performance of QAM communication. The effects of pilot symbols on the BER of 16-QAM data communication have been demonstrated in [149] whereby the increased number of pilot symbols showed improved communication performance. To obtain an improved estimated accuracy on channel characteristics, the pilot symbols are typically transmitted periodically with the data [148].

The PLL is a feedback control system that adjusts the phase and frequency of a local oscillator to match that of an incoming signal [150]. By comparing the phase of the received signal with the local oscillator's phase, the PLL adjusts the oscillator's frequency and phase to achieve synchronisation. The PLL continuously tracks and adjusts the local oscillator's phase to match the received signal, ensuring accurate symbol timing and carrier phase recovery.

2.11 Channel Capacity

Achieving high data rates while ensuring reliable transmission is a crucial objective in communication systems. However, this goal is often hindered by the inherent trade-off

between the signal to noise ratio (SNR) and the achievable data rate. The understanding of this trade-off is summarised by Shannon's information theory, which provides a mathematical framework for understanding the concept of channel capacity [151]. Shannon's equations define the maximum data rate that can be transmitted over a communication channel without error, given the SNR of the channel. The channel capacity is given by the Channel Capacity Theorem

$$C = B\log_2(1 + \text{SNR}) \tag{2.6}$$

where C is the channel capacity in bits per second, B is the bandwidth of the channel in Hertz, and SNR is the signal to noise ratio. The proof of this theorem is given in [152].

The SNR represents the ratio of the power of the transmitted signal to the power of the background noise in the channel. The various forms of background noise on the communication channel have been discussed in Section 2.7.1. The SNR determines the quality of the received signal and the impacts to the achievable data rate. Hence, a higher SNR indicates a stronger signal relative to the noise, resulting in better communication performance. Conversely, a reduced SNR means that it is challenging to reliably decode the transmitted data without first reducing the noise, and so the communication error, such as BER, will begin to increase [153]. To this end, the relationship between SNR and data rate is inversely proportional, whereby reducing the SNR in Equation (2.6) causes the channel capacity to approach 1. On the other hand, as the SNR increases, the logarithmic value grows, leading to a higher channel capacity.

Increasing the channel bandwidth B in Equation (2.6) allows for a higher data rate since more QAM symbols can be transmitted within a given time. However, this increased bandwidth also means a wider frequency range, which may result in more noise being present in the channel. Consequently, the SNR may decrease, limiting the achievable data rate. This therefore exists as a trade-off between bandwidth and SNR in determining the channel capacity.

2.12 Conclusions

This chapter has provided a thorough literature review on the technologies related to the research that is presented in this thesis, including existing smart battery technologies. In particular, the progress of battery research in recent times has been presented with an overview of how this topic may be further advanced to improve Li-ion battery performance. In the following chapters, these techniques in smart cell communication are utilised and further advanced to present novel research and findings on this topic.

Chapter 3

Experimental Details

In this chapter, the details relevant to all experiments and studies presented in this thesis are described. These experimental procedures are performed for channel characterisation of the lithium-ion (Li-ion) cell and in-situ power line communication (PLC) performance when used with quadrature amplitude modulation (QAM) in a simulated drive cycle scenario in Chapter 4, with changes to battery state of charge (SoC) in Chapter 5, and with changing battery configuration in Chapter 6. In addition, this chapter introduces the concepts of error vector magnitude (EVM), bit error ratio (BER) and symbol error ratio (SER) which are used to quantify the performance of the communication system within this experimentation. Subsequently, the measurements are used to determine the expected communication performance of an in-situ Li-ion battery PLC system and the suitability of such a system when used within systems that require large-scale batteries, such as battery electric vehicles (BEVs) and smart grids.

The methodology outlined in this section is used to determine the most appropriate channel bandwidth based on communication error analysis and scattering parameter results that demonstrate little multipath interference with carrier frequency on the communication channel. The selection of the channel bandwidth for an in-situ battery PLC system is key to determining suitable communication channel parameters, including QAM order, and the use of filtering, such as signal repeaters. In addition, the number of orthogonal carriers within the orthogonal frequency division multiplexing (OFDM) modulation scheme may also be determined based upon these parameters.

3.1 Electrochemical Impedance Spectroscopy

electrochemical impedance spectroscopy (EIS) is a technique used to measure the impedance of a system as a function of the frequency of an AC-current or voltage. The impedance of Li-ion cells is used to estimate various characteristics useful for SoC and state of health (SoH) estimation, the monitoring of internal temperature, and characterisation for second-life applications [154]. This analysis of the Li-ion cell allows for further understanding of cell degradation and is therefore useful in investigating limitations of Li-ion performance. A critical review of using EIS for the Li-ion characterisation of cell ageing can be found in [155].

An electrical impedance Z contains a real and an imaginary component in the form of the resistance R and reactance X. In using the impedance and phase measurement data from an EIS, first the reactance X is calculated using the impedance Z and the phase ϕ between Z and R. Their relationship is given by

$$X = |Z| \sin \phi \tag{3.1}$$

Then, the internal cell resistance R is calculated from the impedance and reactance, and the relationship is expressed as

$$R = \sqrt{Z^2 - X^2} \tag{3.2}$$

To perform EIS on a cell, a potentiostat or a galvanostat is used, whereby either the voltage or current is kept constant between the working electrode and the reference electrode, respectively [156]–[158]. A sine wave at a selected frequency is applied to the device under test, and the voltage or current drop of the signal across the cell is measured. By using $V(\omega) = I(\omega)Z(\omega)$ (or $I(\omega) = V(\omega)/Z(\omega)$) where ω is the angular frequency, the impedance of the system is determined. The phase shift of the sine wave is also measured to obtain X using Equation (3.1).

EIS measurements of Li-ion cells include pulsing the cell at low frequencies, typically between 10 mHz to 5 kHz to determine the cell impedance [159]. To achieve an appropriate symbol rate of at least 100 kbps in a prospective communication system, it is expected that the carrier frequency is at least two orders of magnitudes higher than that used in typical EIS applications of 0.1 Hz to 100 kHz [157]. This research

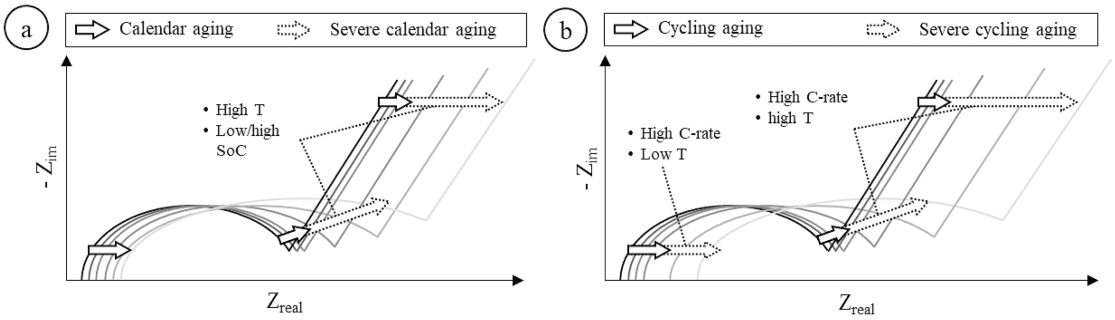

Figure 3.1: The effects of calendar ageing (a) and cycling ageing (b) on the impedance characteristic of a Li-ion cell presented in a Nyquist plot [155]. The dotted arrows emphasise increased ageing due to the effects of high and low temperature, high and low SoC, and high C-rate, as labelled.

study therefore considers carrier frequencies above 100 kHz to determine the best obtainable parameters possible for an in-situ Li-ion energy storage PLC system with respect to given symbol rates and noise rejection performance.

The impedance measurements are normally presented in a Nyquist plot, which shows the impedance, phase angle, reactance and internal resistance of the system tested. Figure 3.1 displays how the Nyquist plot can be used to determine the SoH of Li-ion cells and how these may change with calendar and cycling ageing, and further accelerated with high temperature and charge rate (C-rate).

Performing an EIS on batteries generally requires bespoke equipment to ensure that the batteries are not damaged during measurement, for instance, due to current draw. This equipment has mainly been designed for rather low frequency EIS for the common purposes of cell degradation analysis. Therefore, measuring the EIS of batteries at frequencies above 100 kHz is a challenge.

Preliminary EIS measurements of the Li-ion were performed using the Solartron Analytical ModuLab XM MTS. However, our experimental study showed that these measurements were limited to a maximum frequency of 100 kHz. Hence, alternative methods of performing EIS, such as by using custom circuit designs and fabrication, are followed in this research to complete these high frequency measurements.

The methodology of performing high frequency EIS on Li-ion cells described above is a means to achieving the main focus of this research, that is, on the results of such measurements, which are required to fulfil the objectives of the communication

performance analysis. Based on these facts, in Chapter 4 existing high frequency EIS measurements of Li-ion cells are used to perform the simulations and analysis required to accomplish the research objectives. However, in chapters 5 and 6, measurements and analysis of scattering parameters are performed for analysis of the Li-ion cell as a PLC channel, as will be discussed in Section 3.2.

3.2 Scattering Parameters

To determine the effectiveness of a Li-ion cell as an effective communication channel for PLC, an analysis of the system scattering parameter transmission coefficient can be performed as an alternative to determining the system's impedance with EIS. The transmission coefficient of the PLC channel allows for the analysis of signal attenuation and phase shift imposed onto the signal by the channel. As already explained in Section 2.7, the multipath effects of the PLC channel can cause destructive and constructive interference. Because of this multipath interference, both the phase shift and the S21 magnitude change with carrier frequency not only due to the change in impedance of the Li-ion cell, but also due to the PLC signal taking different paths and recombining at the receiver. Hence, measuring the transmission coefficient of the Li-ion cell at various carrier frequencies enables finding the most appropriate parameters of the PLC system, including carrier frequency, filter requirements, and QAM order. The use of QAM is detailed in Section 3.3. Such parameters will also take into account the changes in transmission coefficient caused by alterations in battery pack configuration and SoC. It is expected that a change in impedance, and hence the channel transmission coefficient, due to the configuration or SoC, may lead to variations in attenuation and phase shift, which as a consequence, influences data integrity as measured with EVM, BER, and SER. Further discussion is given in Section 3.3. Hence, for the most effective PLC parameters, the impedance magnitude and phase shift must remain the same throughout all SoCs and configurations tested.

The scattering parameter (S-parameter) S21 represents the forward transmission coefficient of the Li-ion cell as a communication channel. S21 is defined as the ratio of the wave transmitted by a vector network analyser (VNA) at port 1 to the measured wave at port 2. Other two-port S-parameters are S11, S12, and S22, where S12 is the

reverse transmission coefficient of the communication channel, and S11 and S22 are reflection transmission coefficients of the communication channel solely on port 1 and port 2, respectively. The series transmission impedance can be represented depending on the waveguide circuit theory of travelling waves and power waves [160]. Where for travelling waves, the series transmission impedance is given by

$$Z = 2e^{j\phi(Z_{0i})}\sqrt{\left|\frac{\mathrm{Re}(Z_{0i})}{\mathrm{Re}(Z_{0j})}\right|}\frac{\left|Z_{0j}\right|}{S_{ij}} - \left(Z_{0i} + Z_{0j}\right) \tag{3.3}$$

and for power waves the series transmission impedance is expressed by

$$Z = 2\mathrm{sgn}(\mathrm{Re}(Z_{0i}))\frac{\sqrt{\left|\mathrm{Re}(Z_{0i})\mathrm{Re}(Z_{0j})\right|}}{S_{ij}} - \left(Z_{0i} + Z_{0j}\right) \tag{3.4}$$

where sgn is the sign function defined as

$$\mathrm{sgn}\left(\mathrm{Re}(Z_{0i})\right) = \begin{cases} -1 & \text{for } \mathrm{Re}(Z_{0i}) < 0 \\ 0 & \text{for } \mathrm{Re}(Z_{0i}) = 0 \\ 1 & \text{for } \mathrm{Re}(Z_{0i}) > 0 \end{cases} \tag{3.5}$$

and i and j are physical port numbers 1 or 2, which denote the S parameter and Z impedance, and Z_{0i} and Z_{0j} are reference impedances at ports i and j, respectively. In addition, the parallel transmission impedance is given by

$$Z = \frac{Z_{0i}Z_{0j}S_{ij}}{2\left(Z_{0i}\left|\frac{Z_{0j}}{Z_{0i}}\right|\sqrt{\left|\frac{\mathrm{Re}(Z_{0i})}{\mathrm{Re}(Z_{0j})}\right|} - S_{ij}\frac{Z_{0i}+Z_{0j}}{2}\right)} \tag{3.6}$$

and for power waves the parallel transmission impedance is expressed by

$$Z = \frac{Z_{0j}S_{ij}}{\sqrt{\left|\frac{\mathrm{Re}(Z_{0i})}{\mathrm{Re}(Z_{0j})}\right|}\left(1 + e^{-2\phi(Z_{0i})}\right) - S_{ij}\left(1 + \frac{Z_{0j}}{Z_{0i}}\right)} \tag{3.7}$$

The experiments presented in chapters 5 and 6 perform and analyse S21 measurements of the Li-ion cell. The S21 transmission coefficient can be used to determine other features of the communication channel, such as the impedance and insertion loss. Let characteristic impedance Z_0 of the VNA be 50 Ω, then the impedance of the cell Z_{cell} is calculated by [132]

$$Z_{cell} = \frac{Z_0 S_{21}}{2(1 - S_{21})} \tag{3.8}$$

Insertion loss IL is given by

$$IL = 20\log_{10}|S_{21}| \tag{3.9}$$

Further details of scattering parameters can be found in [161]. Using the impedance calculated from S21 and the measured phase shift, it is possible to calculate the reactance and the internal resistance of the Li-ion under test. The relationships between them can be expressed as

$$\begin{aligned} |Z| &= \sqrt{R^2 + X^2} \\ X &= |Z|\sin\phi \\ R &= |Z|\cos\phi \end{aligned} \tag{3.10}$$

where $|Z|$, X and R, indicate impedance, reactance, and resistance, respectively.

In these experimental works, a Rohde & Schwarz (R&S) ZNA43 VNA as shown in Figure 3.2, is used to perform S21 measurements of the PLC channel. The VNA is configured to perform a sweep of S21 measurements over the frequency range from 10 MHz to 6 GHz. This sweep is performed 100 times for each SoC in order to reduce the impact of noise, interference, outliers after averaging, and ultimately to improve the accuracy of the results obtained.

The VNA is configured to record the S21 transmission coefficient using a calibration profile performed before commencing each experiment. This profile utilises both the R&S ZN-Z129 calibration kit and the cell holder, for a calibration profile spanning frequencies of 10 MHz to 40 GHz. The *One-Path Two-Port* calibration type is utilised for specific use with S11 and S21 measurements only, and uses it the open, short and match standards. This calibration profile allows for accurate S21 magnitude and phase measurements with the VNA. Other calibration types exist which feature different parameters depending on the applications [160].

It is observed that the cell holders and the Li-ion cell have a longer signal path, i.e. electrical length, than the ZN-Z129 calibration kit. Thus, the phase compensation applied by the VNA using the ZN-Z129 calibration profile will be inadequate to effectively compensate for the phase shift caused by the longer signal path. Therefore, the measured phase shift will include a linear background, which will be compensated for during data processing to obtain only the characteristics of Li-ion cell on the phase of the signal. This linear background has a constant slope for the full frequency range

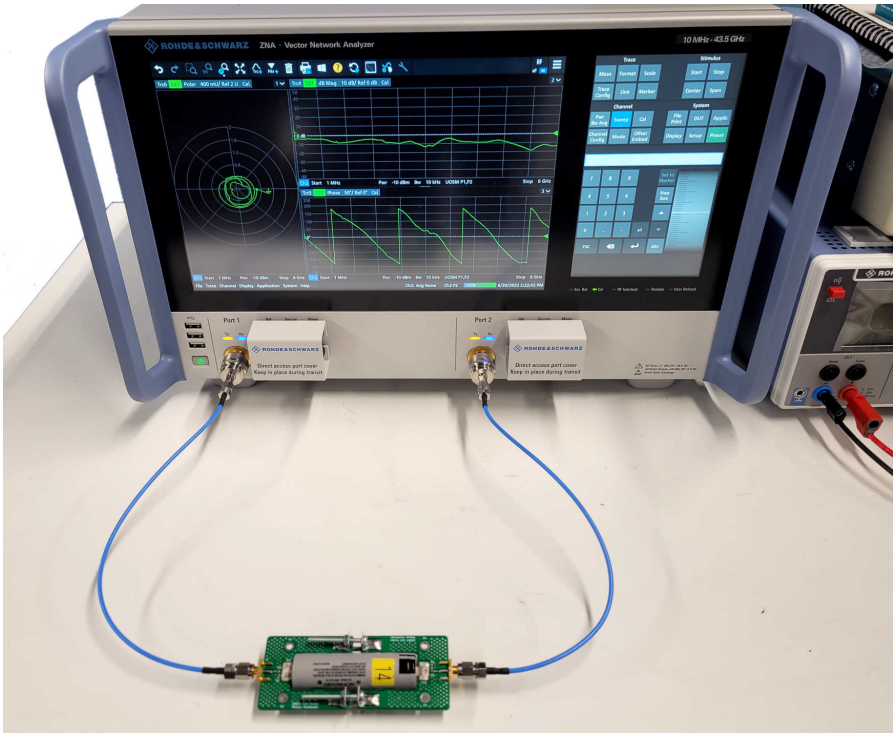

Figure 3.2: The connection of the Li-ion cell to the VNA. The Li-ion cell is clamped within the bespoke cell holder as described in Section 3.4.1.

considered, it includes any consistent background signal or noise, and its removal from phase shift data allows for the analysis of the underlying relevant information and features.

The linear background of the phase shift data is removed by first compensating for the sudden changes in phase from –180° to 180°, the mathematical extremes of the phase, and then determining the gradient between the phase shift at 80 MHz to 100 MHz carrier frequencies. These offsets are chosen due to a slight increase in noise at the lower frequencies between 10 MHz to 80 MHz which hinder the calculation of the gradient of the phase shift data. Because of this index offset of phase data used for the gradient calculation, the first and last phase shift values are not 0°. This method of removing the linear background allows for easier analysis of sudden changes in phase shift with carrier frequency. An example of how the linear background removal from the phase shift data can be helpful for analysis is shown in Figure 3.3. It can be seen from Figure 3.3b that the phase at 3.2 GHz suddenly increases significantly,

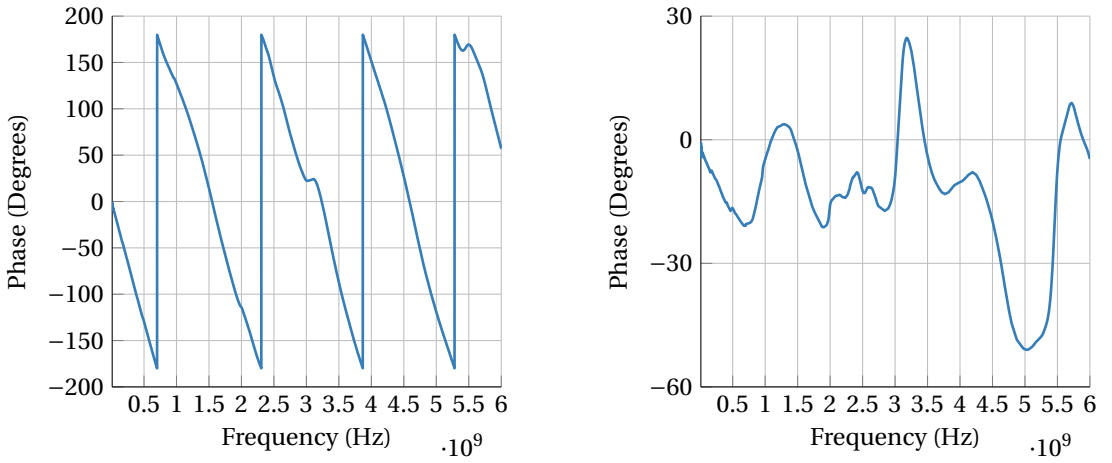

(a) Phase shift.

(b) Phase shift with linear background removed.

Figure 3.3: Phase shift caused by the longer signal path of the cell shown in (a) is compensated by removing the linear background to examine the effects on phase shift caused by the cell characteristics and not its length (b).

whereas removing the linear background only shows a relatively small increase in phase as shown in Figure 3.3a. The use of the gradient for linear background removal may also remove any real gradual phase shift that may be occurring for the full range of carrier frequencies tested. However, the effects of gradual phase shift are later known to be insignificant on the performance of the communication system during the experimental testing performed in Chapters 5 and 6.

Depending on whether a series or shunt-through cell holder is used, the VNA is connected to the cell holder such that the stimulus signal is transmitted through, or across the Li-ion cell, respectively. The differences between the series and shunt-through cell holders are further described in Sections 3.4.1 and 3.4.2, respectively.

The VNA is connected to the cell holder using a coaxial cable with 2.92 mm Sub-Miniature version A (SMA) connectors rated for frequencies up to 40 GHz. However, despite the 40 GHz rating of the VNA and the cable, the experiments performed within this research will limit the highest frequency tested to 6 GHz, as this is the maximum frequency that can be tested using the vector signal transceiver (VST), as will be introduced in Section 3.3. Similar to EIS experimentation, the measurements of S21 using the VNA can be used for impedance analysis.

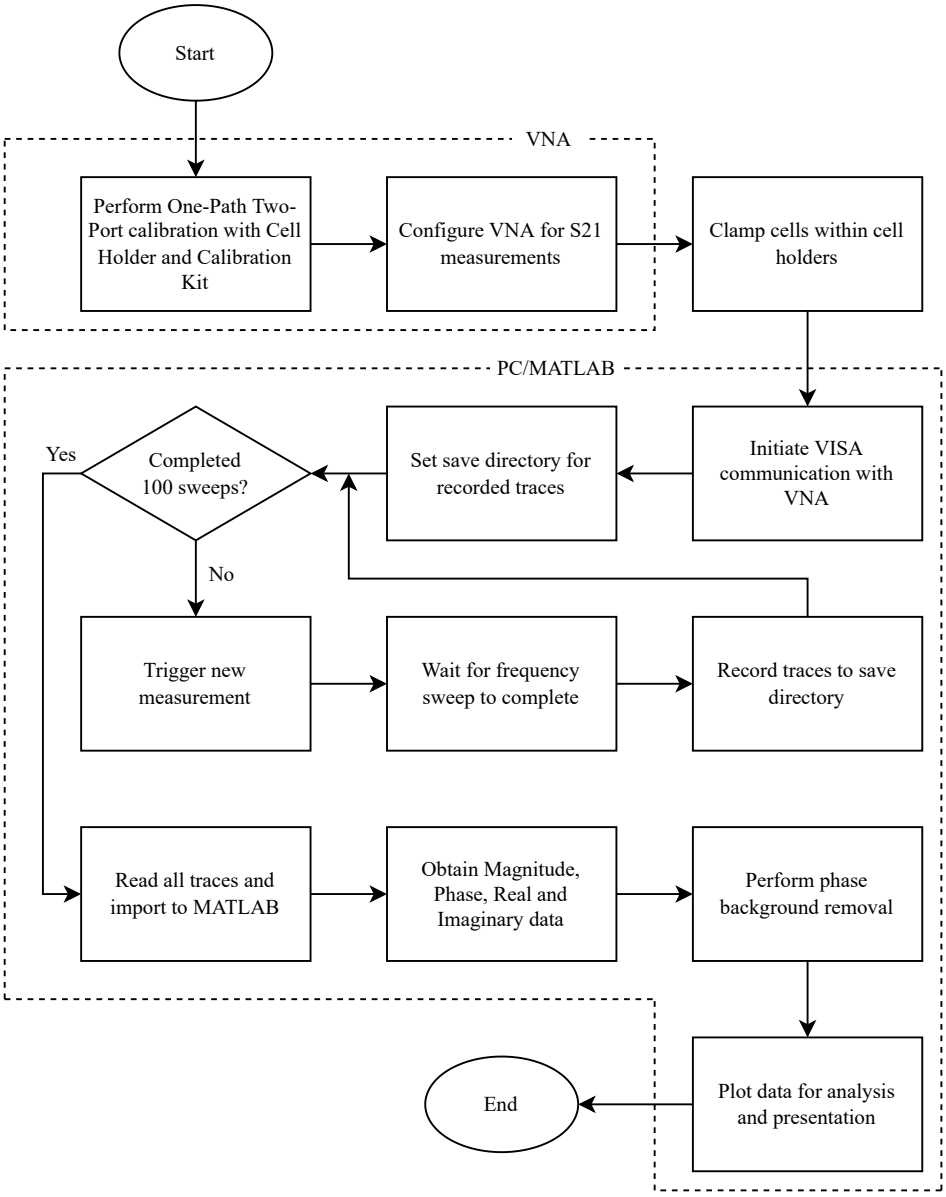

Figure 3.4: Flowchart of the experimental process for communication channel analysis.

Since the characteristics of the communication channel are the main topic under investigation in this work, measurements and analysis of S21 magnitude and phase are presented instead. It is expected that with decreasing S21 magnitude (and hence increasing insertion loss), the communication channel will become more unsuitable for use with PLC due to the decrease in signal to noise ratio. The relationship between the S21 magnitude and phase measurements with the suitability of the Li-ion cell as a communication channel is then verified using real PLC on the system. The associated experimental procedure is discussed in Section 3.3.

During these experiments, the S-parameters of the Li-ion cell will be the only varying property with changing configuration or SoC and the impedance characteristics of the experimental components, such as the cell holder, remain unchanged. Therefore, using a baseline measurement of the Li-ion cell S-parameters will remove the characteristic transmission coefficient of these constant experimental components, thereby presenting the change in S21 caused only by changes to the Li-ion battery configuration or SoC.

A flowchart of the overall experimental process for the scattering parameter measurements of the Li-ion cell is presented in Figure 3.4. The process of performing 100 sweeps in each experiment is expedited through a MATLAB script on a separate computer and a virtual instrument standard architecture (VISA) connection to the VNA for communication commands and status reports. Prior to performing the sweeps, the VNA is configured to perform a frequency sweep of S21 magnitude and phase, and a calibration is performed. After calibration and configuration of the VNA, and clamping of the Li-ion cells within the cell holders, the process of performing the 100 sweeps is automated using the MATLAB script. After the experiment, the data is imported into MATLAB for processing, linear background removal, and analysis.

3.3 Communication Error Analysis

The NI PXIe-5840 vector signal transceiver (VST) is used to perform real PLC testing of the battery with QAM orders from 4-QAM to 1024-QAM. Further discussion on QAM is given later in this section. The VST is configured to transmit a controlled trace of 100,000 QAM symbols with a symbol rate of 100 kHz at carrier frequencies of 10 MHz

to 6 GHz with a step size of 50 MHz. The step size used for the carrier frequency with the VST is higher than that configured with the VNA due to experimental time considerations. In these experimental works, OFDM is not used, and hence the spacing between subcarriers is not an objective of these investigations. As explained in Chapter 2, HomePlug uses 24.414 kHz spacing between subcarriers in OFDM. For simplicity and time considerations, the bandwidth of 100 kHz is used without loss of generality. Based on the findings of these experimental works, the most appropriate bandwidth for OFDM subcarriers can be determined.

The modulated signal is transmitted to the Li-ion battery at either an output power of –9 dBm or of –27 dBm. The experimental processes is then repeated for each output power selected. The maximum output power of –9 dBm is selected as it remains below the level at which the VST warns of overloading the input RF terminal after the RF signal has passed through the Li-ion cell, which may cause waveform clipping, signal corruption, and potential damage to the equipment. The much lower output power of –27 dBm is expected to cause a great increase in EVM, and highlight further susceptibility to changes in the PLC channel of the Li-ion cell under test.

The signal received on the VST input is demodulated into QAM symbols and further into bits of data. Then the QAM symbols are compared to the reference QAM constellation to obtain the root mean square (RMS) EVM. RMS EVM is explained in more detail later in this section. The decoded bits of data received are compared with the transmitted data to obtain the BER and SER.

As explained in Section 2.9, QAM uses both amplitude and phase for modulation for enhanced utilisation of the transmission channel.

The VST is configured to transmit 100,000 known QAM data symbols with a symbol rate of 100 kHz, and to receive the signal after it has passed through the Li-ion cell. These known data begin with pilot symbols that are used by the VST to perform normalisation and the phase compensation required for effective symbol trace demodulation. The use of pilot symbols for synchronisation has been previously discussed in Section 2.10. In this research, these pilot symbols are configured as consecutive QAM symbols in ascending Gray-code order. Following these pilot symbols are known random data modulated as QAM symbols. Due to the increasing number of symbols with higher modulation orders of QAM, the number of pilot symbols will

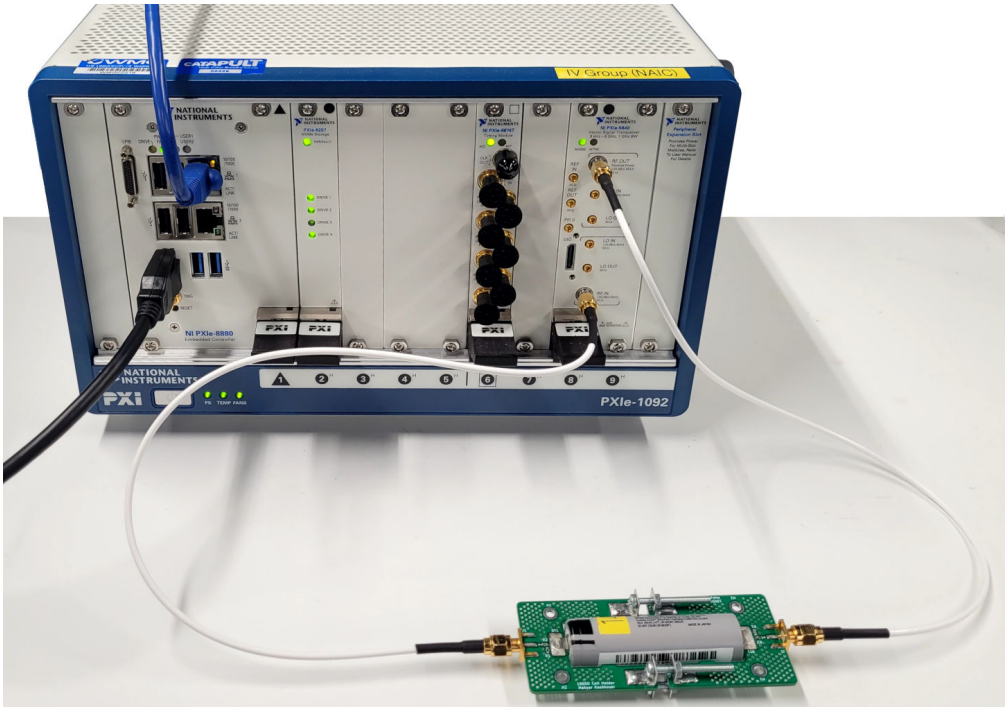

Figure 3.5: The Li-ion cell connected to the VST. The Li-ion cell is clamped within a bespoke cell holder as described in Section 3.4.1.

increase whilst the number of known random data will decrease. This will not affect the experimental procedure as the contents of these data are not influential on the results of this research.

The RF output of the VST is connected to the negative terminal of the Li-ion cell, and the positive terminal is connected to the RF input of the VST. The VST and the cell holder are connected via coaxial SMA cables rated to 12.4 GHz at a defined torque. The signal received is demodulated into data symbols that are then compared with the symbols transmitted. Comparison of the received data with the data transmitted enables one to calculate the BER and SER, which are ratio-metric comparisons of the corrupted bits and symbols within the data stream, respectively. Since each symbol contains multiple bits, it is observed that the SER will be equal to or greater than the BER for each test. Since the number of QAM data symbols transmitted is limited to 100,000, the lowest possible SER will therefore be 10^{-5}. This is because it is not appropriate to suggest that absolutely no symbol error is possible on the commu-

nication channel, as assuming the worst case, the 100,001th received symbol could be erroneous. Hence, when no symbol errors occur in this research, the theoretical minimum is presented instead. Furthermore, since the number of bits within QAM symbols of various modulation orders differ, the lowest theoretical BER changes. This can be calculated using

$$\text{Minimum BER} = \frac{1}{\text{Bits in QAM Symbol} \times \text{Number of QAM Symbols}} \tag{3.11}$$

where for 2-QAM, the lowest theoretical BER an experiment of 100,000 QAM symbols is $1/(2 \times 10^5) = 5 \times 10^{-6}$.

In addition to measuring BER and SER, the EVM is also calculated in each test, where EVM is a measurement of imperfections within a constellation plot against a reference symbol map. The calculation of the RMS EVM is given by

$$EVM_{RMS}(dB) = 10\log_{10}\left(\frac{\frac{1}{N}\sum_{k=1}^{N}\sqrt{(I_k - \tilde{I}_k)^2 + (Q_k - \tilde{Q}_k)^2}}{m_{\text{avg}}}\right) \tag{3.12}$$

where k is the symbol index, N is the number of symbols, I_k is the in-phase measurement of the kth symbol, Q_k is the quadrature measurement of the kth symbol, and m_{avg} is the average constellation magnitude. Note that $\tilde{I}_k$ and $\tilde{Q}_k$ represent measured symbols, whereas I_k and Q_k represent reference symbols.

The EVM increases as a symbol drifts further away from the reference symbol within a constellation plot. Such imperfections might be due to poor phase compensation or normalisation of the VST, which may be caused by significant phase distortion and attenuation by the Li-ion cell. Using EVM enables the performance measurement of the PLC channel in more precise detail, including in instances where the BER or SER do not show any important change. This behaviour occurs because of imperfections in received symbol data that may not be significant for the demodulator to produce corrupt data, but may be significant to become a cause for concern. These are instances whereby a QAM symbol may be sufficiently distorted to approach another reference symbol, and yet remain effectively separated so that the symbol is not demodulated incorrectly. Figures 3.6a and 3.6b display a reference 16-QAM constellation diagram with a perfect EVM, and an example constellation diagram of a noisier 16-QAM signal with an RMS EVM of –26.4 dB, respectively.

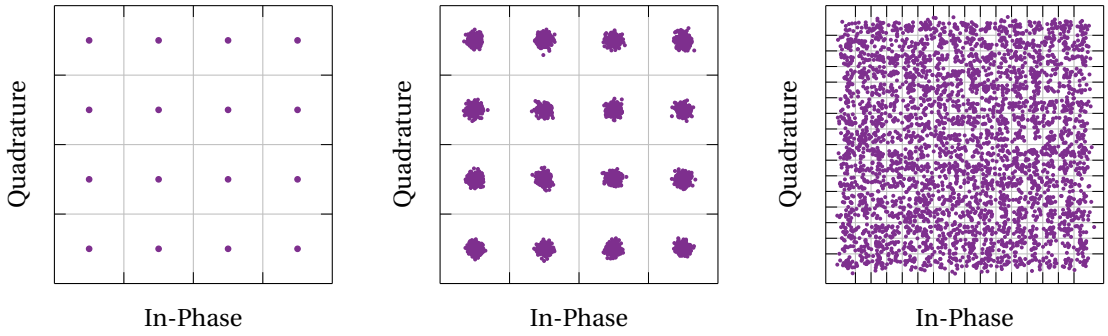

(a) 16-QAM reference constellation.

(b) 16-QAM signal with an EVM and BER/SER of –26.4 dB, and 0 , respectively.

(c) 256-QAM signal with an EVM and BER/SER of –25.6 dB, and 0.10 , respectively.

Figure 3.6: Constellation diagrams showing a reference 16-QAM constellation, and QAM signals with manually added noise. The same number of QAM symbols are tested in each figure. The grid lines depict the relative constellation sector boundaries.

Higher orders of QAM offer higher data rate as more bits can be transferred in each symbol. However, higher orders of QAM require an increased number of symbols on the constellation diagram, which consequently increases the susceptibility of data corruption due to noise. This potential corruption occurs because the QAM order is limited by the signal to noise ratio (SNR) of the PLC channel, which must be greater with increasing QAM order to differentiate between different QAM symbols on the constellation diagram [162]. For instance, it can be seen in the 256-QAM signal shown in Figure 3.6c, that artificially added additive white gaussian noise (AWGN) noise has a significant negative effect on the PLC system, resulting in increased EVM, bit and symbol errors, as symbols can easily move beyond their correct constellation sector. The boundaries of the constellation sectors are shown as grid lines in Figure 3.6, and these depict where a symbol changes its representation. Hence a symbol approaching a sector boundary has a high EVM, and a symbol crossing this boundary increases the SER.

A flowchart of the overall experimental process using the VST is presented in Figure 3.7. A custom program written in the C programming language has been created to perform the full experimentation with the VST. This program utilises the so-called NI RFmx [163] and RFSG [164] APIs, where the RFmx API is used for input signal configuration and demodulation, and the RFSG API is used for signal modulation and

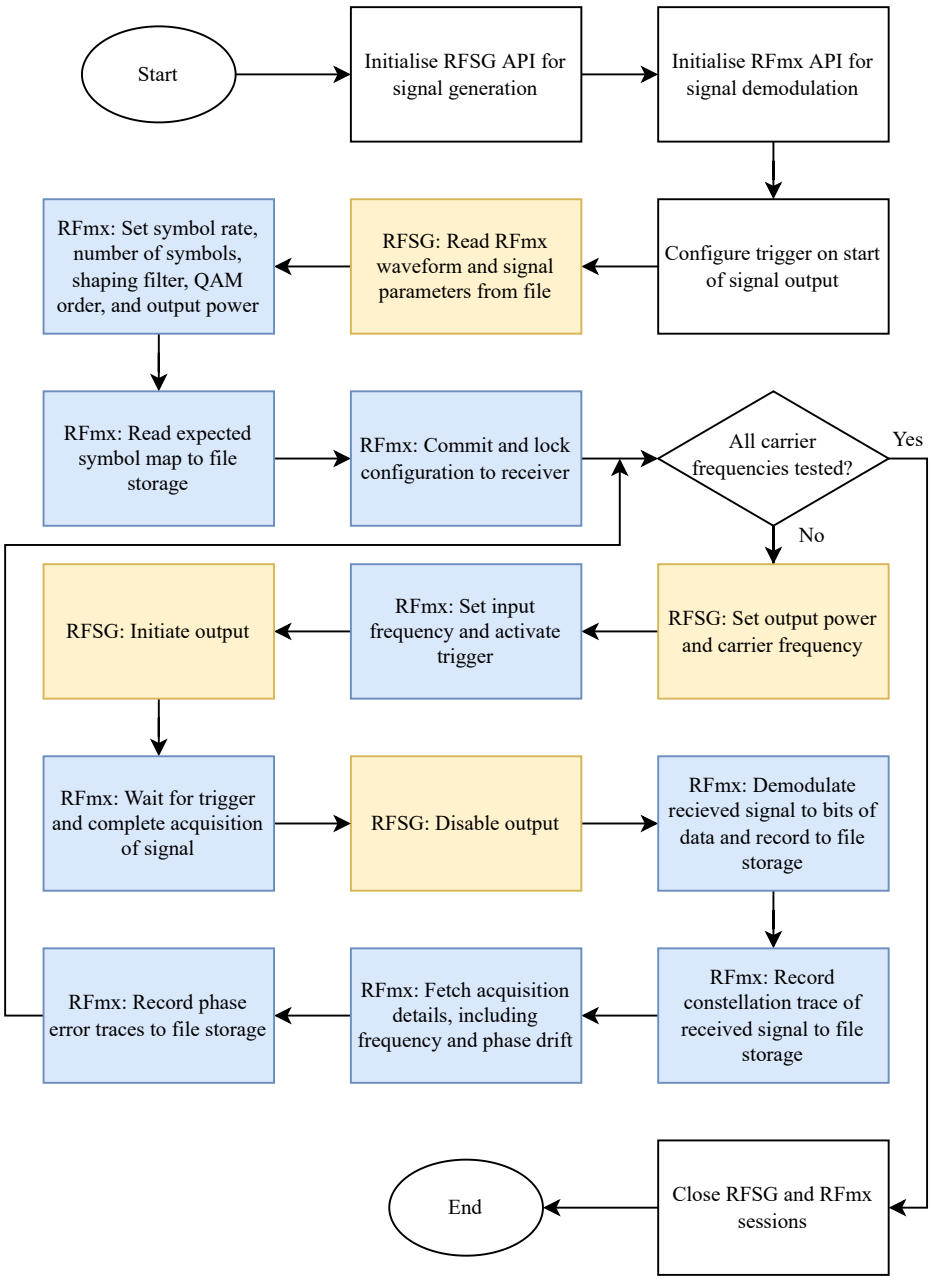

Figure 3.7: Flowchart of the technical experimental process with the VST. The processes involving transmitting and receiving the QAM data using NI APIs RFSG and RFmx are coloured orange and blue, respectively. The source code used to execute this process is provided in Appendix A.3.

Table 3.1: Definitions of the properties obtained from the experimental process with the VST.

Properties	Definition
Constellation Trace	Complex values of signal trace.
Demodulated Bits	Demodulated signal into binary bits of data.
RMS EVM	EVM of the vector error in the constellation trace.
Modulation Error Ratio (dB)	SNR of the constellation trace.
Frequency Offset (Hz)	The difference between the signal frequency and the expected frequency.
Frequency Drift (Hz)	Changes in frequency during signal acquisition.
Phase Error (Degrees)	The difference in phase between the constellation trace and the reference constellation.
IQ Gain Imbalance (dB)	Ratio of the gains of I and Q of the constellation trace.
Quadrature Skew	The orthogonal error of the I and Q components in the constellation trace.
IQ Origin Offset (dB)	The offset of the origin in the constellation trace compared to the reference origin.
Amplitude Droop (dB)	Mean change in amplitude in each symbol measurement window in the constellation trace.
Phase Error Trace (Degrees)	Mean phase error per symbol in constellation trace.

RF output. The waveforms that are output using the RFSG API have been previously generated using the 'RFmx Waveform Creator' for all the QAM orders tested. The results of the experiment are obtained from the RFmx API, and a full list of these properties are shown in Table 3.1.

3.4 Cell Holder

To improve the accuracy of all characterisation measurements, the construction and use of the measurement setup must be given careful consideration. The use of winding and unshielded signal paths, such as through a spring or an unshielded cable, may

cause irreproducible changes in inductance and capacitance, and thereby complicate the analysis of the measured signals. The requirements for an adequate Li-ion cell holder are therefore:

- Short and curved signal paths to reduce electromagnetic interference (EMI), as an alternative to right angle bends.
- Low capacitance and inductance signal traces and components to reduce the effects of reactance on the measurements.
- Stable mechanical connection to cell under test.
- High frequency-rated connectors.

Existing research has demonstrated the use of a bespoke cell holder for S21 measurements, such as in [132] where a cell holder was simulated and then used for shunt-through impedance measurements of a Li-ion cell from 1 kHz to 300 MHz. In [141], it has been explained that the shunt-through configuration is selected for its improved sensitivity in measurements when the Li-ion has a low impedance. However, in their experiment, direct current (DC) blocks were required to protect the measurement equipment from the DC current of the connected Li-ion cell.

In this thesis, both series-through and shunt-through cell holders are designed and used for the measurements of communication performance with SoC and battery configuration, respectively. The cell holders are designed to provide the option of using DC blocks for testing high voltages with the VNA and VST. However, the use of DC blocks is determined to be unnecessary as the maximum voltage of the battery under test is always below the maximum input voltage permitted on the VNA (±30 V) and VST (±10 V). It is important to ensure that the applied input voltage on the equipment is below the maximum input voltage rating, as exceeding this voltage may cause permanent damage to the equipment.

3.4.1 Series-Through Cell Holder

The first bespoke cell holder that is designed and constructed for particular use within the experiment of changing PLC performance with Li-ion SoC is shown in Figure 3.8.

Figure 3.8: The Li-ion cell clamped within the cell holder.

This cell holder is constructed of two separate printed circuit boards (PCBs) that form a clamp using four screws — two above and two below. A nickel-plated copper tab on the centre of each cell holder part provides a connection to the terminals of the Li-ion cell. The screws of the cell holder are tightened such that the tabs form a secure connection with the cell terminals, and that the cell is tightly secured within the clamp. Care is taken to ensure that the screws are not over-tightened, which may cause damage to the cell terminals. The Li-ion cell remains clamped within the cell holder under a fixed torque for the full duration of the experiment, including when changing SoC and cell configuration.

Each tab is connected to a signal path that optionally leads through resistors and then to an SMA connector. Both sides of the clamp use a $0\,\Omega$ resistor in series to create a bridged connection. This component has been added to the cell holder for the option of using capacitive coupling on either the input or the output of the cell by replacement with a similar-sized ceramic capacitor. However, capacitive coupling is not utilised on the cell holder in these experiments, but alternatively the alternating current (AC) coupling of the input to the VNA and VST is utilised.

Despite the small size of the resistors selected and hence their low power rating, it is not expected that the resistors will have a noticeable effect on the S21 measurements. Since both the VNA and the VST use a high impedance input, the power draw from the cell should be minimal. Therefore, the current passing through these resistors is expected to be very low. The resistors selected are *thin-film* resistors, which offer negligible effects on the overall circuit's impedance.

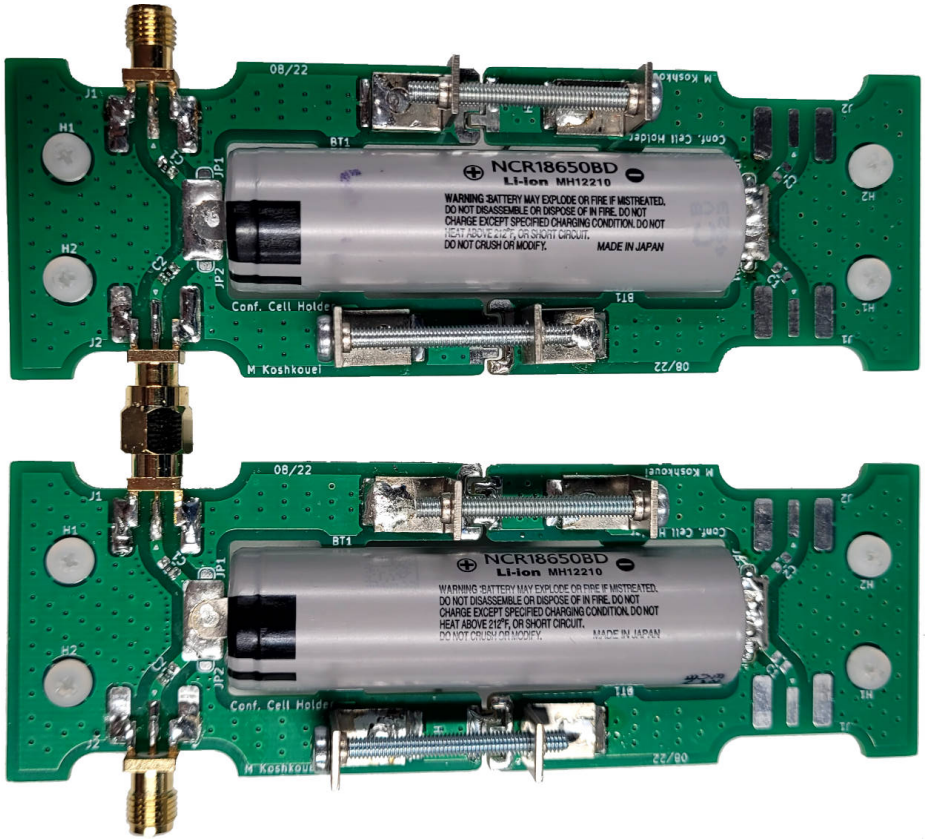

Figure 3.9: Cell holders connected in 2P shunt-through configuration.

The signal paths on the cell holder's PCBs are as short as possible to reduce the effects of EMI on the signal. To this end, further techniques include the rounding of footprint edges and using large ground planes on both sides of the PCB that are connected using 'via stitching'. In addition, all screw holes are grounded for further mitigation of EMI on the cell holder. The circuit and PCB layout of the series-through cell holder are presented in Appendix A.1.

3.4.2 Shunt-Through Configurable Cell Holder

This shunt-through cell holder has been designed to simplify the connection with other cell holders, making cell reconfiguration a more simplified process. Hence, this configurable cell holder has been selected for particular use for testing various configurations of Li-ion batteries, as cells can be added and removed in series and

parallel to form the battery pack required. The design of the cell holder reduces the effect of EMI on the signal, which includes using short traces and via stitching on the ground plane. The circuit and PCB layout of the shunt-through configurable cell holder are presented in Appendix A.2. This design utilises findings based on simulations and measurements presented in [141], whereby a single cell shunt-through PCB fixture was tested up to 300 MHz for measuring cell impedance.

The shunt-through configuration is used because of the increased accuracy in measuring low-ohmic impedances [139]. Furthermore, this configuration allows for testing of the communication performance across a bus bar within a large battery pack. In the employed shunt-through configuration the negative terminal of the Li-ion cell is connected to ground. It is therefore expected that a decrease in internal resistance of the Li-ion cell will increase the attenuation of the signal. The effects of the Li-ion cell internal resistance on the shunt-through configuration is explained in more detail in Section 6.1.

3.5 Conclusions

This chapter has provided the experimental details relevant to the three main contributions that are presented in Chapters 4 to 6. The details presented herewith show the relationships between them and how they enable the delivery of the main aim of the research presented in this thesis. This is namely the performance evaluation of a PLC system through Li-ion cells and determining the appropriate parameters for such a system.

Chapter 4

Simulation of a QAM-based Power Line Communication System for Lithium-ion Batteries

In this chapter, the results of an electrochemical impedance spectroscopy (EIS) on two lithium-ion (Li-ion) cells configured in series and parallel are obtained from the existing literature and exploited within this experimentation to create a realistic battery model for the purposes of analysing and demonstrating an in-situ battery power line communication (PLC) system. This model is used with a real dynamic drive profile to simulate the effects of a driving battery electric vehicle (BEV) on the performance of an in-situ PLC system. The simulation is further enhanced by applying the noise expected within a typical BEV energy storage system. The simulation of a PLC system utilising carrier frequencies of 100 kHz to 200 MHz and the use of quadrature amplitude modulation (QAM) for high data throughput are additional contributions to the research community.

These simulations reveal that the performance of the PLC system is heavily dependant on the selected carrier frequency due to the significant changes in reactance and internal resistance of the Li-ion cells tested. Furthermore, cells placed in parallel display a decreased performance compared to cells in series. The results highlight that the optimal carrier frequency for in-situ QAM-based PLC system for a Li-ion battery system is 30 MHz, and that additional signal conditioning is required for 4-QAM and

higher modulation orders.

In addition, this experimental work demonstrates the ability to measure the expected performance of a PLC system within a particular battery design architecture using a battery model and simulation. This technique allows for supporting battery architecture design for the purpose of creating a smart battery system that utilises a PLC system. For the particular Li-ion cells tested within this experimental work, it is shown that the addition of cells in parallel deteriorates the performance of the PLC system. Hence, these facts can be exploited during battery architecture design to select an appropriate number of cells in parallel as required by the target system, but not so much to impair the performance of the in-situ battery PLC network.

4.1 Experimental Details

As discussed in Chapter 3, the EIS of Li-ion cells is used to estimate various characteristics useful for degradation mitigation. Typically, an EIS is performed at low frequencies between 1 mHz to 10 kHz in order to perform such characterisation of Li-ion cells [159]. However, these low frequencies of Ultra Narrowband and Narrowband are typically only appropriate for low data rate communication systems, such as smart metering, and only offer up to 100 bps and 500 kbps, respectively [165]. In comparison, Broadband PLC systems operate at frequencies higher than 1 MHz and offer data rates upwards of 100 Mbps. In a large-scale smart battery comprising hundreds of networked instrumented smart cells, where each smart cell is transmitting and receiving sensor and configuration data, a higher data rate becomes a requirement for the system. If the data rate of the communication system is not sufficiently high, then the time taken for all of the smart cells to report their status to the battery management system (BMS) will increase. The smart cells must be able to report their status to the BMS such that a safety event, like cell overheating, can be managed before thermal runaway can occur. It is therefore appropriate to select a broadband category carrier frequency of at least 1 MHz in order to achieve a data rate high enough to facilitate such a large networked system of smart devices. This range of carrier frequencies is much higher than the frequencies used to perform characterisation of Li-ion cells with EIS.

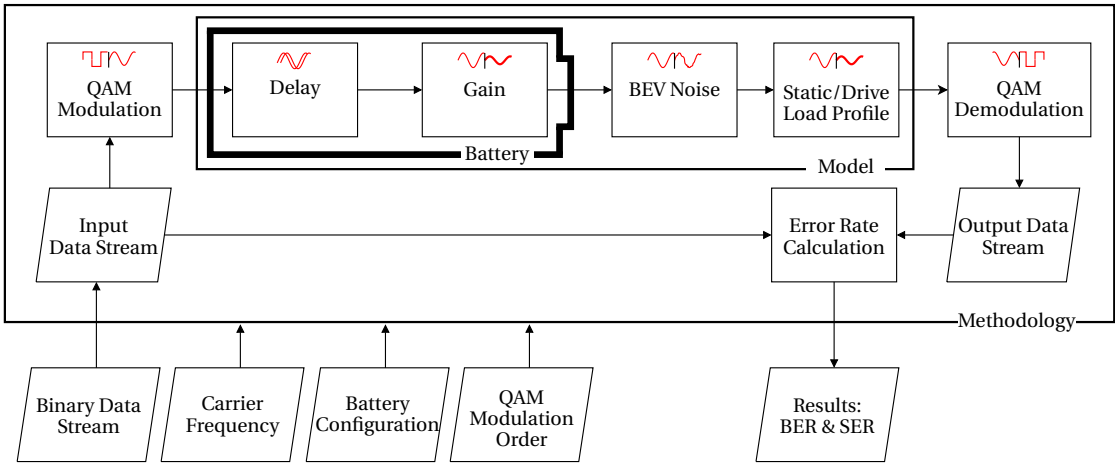

Figure 4.1: Process diagram of the experimental methodology.

This experimental work considers carrier frequencies between 100 kHz and 200 MHz to determine the best obtainable parameters possible for an in-situ Li-ion energy storage PLC system with respect to given symbol rates and noise rejection performance. Furthermore, QAM is used as a state-of-the-art modulation method for further increasing the data rate of the network by making efficient use of the communication channel.

Using EIS, impedance measurements of Li-ion cells are obtained. As stated in Chapter 3, electrical impedance possesses both a phase and a magnitude that can be obtained from reactance and resistance measurements, respectively. The reactance of a Li-ion cell affects the phase shift or delay of the signal transmitted through it. If the phase shift between current and voltage is positive, then the circuit shows inductive behaviour, whereas if it is negative, the circuit shows capacitive behaviour. The internal resistance of the cell forms a potential divider with the circuit it is connected to, and therefore affects the attenuation of the transmitted signal; as the internal resistance increases, the output voltage decreases. Hence, the potential difference of the electrochemical cell must be known before its internal resistance can be determined. The load of the circuit in this instance varies due to the use of the BEV through driving [166]. The attenuation of the transmitted signal may change at any time, and must thus be taken into account by the communication system.

Various methods exist for performing EIS at high frequencies in order to obtain

the impedance of a circuit or component. This includes using a potentiostat or galvanostat, whereby either the voltage or current is kept constant, respectively. This chapter uses real experimental data presented in [167], [168] to create a battery model in MATLAB for simulating a battery system to determine the impedance and phase for two 18650-model Li-ion cells in series, and two in parallel, for signals modulated at carrier frequencies between 100 kHz to 200 MHz. A pre-specified load in the form of a static or dynamic drive profile is applied to the battery model to obtain the signal attenuation on the simulated battery communication channel. The designed battery model is then used to simulate the effects of the Li-ion cells on the PLC signals transmitted in order to determine optimal parameters for the proposed PLC system. Since the EIS of a Li-ion battery changes with state of charge (SoC), the SoC is kept constant for the measurements used to create the battery model. Details on the experimental work on changes with the PLC performance with Li-ion battery SoC is presented in Chapter 5.

Using Equations (3.1) and (3.2), it is possible to obtain the internal resistance R of the Li-ion cell and the phase ϕ between the impedance Z and the internal resistance, from EIS measurements. By obtaining the internal resistance and impedance using these calculations based on this existing EIS data, the expected attenuation and phase shift applied to the signal transmitted through the Li-ion cell, are determined. In this study, it is first assumed that the load connected to the Li-ion cell is 1 Ω. A second simulation is then performed using load profile data obtained from real driving of a vehicle on a motorway near Coventry, U.K. [166]. These two simulations are used to determine the effects of the Li-ion cells and user driving on the communication system, respectively.

Thus far, only the effects of the Li-ion cells and the drive profile on PLC systems have been considered. It is also required to consider the effects of expected noise within the target communication medium. The maximum noise level expected within a BEV energy storage system must be applied to the transmitted signal to improve the accuracy of the system model. The most significant noise has been shown to be produced by the DC-DC converter within powertrain systems, which causes spikes of up to 2 MHz noise. An additional 12 MHz noise can be caused by the operation of the CAN signal bus [169].

Table 4.1: Parameters and their value ranges as used in the experimental method.

Parameter	Value
Battery Load	Constant 1 Ω or Dynamic Drive
QAM Modulation order	2, 4, 8, 16, 32, 64, 128, 256
Number of Symbols	10^7
Carrier Frequency	100 kHz – 200 MHz
Frequency step	100 kHz
Li-ion Cell Configuration	Two in parallel or two in series
Drive Profile Ambient Temperature	10 °C

A process diagram of the used methodology for the series of tests presented in this chapter are shown in Figure 4.1, and a summary of the experimental parameters and values described within this section are presented in Table 4.1. 10^7 QAM symbols of random data are modulated in orders of 2, 4, 8, 16, 32, 64, 128 and 256, as has been detailed in Section 3.3. Each QAM symbol is then processed by the simulated energy storage system model, by first applying the calculated delay and gain for the battery configuration under test. The QAM symbol is represented as a complex value of real and imaginary values, which are its in-phase (I) and quadrature (Q) components, respectively, as previously stated in Section 2.9, where equations that represent these facts are also presented. The delay and gain are applied by changing the phase shift of the QAM symbol, and by performing a multiplication of the I/Q components, respectively. Thereafter, the load of the system is taken into account, either as a constant 1 Ω load or taken from the dynamic drive profile. For the latter scenario, the actual transmission times of each of the 10^7 QAM symbols are used, and the simulated load is adjusted to the dynamic load at that specific time. Once the load is specified, the internal resistance of the simulated Li-ion battery is obtained from the battery model and is used in a voltage divider to calculate the attenuation of the signal transmitted through the simulated battery system. Finally, the noise that is expected within the target transmission medium is added.

After transmitting the QAM signal through the simulated energy storage system

model, the resultant signal is demodulated to obtain a binary data stream that is then compared to the original transmitted data. The bit error ratio (BER) is calculated by comparing each bit of the two data streams, and the symbol error ratio (SER) compares the symbols that the bits represent. Hence, SER is more sensitive to errors in data, and is always equal to or higher than BER. The BER and SER may be reduced through the use of signal conditioning techniques, and an analysis is given in Section 4.2 as to how such techniques may be utilised to improve the PLC performance.

4.2 Results and Discussions

This section presents the results obtained using the methodology described in Section 4.1, and evaluates the usability of the PLC systems under test. Furthermore, various parameters including carrier frequencies and battery configuration of a prospective PLC system for in-situ Li-ion energy storage systems are discussed.

4.2.1 Understanding the Effects of Noise with SNR

To understand the effects of noise on an in-situ battery communication system, a simulation is performed within MATLAB that varies the power of random noise on the communication channel. The steps used to perform this simulation are:

1. The data to be transmitted is modulated with the given QAM modulation order.
2. The effects of the Li-ion cell are applied to the QAM symbol stream. These effects are gain and phase shift, which are derived from the impedance of the cell model.
3. Noise is added to the QAM symbol stream to obtain the signal to noise ratios (SNRs) of interest.
4. The QAM symbol stream is demodulated and the simulated differences between the transmitted and the received data are compared to obtain the BER and SER.

In this work, the simulation is performed using SNRs of –27 dB, –18 dB, –9 dB, –6 dB, –3 dB, 0 dB, 3 dB, 6 dB, 9 dB, 12 dB and 15 dB in order to simulate the expected

communication error in times of low and high noise on the communication channel. The results of this simulation are presented in Figure 4.2, where it is shown that the decrease in SNR correlates with an increase in BER. The SER illustrates similar results, therefore they are omitted without loss of generality.

These results demonstrate that the increase in noise has a significant effect on the performance of the communication channel. However, this simulation performed in MATLAB does not perform synchronisation to allow for phase shift compensation and the application of gain to reduce the impact noise on the communication channel. In the following chapters, the in-situ battery communication system will use training symbols in order to perform these signal enhancement techniques. These results also indicate that with a sufficiently high SNR, such synchronisation is not required in order to achieve the best BER.

4.2.2 Performance of In-Situ Battery Communication System under Constant Load

This research utilises existing battery experimental data to understand how changes in resistance and reactance may affect an in-situ battery communication system using simulation. This simulation can then be used to determine the performance and implementation requirements, such as signal filtering, and battery configuration limitations. However, it is not an objective of this research to determine the causes of these differences in resistance and reactance with battery configuration.

The existing battery experimental data are presented in the Nyquist plots shown in Figure 4.3 of two Li-ion cells in series and parallel, which are used to determine the phase angle and the internal resistance of the cells required for the simulation of PLC data through the cells models. The difference in resistance R and reactance X between both configurations shown can clearly be observed, whereby the parallel configuration shown in Figure 4.3a shows much greater inductive reactance X_L, capacitive reactance X_C, and resistance in comparison to the series configuration illustrated in Figure 4.3b. Moreover, it can be seen that a large change in both the resistance and reactance occurs across the small frequency range of 90 MHz to 130 MHz for cells tested in parallel configuration. In fact, the resistance R reaches a peak of 374 Ω near 110 MHz, and the reactance X varies between 196 X_L and 155 X_C. In contrast, cells in series

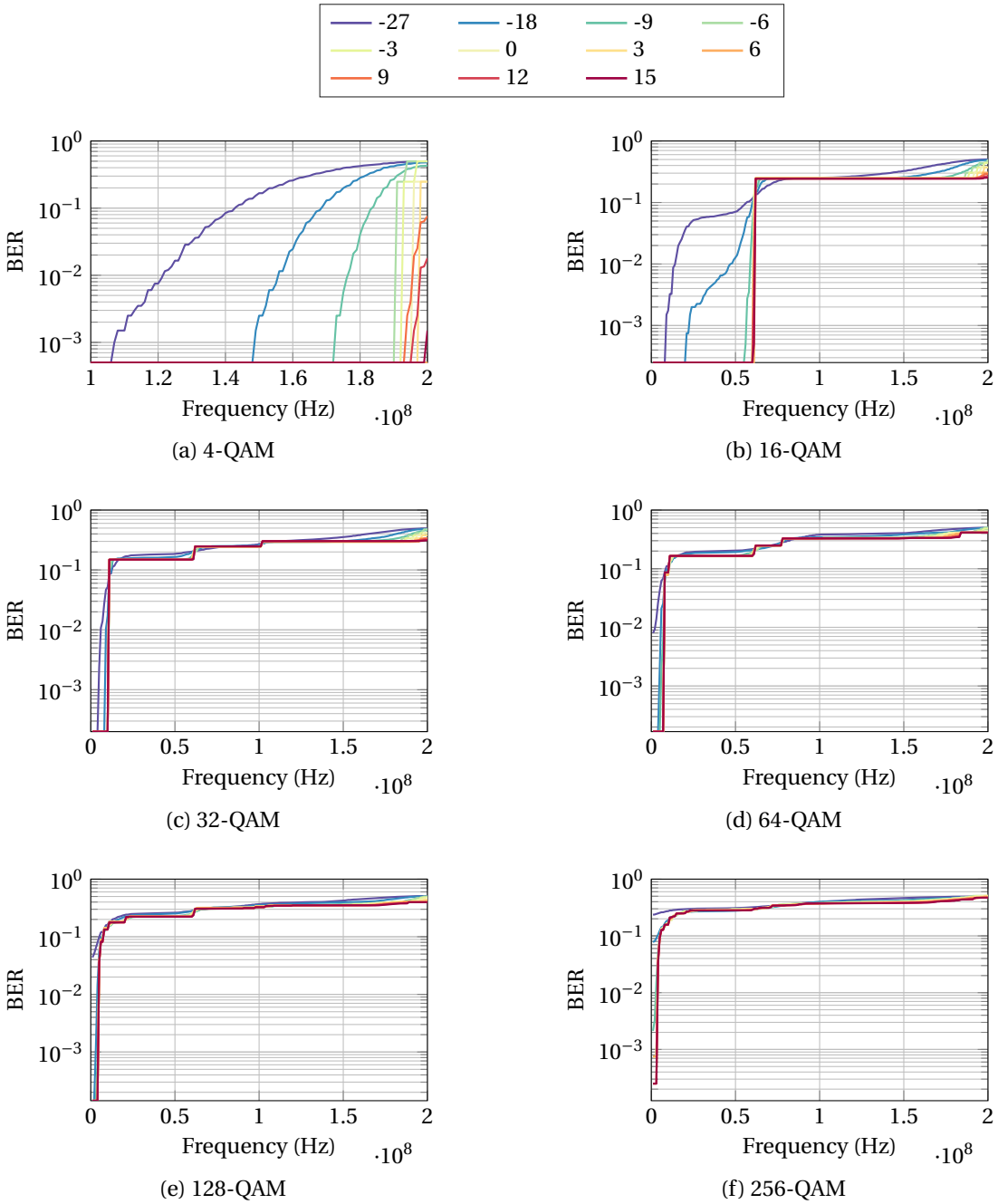

(a) 4-QAM

(b) 16-QAM

(c) 32-QAM

(d) 64-QAM

(e) 128-QAM

(f) 256-QAM

Figure 4.2: BER for QAM-signals transmitted through a simulated Li-ion battery with SNRs of −27 dB, −18 dB, −9 dB, −6 dB, −3 dB, 0 dB, 3 dB, 6 dB, 9 dB, 12 dB and 15 dB applied. Each order of QAM has a different minimum BER since the number of transmitted symbols is kept constant, rather than the number of transmitted bits.

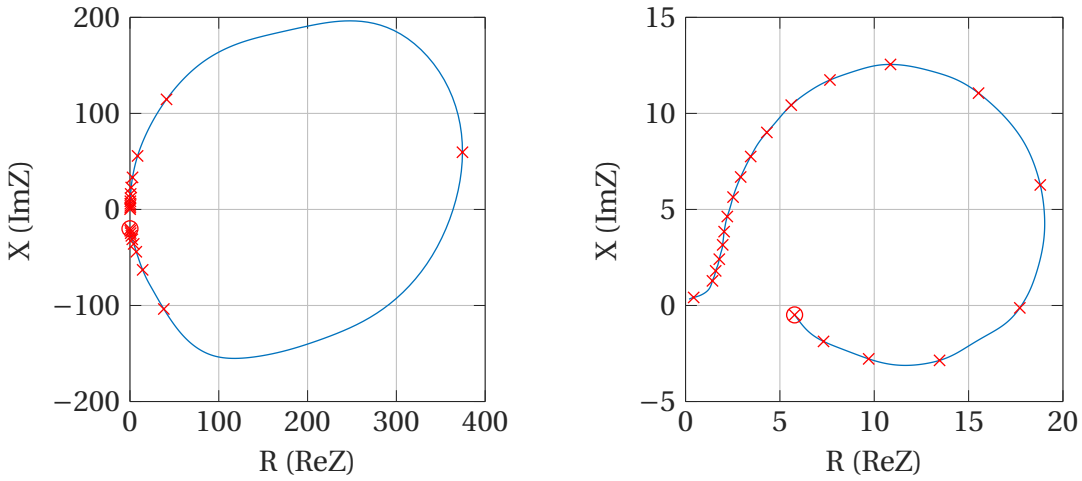

(a) Two Li-ion cells in parallel.

(b) Two Li-ion cells in series.

Figure 4.3: Nyquist plots of two Li-ion cells in parallel and in series. Circle and cross markers indicate steps of 200 MHz and 10 MHz, respectively.

configuration exhibit a gradual change in resistance and reactance for all carrier frequencies tested, reaching a peak resistance of 19 Ω near 150 MHz, and reactances of up to 12.5 X_L and 3.1 X_C.

As explained in Section 3.1, the reactance X and impedance Z can be used to derive the phase angle using Equation (3.1). In addition, the attenuation of the communication channel can be calculated by using the internal cell resistance R and the system load in a voltage divider. Using these facts, Figure 4.4 presents the magnitude of the phase change and attenuation of PLC signals transmitted through Li-ion cells based on the existing battery EIS experimental data presented in Figure 4.3. It is shown that both the attenuation on the communication channel and the phase angle change significantly with carrier frequency. A direct comparison of Figures 4.4a and 4.4b indicates that two Li-ion cells in series have a more negative impact in terms of attenuation across the spectrum of carrier frequencies tested. For the parallel configuration as shown in Figure 4.4a, the two Li-ion cells display the largest attenuation with a near-zero gain at a carrier frequency of 110 MHz, before recovering towards a gain of 1 at 200 MHz. On the other hand, for the series configuration as shown in Figure 4.4b, the gain falls slowly to 0.05 at 153 MHz, and then only rises slowly towards a gain of 0.15 at

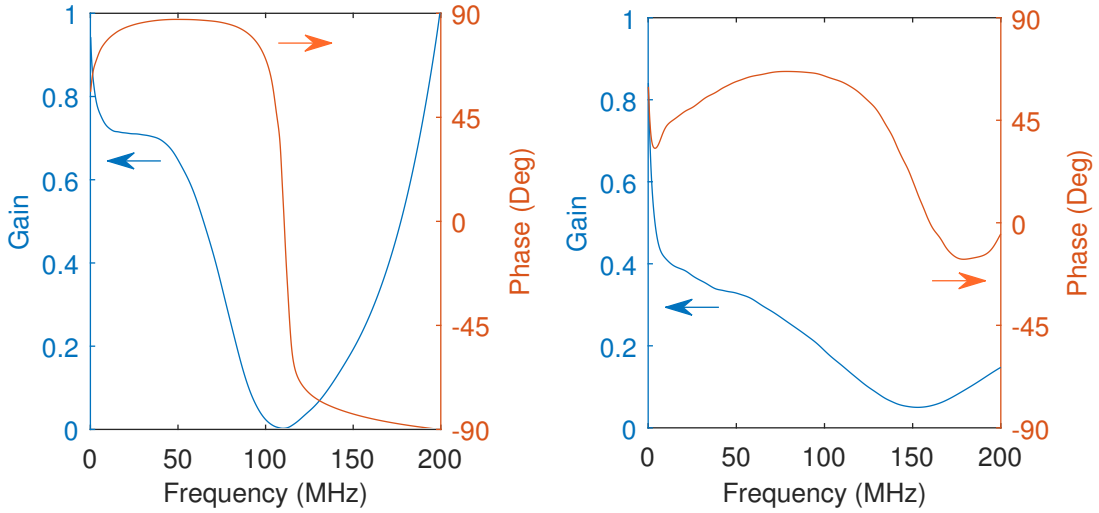

(a) Two Li-ion cells in parallel.

(b) Two Li-ion cells in series.

Figure 4.4: The carrier frequency dependence of the phase and gain of PLC signals transmitted through two Li-ion cells in parallel and in series.

200 MHz. Whereas a parallel cell arrangement results in a stable gain of 0.7 between 13 MHz and 40 MHz, for a series configuration it is shown that the lower the carrier frequency, the less attenuation is observed on the signal. The differences in both gain and phase between series and parallel configuration may be due to multipath effects, which, as explained in Section 2.7, may cause attenuation due to the signal arriving at the receiver at different times. Notwithstanding, the frequency range of 13 MHz to 40 MHz demonstrates the least change in amplitude fading between both parallel and series configurations, and would therefore be considered the best range of coherence bandwidth, which is the range of frequencies within which the attenuation on the communication channel remains relatively unchanged. However, as it will be mentioned later in this section, the change in phase shift in the series configuration within this range may require QAM synchronisation to avoid communication error. These observations signify that both the battery configuration and the carrier frequency can significantly impact the performance of an in-situ battery PLC system. In the following, the significance of these characteristics are examined a simulation of an in-situ battery PLC system using this battery characteristic data.

The phase shift of the signal transmitted through two Li-ion cells in parallel, as

shown in Figure 4.4a, is significant throughout the carrier frequencies tested, nearing both –90° and 90° for most of the carrier frequencies tested. However, at 110 MHz, the phase delay crosses 0° as it quickly deviates from 90° to –90°. The effect of this momentary lack of delay at 110 MHz is shown in the following analysis, whereby an improvement in error rates is seen for all QAM symbol rates. Nevertheless, the attenuation at 110 MHz is too large for this carrier frequency to be useful, unless significant signal conditioning is added for every two Li-ion cells in parallel to compensate for the signal loss. It is possible that even small changes in characteristics of the Li-ion cell could significantly alter the phase shift of the transmitted signal, due to the sharp change in phase with frequency. As mentioned in Section 2.10, existing QAM systems that use pilot symbols for synchronisation may provide adequate compensation for the phase shift of the communication channel. Despite this fact, the sudden change in phase shift at 110 MHz means that the available bandwidth for the communication channel is reduced, as even slight changes in carrier frequency will cause great changes in phase which may negatively influence a QAM systems' ability to demodulate data correctly.

In contrast to the parallel configuration, the phase shift of two cells in series, as shown in Figure 4.4b, does not fluctuate as significantly, reaching a maximum of 66°, before a trough that falls to a minimum of –16°. If both parallel and series configurations are then taken into account, the performance of the PLC system is expected to be optimal at 30 MHz, where both the attenuation and the phase remain most steady. At this frequency, the communication system is thus less susceptible to clock jitter noise, and may therefore use wider communication channels.

Figures 4.5a and 4.5b show the BER and SER of data streams transmitted with PLC using various QAM orders through a model representing two Li-ion cells in series, respectively. It can be observed that both BER and SER are either low at 10^{-7}, or tend to 1 due to the majority of data transmitted becoming corrupt. By comparing both figures, it can be shown that 2-QAM is not affected by the characteristics of the Li-ion cells throughout the entire frequency spectrum tested. In comparison, of the other modulation orders, only 4-QAM signals are able to approach the minimum BER and SER of 10^{-7} at frequencies of 1 MHz to 14 MHz, and 134 MHz to 200 MHz. Modulation orders higher than 4-QAM fail to demonstrate any reasonable data communication.

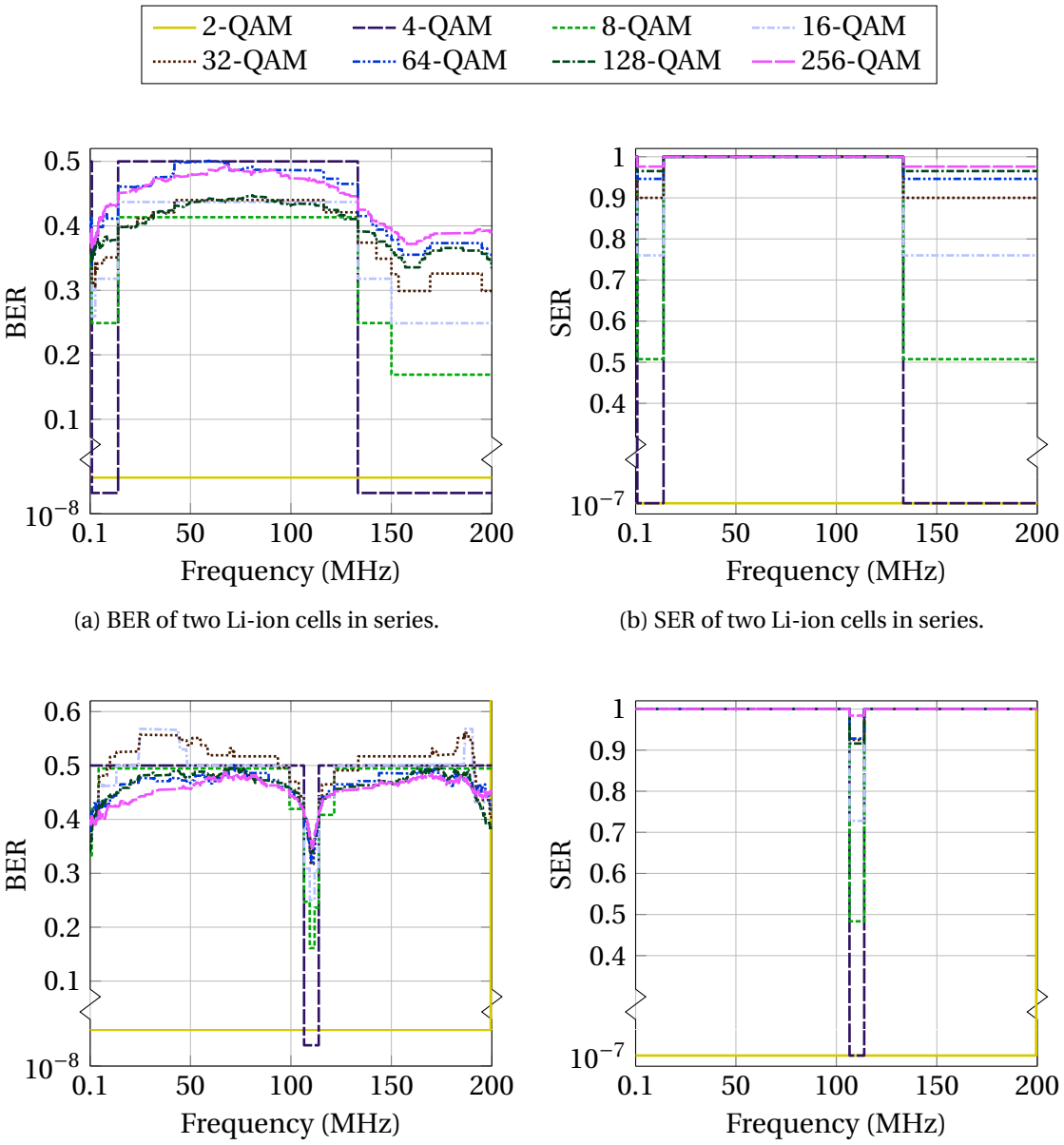

(a) BER of two Li-ion cells in series.

(b) SER of two Li-ion cells in series.

(c) BER of two Li-ion cells in parallel.

(d) SER of two Li-ion cells in parallel.

Figure 4.5: BER and SER of PLC through Li-ion cells under constant 1 Ω load.

Figures 4.5c and 4.5d display the BER and SER of data streams transmitted through the battery model representing two Li-ion cells in parallel, respectively. When the data are compared with the data transmission through two cells in series, these results show degraded performance. Moreover, the results indicate that 2-QAM is able to keep a BER and SER of 10^{-7} between 100 kHz and 199 MHz, but then immediately increases to a maximum SER of 1 at 200 MHz. Of the other higher order modulated data streams, only 4-QAM is able to demonstrate stability at any point across the tested frequencies. Between 106 MHz and 114 MHz, the data stream modulated with 4-QAM yields a BER and SER of 10^{-7}, deviating from a SER of 1 presented at all other carrier frequencies tested. In fact, at these frequencies, all other QAM orders show a decrease in both BER and SER. For instance, the BER and SER of 8-QAM at 110.6 MHz are reduced to 0.16 and 0.48, from the maximum of 0.49 and 1, respectively. This improvement in error rate is reduced with increasing QAM order. As already stated, this sudden improvement in BER and SER occurs within the same range of frequencies that produces a significant change in resistance and reactance within the Nyquist plot shown in Figure 4.3a.

From these results, it can be concluded that using QAM causes increasing error rates with increasing modulation order. Across the carrier frequencies tested, 2-QAM demonstrates the best possible BER and SER for both series and parallel arrangements of the two Li-ion cells modelled. For higher modulation orders of QAM, the window of usable carrier frequencies not only decreases, but also varies significantly between series and parallel cell arrangements, whereby the parallel arrangement poses a much smaller window of 106 MHz to 114 MHz in comparison to the two windows of 950 kHz to 14 MHz and 133 MHz to 200 MHz for the series arrangement.

Both the BER and SER for serial and parallel configurations displayed no difference between simulations that include expected noise on the target communication channel, such as from switch-mode converters [169], and simulations without noise consideration. By taking into account the intensity of attenuation and phase for specific carrier frequencies and configurations, these results may be used to predict the usability of PLC within a target environment when a noise characterisation for the specific energy storage system is also considered. Due to the wide variety of powertrain systems, it is expected that each will exhibit differing properties of electromagnetic

noise, and therefore noise should only be considered for each specific system. Furthermore, consideration must be given to the noise generated as a consequence of user behaviour, such as when acceleration or braking is applied, this action may produce spikes of noise large enough to disrupt the communication channel.

The effects of delay and attenuation that the Li-ion cell imposes on the in-situ transmitted signal increases with QAM order. As stated in Section 3.3, QAM is a summation of in-phase and quadrature components, and the effects of delay and attenuation of the Li-ion cells have a direct influence on these components and therefore the quality of data transmission. The most successful modulation order, 2-QAM, is also known as binary phase shift keying (BPSK) as the only two symbols in the constellation are two states of phase shift and hence do not need any amplitude modulation used in higher orders of QAM. In order to fully exploit the performance benefits of QAM for PLC in terms of achievable data rates, at least 4-QAM must be used.

Through focusing on the resultant QAM constellation plots for each modulation order, it can be observed as to why the error rates are so polarised. For example, Figure 4.6 visualises that despite both 2-QAM and 4-QAM demonstrating very low error rates, the attenuation is so significant that it is difficult to observe the different constellation points in each plot without significantly reducing axes limits. If such a system is to scale to many Li-ion cells in parallel, then the use of 110 MHz as a carrier frequency will be unacceptable due to the level of signal amplification required throughout the transmission medium. Therefore, in this case, the smallest amount of noise could cause data corruption. In fact, a carrier frequency of 110 MHz is shown to produce most appropriate results for two Li-ion cells in parallel only because the phase shift is 9°, which is sufficiently low for the QAM symbols to remain within their constellation sector. This response can be observed in Figure 4.6, whereby the attenuation is so significant that the points approach the origin, however they are still decoded correctly as the constellation points are within their correct sector. However, as the QAM order is increased, symbols that are not mapped to the sectors closest to the origin become invalid due to the significant attenuation that displaces these symbols out of their correct sector. This behaviour can be seen for 8-QAM and 16-QAM, whereby the outer 4 and 12 constellation points are not mapped to their correct

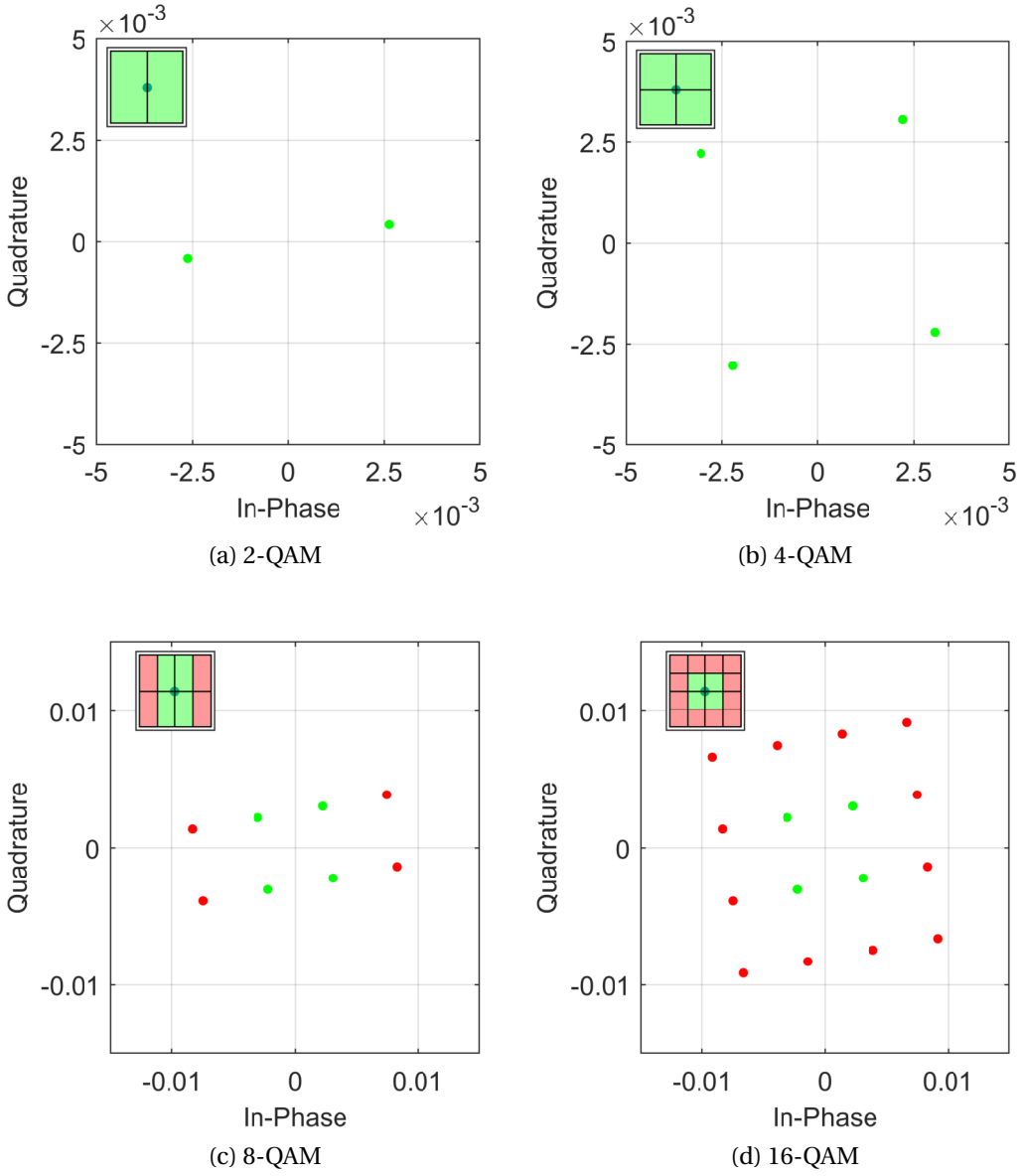

(a) 2-QAM

(b) 4-QAM

(c) 8-QAM

(d) 16-QAM

Figure 4.6: QAM constellations of PLC data transferred through two Li-ion cells in parallel at carrier frequencies of 110 MHz. Insets show green and red shaded segments that denote constellation points within their correct and incorrect sectors, respectively.

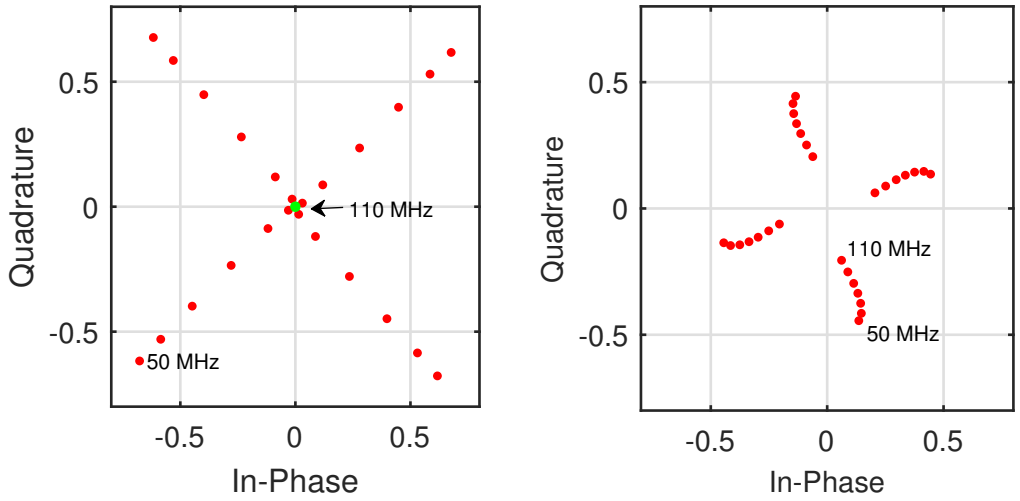

(a) Two Li-ion cells in parallel.

(b) Two Li-ion cells in series.

Figure 4.7: Frequency sweep of 50 MHz to 110 MHz in 10 MHz steps of a 4-QAM signal. The closer the symbol tends to the origin, the more significant the signal attenuation. Green and red markers denote constellation points within their correct and incorrect sectors, respectively.

sector, respectively. In other words, with increasing QAM order the system is more prone to attenuation.

Figure 4.7 illustrates that the magnitude of the 4-QAM signal decreases as the carrier frequency increases from 50 MHz towards 110 MHz. The rate with which the magnitude decreases is greater than when the two Li-ion cells are connected in parallel. In fact, Figure 4.7a shows that there is a decrease in magnitude of 0.68 between 50 MHz and 110 MHz for a parallel configuration, whereas Figure 4.7b shows only a decrease in magnitude of 0.25 for a series configuration. However, Figure 4.7a shows that whilst the magnitude may be the lowest at 3.8×10^{-3} when using a carrier frequency of 110 MHz, the change in phase pushes the constellation points (shown in green) into their correct sectors. This change in phase may also be seen in Figure 4.4a whereby the constellation points rapidly decreases towards 0° at 110 MHz. This behaviour corresponds to the improvement in SER that is also observed within Figure 4.5d. Nevertheless, as already discussed, the high attenuation at 110 MHz means that an increase in the magnitude of noise on the communication channel has the potential

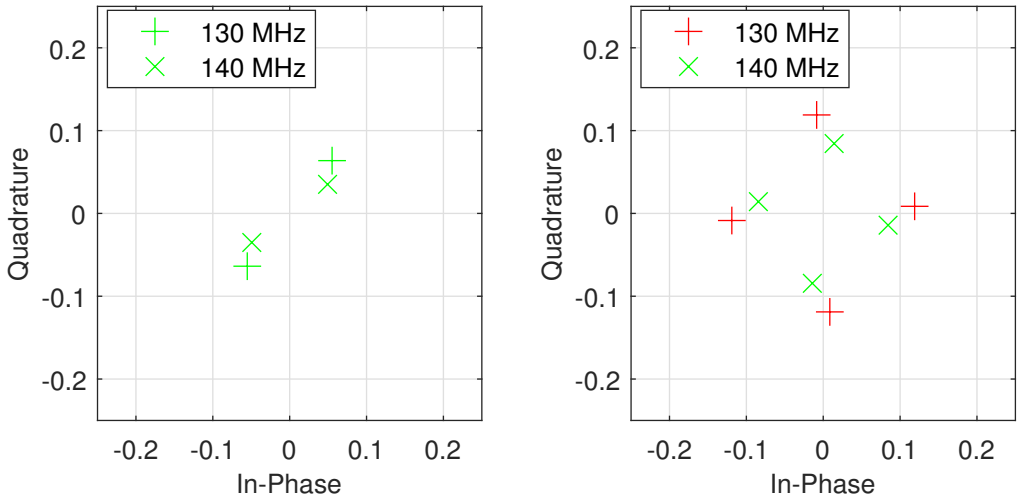

(a) 2-QAM (b) 4-QAM

Figure 4.8: QAM constellations of PLC data transfer through two Li-ion cells in series at carrier frequencies of 130 MHz and 140 MHz. Green and red markers denote constellation points within their correct and incorrect sectors, respectively.

to reduce the reliability of the PLC system.

On the other hand, Figure 4.7b shows that there is only a gradual change in phase and attenuation between 50 MHz and 110 MHz. In fact, over the full range of carrier frequencies tested, the arrangement of two Li-ion cells in series showed only gradual changes in reactance and internal resistance, in comparison to the sharp changes in parallel configuration. This gradual change in phase is not sufficiently significant enough to push any of the constellation points into their correct sectors at 110 MHz, but rather does so from 133 MHz upwards. However, the attenuation identified in the series configuration does not increase as significantly as seen in the parallel configuration for the same range of carrier frequencies. This performance indicates that less signal conditioning is required for Li-ion cells arranged in series than for cells arranged in parallel. However, phase shift compensation will still be required for both arrangements in order to place QAM symbols within their correct sector.

It is shown in Figure 4.8 that an improvement in SER can also be seen for PLC transmission through two Li-ion cells in a series configuration when the carrier frequency is increased from 130 MHz to 140 MHz. This improvement is reflected in the

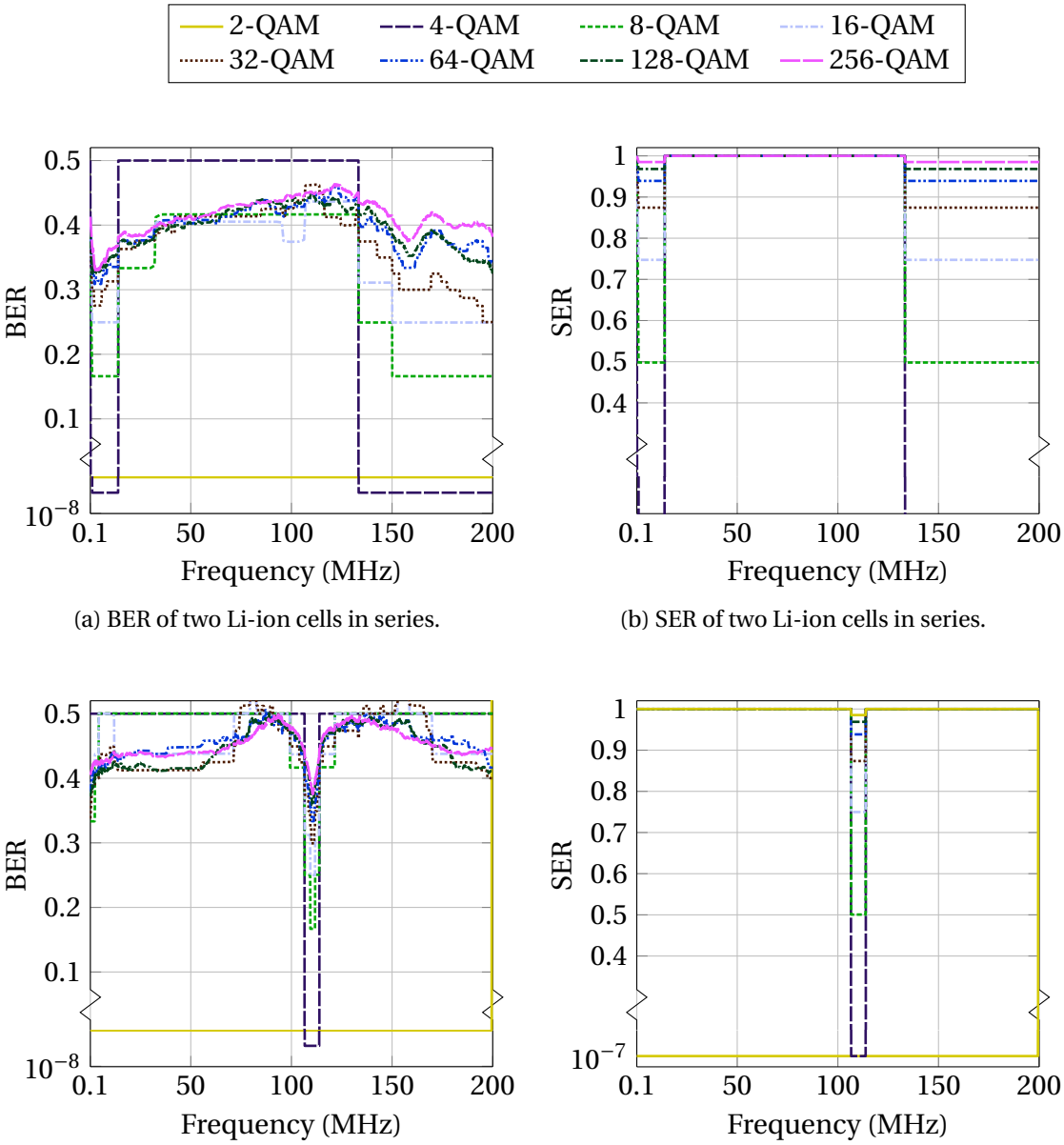

(a) BER of two Li-ion cells in series.

(b) SER of two Li-ion cells in series.

(c) BER of two Li-ion cells in parallel.

(d) SER of two Li-ion cells in parallel.

Figure 4.9: BER and SER of PLC through two Li-ion cells in series or parallel under the dynamic drive profile load.

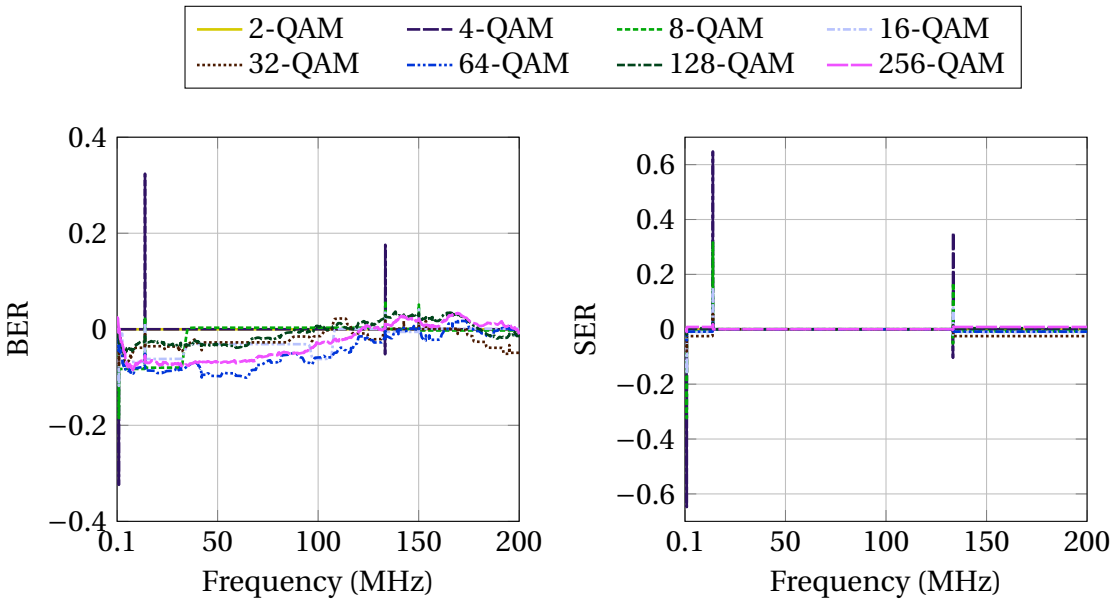

(a) Difference in BER for two Li-ion cells in series.

(b) Difference in SER for two Li-ion cells in series.

(c) Difference in BER for two Li-ion cells in parallel.

(d) Difference in SER for two Li-ion cells in parallel.

Figure 4.10: Differences in BER and SER between a constant 1 Ω load and the dynamic drive profile load.

reduction in SER for 4-QAM at 140 MHz, as displayed in Figure 4.5b. In this case, the phase shift is too small to cause errors within the data stream as shown by the green points. Despite this, the transmitted QAM symbols are displaced to near the origin, highlighting that the attenuation is so substantial that significant signal conditioning is required in order to achieve a SNR that allows for adequate data transmission rates.

Depending on the carrier frequency selected for the PLC system and the magnitude of the noise on the target transmission channel, signal conditioning techniques may be required. These techniques may consist of automatic gain control (AGC), phase compensation, and band-pass filters. However, signal conditioning techniques may be limited by the available space within a BEV battery, and by the reluctance to reduce the energy density of the battery, especially if a significant number of in-situ signal conditioning systems is required. Moreover, these signal conditioning techniques may vary between different energy storage systems due to their unique design, electrochemical chemistry, transmission channel characteristics and cell arrangement.

These results show that the phase shift caused by the Li-ion cell on the transmitted PLC signal varies with frequency. These changes in phase shift are generally of significance to cause QAM symbols to be displaced from their correct sector, resulting in polarised changes in the achieved BER and SER. Phase shift correction must therefore be utilised to reverse the Li-ion cells' effects of such delay on the signals. Hence, phase shift correction is utilised in the experimentation presented in Chapters 5 and 6. Should simultaneous data transfer through the use of frequency division multiple access (FDMA) be required, the significant change in phase shift at 110 MHz will severely compromise the integrity of the in-phase and quadrature components of QAM, making them misaligned with the reference QAM symbol mapping, and consequently increase the SER in the communication system. A carrier frequency of 30 MHz is therefore recommended for use within a PLC system utilised within a large BEV Li-ion battery using QAM, on the precondition that phase shift compensation is employed. The required amount of signal conditioning is dependant upon the number of cells arranged in parallel and series within the battery.

4.2.3 Performance of In-Situ Battery Communication System under Dynamic Load

Real battery load profile data shown in Figure 4.11 has been obtained from a vehicle driving on a motorway near Coventry, United Kingdom [166], is used to determine the effects of dynamic load on the performance of the prospective PLC systems considered. This drive load profile was recorded at an ambient temperature of 10 °C for a drive duration of 44 minutes. Due to the high carrier frequencies of the communication system under consideration, all of the 10^7 symbols are transmitted within 100 seconds and only 50 milliseconds for carrier frequencies of 100 kHz and 200 MHz, respectively. It is therefore expected that the drive load profile will have less influence on error rates for communication systems utilising higher carrier frequencies due to the reduced period of time that the drive profile is considered. Before the effects of the drive load profile, which is based on a single 5 Ah Li-ion cell, are applied to the simulated communication system, the drive profile is normalised for two 3 Ah 18650-model Li-ion cells using

$$\text{Normalised Load} = \frac{\text{Drive Load Profile}}{I_\alpha} \times I_\beta \times n \tag{4.1}$$

where $I_\alpha = 5$, $I_\beta = 3$ and $n = 2$.

Figure 4.9 shows the BER and SER of a PLC system transmitted through two Li-ion in series and in parallel when the drive load profile is considered. In comparison with the results that use a constant load of 1 Ω, the difference in results is not immediately apparent. Therefore, the numerical difference in error rates between the constant 1 Ω load and the dynamic drive profile load is shown in Figure 4.10, whereby it can be seen that only certain carrier frequencies provide substantial improvements in BER of up to 0.15, but only little improvement in SER of up to 0.05 is observed.

This study shows that noticeable improvements in both BER and SER are observed for cells in series arrangement. The greatest improvement in BER is occurred for 64-QAM, but this does not correlate with the same degree of improvement in SER due to some incorrect bits still existing within the received symbols. A greater improvement in BER can be seen for cells in parallel between 10 MHz to 80 MHz and 160 MHz to 190 MHz, but only for modulation orders of 16-QAM and higher. This improvement in BER does not translate to any change in SER within the same frequency ranges.

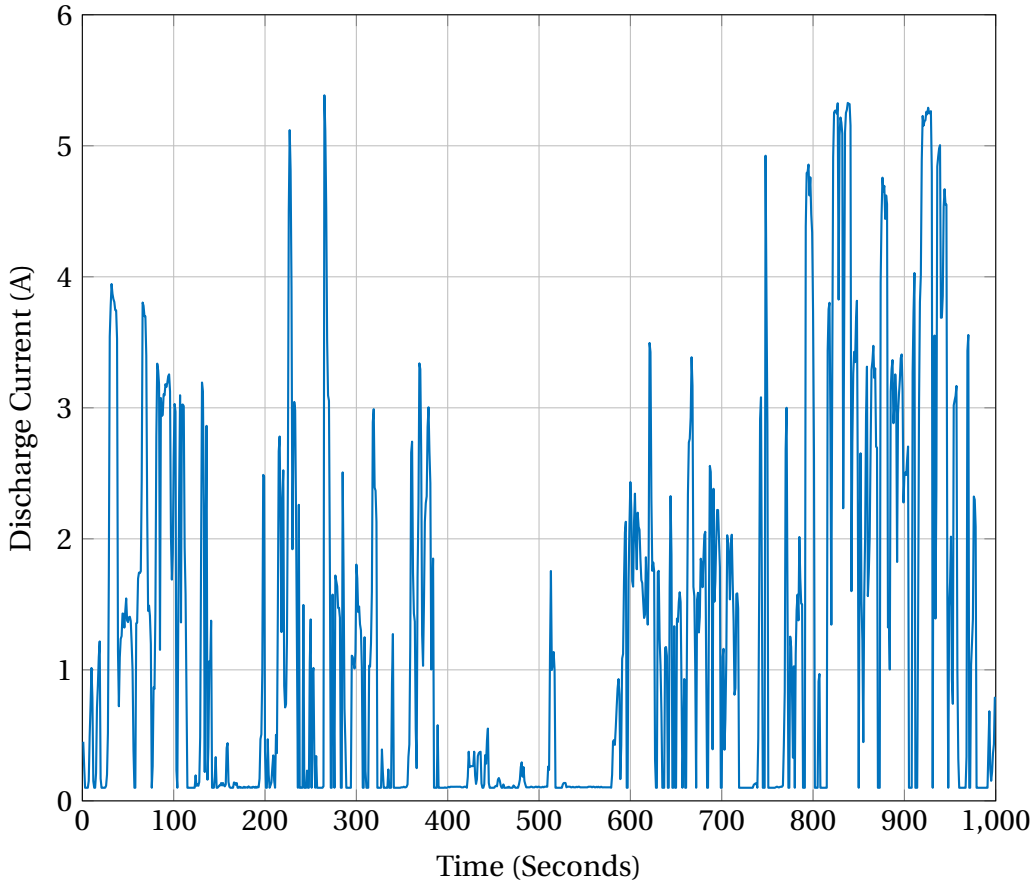

Figure 4.11: Drive profile sampled from a single 5 A h Li-ion cell during driving on a motorway near Coventry, United Kingdom [166].

This behaviour is due to multiple bits being decoded incorrectly for some symbols when transmitted under the constant load model, but not under the dynamic drive load profile due to a favourable reduction in attenuation. Although this improves BER, there is no change in SER if there is still one bit set incorrectly within the transmitted symbols. In contrast, a reduction in BER of up to 0.04 for cells in parallel is shown between 90 MHz to 140 MHz, which indicates that a small number of additional bits are changed during transmission at these frequencies, in the opposite effect of that described for the improvements to the BER seen in Figure 4.10c.

The use of the drive load profile additionally simulates the effects on PLC of a sudden change in drive load, such as through acceleration. These simulations

demonstrates that it is exceptionally rare that corruption of data occurs due to sudden changes in drive load. This is because the carrier frequencies tested are orders of magnitude higher than the change in load seen within the drive load profile.

Based upon these comparisons, one can conclude that the most suitable carrier frequency is 30 MHz as previously stated, even when the drive load profile is also considered. Firstly, it can be implied that this carrier frequency offers stable attenuation and phase shift behaviour from the simulated Li-ion cell configurations. Secondly, the drive load profile is responsible for only marginal change in error rates at this carrier frequency. This is likely due to the rate of change of the battery load being orders of magnitude lower than that of the carrier frequency.

4.3 Conclusions

In this chapter, the existing impedance data of both a series and parallel configuration of two in-situ connected 18650-model cylindrical Li-ion cells were utilised to create a battery model for the novel purpose of simulating the effects of Li-ion cells on a PLC system that utilises QAM.

Without any synchronisation, analogue filtering or digital error correction, the modelled transmission medium of the two Li-ion cells has been shown to be mostly inadequate for PLC with carrier frequencies between 100 kHz to 200 MHz. This behaviour is due to the significant attenuation of the signal transmitted through the cells when a nominal constant load of 1 Ω is connected or when real drive profile data is utilised. Furthermore, it has been shown that a parallel arrangement of Li-ion cells results in the highest BER and SER due to the increased magnitude of both attenuation and phase shift in comparison to a series arrangement of cells.

Changes in signal attenuation and phase will reduce the range of frequencies in a coherence bandwidth. Such changes may be due to the effects of multipath characteristics caused by impedance mismatching, which, as explained in Sections 1.1 and 2.7, is caused by the propagation of signals through multiple paths causing it to arrive at the receiver at different time intervals. These multipath characteristics change with frequency, and as Chapter 6 will show, the multipath characteristics are heavily influenced by the number of cells in a battery and the configuration of the

cells in parallel and series. In this chapter, the differences in attenuation and phase shift between the series and parallel configurations simulated in this chapter can already be observed. Despite this fact, the focus of this chapter is the demonstration of using existing EIS battery and BEV drive cycle data to perform a simulation of a novel in-situ battery PLC system during a driving scenario, in order to determine the most appropriate communication channel parameters, such as carrier frequency and signal conditioning. In-depth analysis on the effects of battery configuration on multipath fading is presented in Chapter 6.

In terms of coherence bandwidth, it has been shown that the range of frequencies of 13 MHz to 40 MHz showed the least change in attenuation and phase shift for both series and parallel configurations simulation in this experiment. In fact, it can also be concluded that when a carrier frequency of 30 MHz is used, both the attenuation and phase are least frequency dependent, allowing for wider communication channels and increased tolerance for clock jitter. This system requires at least a phase compensation component to counteract the significant (but steady) phase shift observed at that frequency. Moreover, this chapter has shown that significant signal amplification will be required for QAM PLC through large BEV battery packs across all evaluated carrier frequencies. A closed-loop amplifier, such as automatic gain control, may be utilised to overcome the observed signal attenuation. Further research is required to ensure that this process does not modify the in-phase and quadrature components of QAM.

By simulating two batteries of different configurations, the effects of connecting cells in series and parallel can be compared. However, the addition of further cells to this battery model requires new measurements of impedance using EIS due to the non-linear behaviour of cells which may be caused by the connections between the terminals of the cells and the measurement equipment. Therefore, Chapter 6 discusses and measures the differences in S21 magnitude and PLC performance for four distinct battery configurations, where it is shown that the differences between these battery configurations are non-linear.

This chapter has also shown that existing Li-ion battery characteristic data based upon EIS experimentation and drive profile data may be used to perform simulations of an in-situ battery PLC system with QAM within a BEV environment. In the following chapters, battery characterisation is performed for the specific purpose of commu-

nication channel analysis using scattering parameters. Additionally, real PLC with QAM data communication is conducted to determine the changes in communication system performance, such as error rates, with SoC (in Chapter 5) and battery configuration (in Chapter 6).

Chapter 5

Impact of Lithium-ion Battery State of Charge on In-Situ Power Line Communication

In Chapter 4, an in-situ lithium-ion (Li-ion) battery power line communication (PLC) system was simulated to measure the performance of such a communication system within a simulated battery electric vehicle (BEV) load and noise environment. The next stage of this research is to determine the performance of this communication system with changes in Li-ion cell characteristics.

In this Chapter, the effects of Li-ion cell state of charge (SoC) on an in-situ PLC system are evaluated for carrier frequencies of 10 MHz to 6 GHz. Instead of using existing electrochemical impedance spectroscopy (EIS) measurements of Li-ion cells as conducted in Chapter 4, scattering parameter (S-parameter) S21 measurements and analysis are performed on a single 18650-model Li-ion cell using a vector network analyser (VNA) to determine insertion loss of the communication channel and cell impedance with carrier frequency. A bespoke cell holder for series-through configuration is designed and calibrated to reduce the effects of noise, and is utilised within this study to facilitate the characterisation of an 18650-model Li-ion cell. A vector signal transceiver (VST) is used to perform actual tests of in-situ Li-ion PLC using quadrature amplitude modulation (QAM). Both tests with the VNA and VST are carried out when the Li-ion cell is discharged to 95 %, 80 %, 60 %, 40 %, 20 % and 5 % SoC to

determine the changes in communication performance as the cell is being discharged, such as through driving a BEV. The performance of this PLC system is quantified by quality of signal parameters obtained using the PLC, which are error vector magnitude (EVM), bit error ratio (BER), and symbol error ratio (SER). Furthermore, QAM is used to demonstrate the efficient use of the communication channel to achieve higher data rates. Comparisons are made between the changes of the PLC performance and the S21 forward transmission coefficient of this channel with the different SoCs tested. Using these comparisons, a prediction of the expected data rate attainable is enabled using the S21 magnitude when cell SoC is taken into account. The analysis of the changes in S21 magnitude and PLC performance through a Li-ion cell with various SoCs, up to high carrier frequencies of 6 GHz, is a main contribution to the research community.

The overall results indicate that certain carrier frequencies and QAM orders may not be suitable for the in-situ battery PLC due to changes in battery impedance with certain Li-ion cell SoC, which cause an increase in EVM, BER, and SER. This research shows that cell characterisation at a specific SoC only is inadequate to determine the expected performance of an in-situ Li-ion cell PLC system. Recommendations and trends on the impact of these changing characteristics based upon empirical results are also presented in this chapter.

5.1 Experimental Details

In this experimental work, a VNA and VST are used to perform S21 measurements of the Li-ion as a PLC channel, and to determine the effectiveness of a Li-ion cell as a PLC channel using QAM. These measurements are analysed and compared to determine the S21 magnitude thresholds with which symbol errors begin to occur in the communication system, and how these thresholds change with Li-ion SoC.

The details on the use of the VNA and VST have been presented in Sections 3.2 and 3.3, respectively. In this chapter, the VNA is configured to perform a sweep of S21 measurements over the frequency range from 10 MHz to 6 GHz with a step of 1 MHz. To improve the accuracy and confidence of the results obtained, this sweep is performed 100 times. The S21 data is then processed to determine the median for

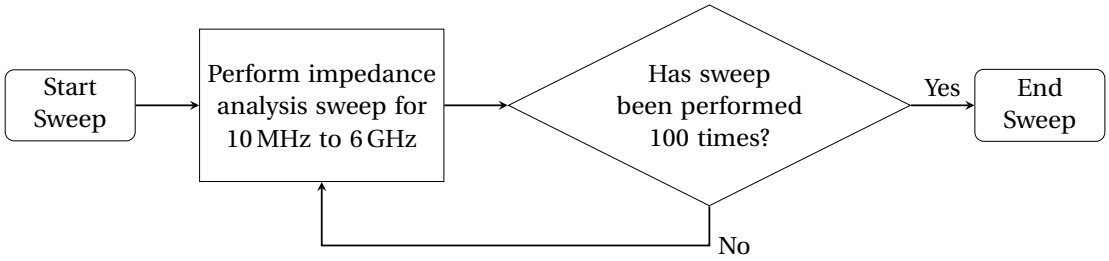

Figure 5.1: Flowchart of the specific experimental process for the VNA.

each frequency tested. The series of 100 sweeps are performed for each SoC tested, as shown in the experimental process overview on the use of the VNA in Figure 5.1. The technical process of acquiring measurements with the VNA is shown in Figure 3.4, which includes the use of the R&S ZN-Z129 calibration kit for performing 'One-Path Two-Port' calibration with the series-through cell holder. The details and design of the series-through cell holder are presented in Section 3.4.1 and Appendix A.1, respectively. Since the ZN-Z129 calibration kit has a shorter signal path than the cell holder and the Li-ion cell, the measured phase shift will include a linear background value, which will be compensated for during data processing to obtain only the characteristics of Li-ion cell on the phase of the signal. The process of removing the phase shift background is presented in Section 3.2.

The VNA is connected to the cell holder such that the stimulus signal is output to the negative terminal of the Li-ion cell, as is stated in Section 3.4.1. Also, the VNA is connected to the cell holder using a coaxial cable with 2.92 mm SubMiniature version A (SMA) connectors rated for frequencies up to 40 GHz. However, despite the 40 GHz rating of the VNA and the cable, this experiment will limit the highest frequency tested to 6 GHz, as this is the maximum frequency that can be tested using the VST, as explained in Section 5.1.1. This part of the experiment results in a series of plots that show alterations in Li-ion cell characteristics with frequency and SoC.

During this experiment, the S-parameters of the Li-ion cell are the only varying properties with changing SoC. In which case, the impedance characteristics of the experimental components, such as the cell holder, will not change. Therefore, using a baseline measurement of the Li-ion cell S-parameters eliminates the characteristic transmission coefficient of these experimental components, thereby only presenting

the change in S21 caused only by changes to the Li-ion cell SoC. Hence, a baseline of 95 % SoC is selected as it is the first measurement performed within this experiment. These results are used to identify changes in the transmission coefficient of the cell with SoC at various carrier frequencies. In this regard, measuring the absolute transmission coefficient of the Li-ion cell may not clearly demonstrate changes with SoC, but are also presented to allow for analysis of the Li-ion cell in terms of its channel characteristics. These results also include an S21 magnitude plot displaying the attenuation of the stimulus signal through the cell holder, and a plot displaying changes in phase shift, relative to their respective baselines at 95 % SoC, in addition to figures showing the measured S21 magnitude and phase.

5.1.1 Communication Error Analysis

To determine the effectiveness of a Li-ion cell as a PLC channel using QAM, a VST is used. In this study, a NI PXIe-5840 VST and PXIe-8880 controller within a PXIe-1092 chassis, as shown in Figure 3.5, are used to transmit and to receive QAM symbols at carrier frequencies of 10 MHz to 6 GHz with a step of 50 MHz. In comparison to the S21 measurements, this increased frequency step is selected to complete the experiment within a reasonable period of time.

As previously explained, the VST is configured to transmit 100,000 known QAM data symbols with a symbol rate of 100 kHz, and to receive the signal after it has passed through the Li-ion cell. As explained in Section 2.9, pilot symbols are included within this data stream to allow the VST to perform synchronisation through the use of normalisation and phase compensation required for effective symbol trace demodulation. Such synchronisation is necessary to ensure correct demodulation of QAM data, and is commonly used in existing QAM transceivers. The series-through cell holder is connected to the VST using coaxial SMA cables rated to 12.4 GHz at a defined torque. The cell holder is configured such that the negative terminal of the Li-ion cell is connected to the RF output of the VST, and the positive terminal is connected to the RF input.

The experimentation with the VST is used to obtain measurements of BER, SER, and EVM with changing SoC. By using such measurements, an analysis of how they change as the SoC of the cell decreases can be performed. Note that the methods for

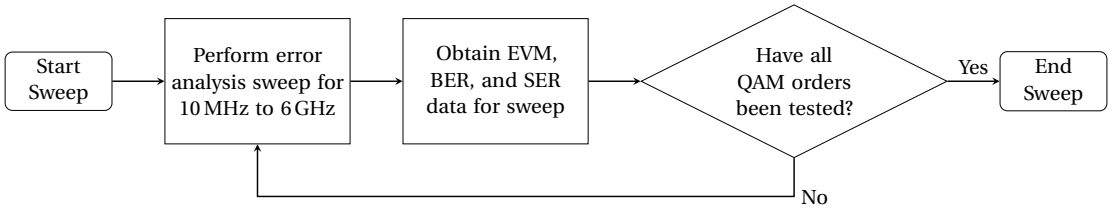

Figure 5.2: Flowchart of the experimental process specific to the VST. The output power is configured before commencing the sweep.

calculating these measurements have been presented in Section 3.3.

To measure the relationship between EVM and the BER and SER, VST output powers of –9 dBm and –27 dBm are tested. The experimental processes of the VST are repeated for each output power selected. The maximum output power of –9 dBm is selected as it remains below the level at which the VST warns of overloading the input RF terminal after the RF signal is passed through the Li-ion cell, which may cause waveform clipping, signal corruption, and potential damage to the equipment. The much lower output power of –27 dBm is expected to cause a great increase in EVM, and highlight further susceptibility to changes in the PLC channel of the Li-ion cell under test.

A summary of the experimental process using the VST is shown in Figure 5.2, and a technical overview of this experimental process has previously been shown in Figure 3.7.

5.1.2 Lithium-ion Cell Preparation

A single 18650-type Panasonic NCR18650BD-model Li-ion cell is tested in this experiment. The Li-ion cell is tested at SoCs of 95 %, 80 %, 60 %, 40 %, 20 % and 5 %. 5 % and 95 % represent SoCs where the Li-ion cell is near the state of complete discharge and fully charged, respectively. The other SoCs selected are equally separated with a step of 20 %. The voltages used for charging and discharging the Li-ion cell to specific SoCs are derived from the data provided on the manufacturer datasheet. The Li-ion cell is to be within ±2 % of the desired SoC before commencing each experiment.

The Li-ion cell is discharged to the required SoC using a power resistor and a microcontroller for SoC monitoring and automatic safety shut-off. An overview of

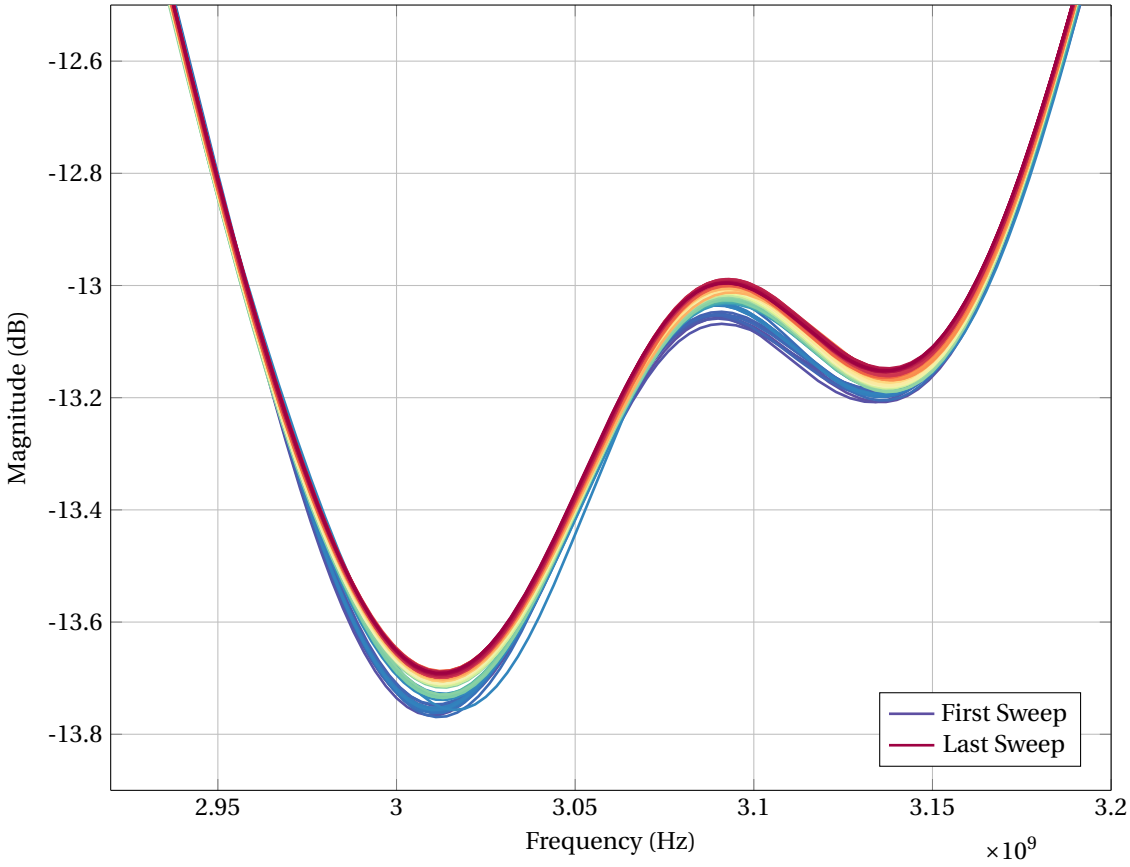

Figure 5.3: Timed sweep for 30 minutes with a step of 10 seconds of the Li-ion cell S21 magnitude with carrier frequency, immediately after discharging to 20 % SoC. The frequency range is reduced to show only the greatest change in S21 magnitude for all the frequencies test. The first sweep is coloured blue and each sweep thereafter uses a gradient of colour where the final sweep is in red.

the discharging apparatus is shown in Figure 5.4. The microcontroller uses a 10-bit analogue to digital converter (ADC) to measure the voltage of the cell. The 10-bit ADC allows for a precision of approximately 5 mV. The N-channel MOSFET is switched off before the ADC samples the voltage of the cell, since the voltage of the cell decreases with higher current draw. This MOSFET is controlled by the microcontroller. To discharge the cell, the N-channel MOSFET is switched on by increasing the gate voltage above the threshold voltage of the MOSFET. When the MOSFET is switched on, the current from the cell passes through the 4.7 Ω power resistor and the MOSFET to ground. The power resistor dissipates the energy as heat. Therefore, a heat sink

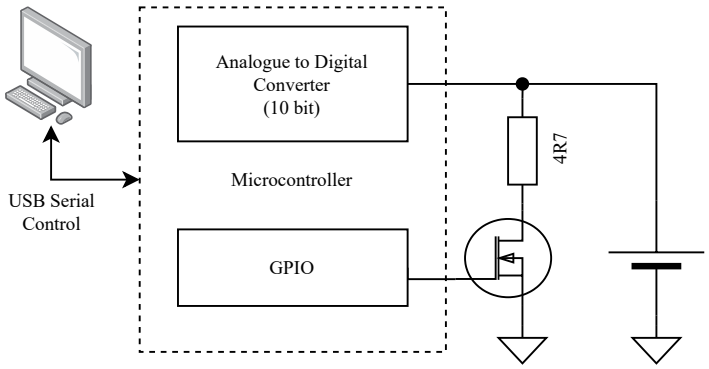

Figure 5.4: Overview of the discharging apparatus.

is attached to the power resistor and the resistance of 4.7 Ω both ensure that the temperature of the resistor is not hot to touch during discharging. The USB Serial connection provides status monitoring of the system, including cell voltage, discharge status, and setting a new target cell voltage.

The cell will remain clamped within the series-through cell holder during the discharging process. Once the discharging is completed, the cell holder is disconnected from the discharging apparatus and left to cool-down for a period of 30 minutes. Based on this experiment, it is observed that the magnitude and phase of the S21 transmission coefficient of the Li-ion cell do not change anymore with time after this cool-down period. It is shown in Figure 5.3 that the S21 magnitude had changed slightly during the cool-down period after discharging. The cool-down period is therefore essential in maintaining accurate results, as the charging of the Li-ion cell may cause some changes in cell characteristics, such as internal resistance, resulting from the changes in its core temperature, as described in Section 2.4.

5.1.3 Experimental Procedure

The individual measurement processes of using the Li-ion cell with the VNA and the VST are combined into a single experimental procedure, of which an overview is shown in Figure 5.5. The main details of the use of the VNA and VST have already been presented in Sections 3.2 and 3.3, respectively.

To reduce the effects of electromagnetic interference (EMI), the experiment is con-

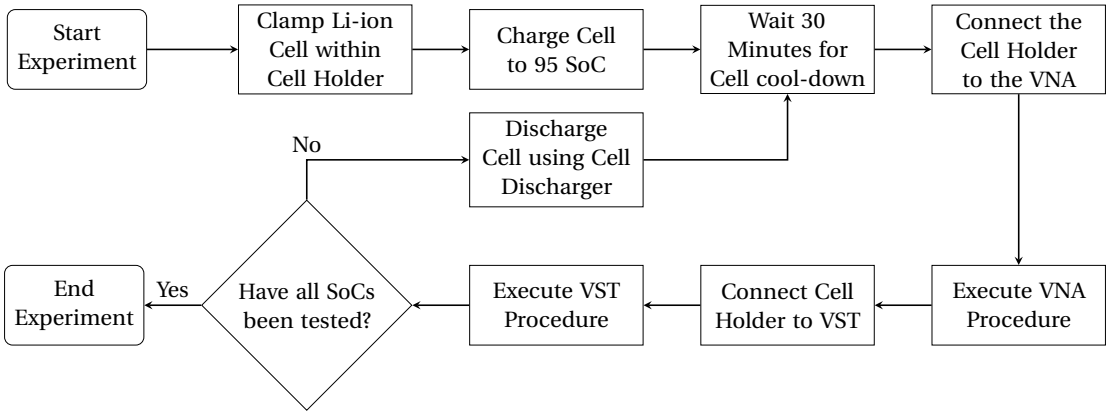

Figure 5.5: Flowchart of the overall experimental process for obtaining insights into the characteristics of a Li-ion cell at various SoCs and into the associated quality of in-situ PLC.

ducted in WMG's vehicle drive-in anechoic chamber inside the National Automotive Innovation Centre at the University of Warwick, U.K.. The ambient temperature within this chamber is set to 20 °C for the duration of the experiment.

The procedure of the experiments is now presented. The Li-ion cell is first prepared by placing it within the series-through cell holder. The screws of the cell holder are tightened at a defined torque to keep the cell firmly clamped. The cell is charged to an SoC of 95 %. After the cool-down period of 30 minutes, the cell holder is connected to the VNA to measure the S21 magnitude of the Li-ion cell as a communication channel.

The second step, with the cell holder connected to the VNA, 100 frequency sweeps are executed consecutively using the virtual instrument standard architecture (VISA) communication interface described in Section 3.2. Thereafter, the cell holder is disconnected from the VNA and connected to the VST at a defined torque such that the positive terminal of the cell is connected to the RF input. The bespoke program made for this experiment is started on the VST, which executes the transmission and receiving of QAM signal data, and records the received demodulated symbol data and phase error traces for each carrier frequency tested. The technical details of this bespoke program have already been presented in Figure 3.7. Finally, the cell holder is disconnected from the VST, and connected to the discharging apparatus for discharging to the next SoC. The process is repeated for all of the SoCs under consideration within the experiment.

The magnitude and phase of the S21 transmission coefficient are retrieved from the VNA and processed to achieve phase compensation, as stated in Section 3.2. These results are combined with the results of other SoCs to highlight the alterations in the transmission coefficient's magnitude and phase with SoC. The symbol data and phase error traces from the VST are retrieved with the symbol data processed to obtain the EVM, BER, and SER for all SoCs tested. The phase error traces allow for further analysis and investigation into how phase error in QAM symbols may cause instances of increased bit and symbol error.

5.2 Results and Analysis

This section presents the results obtained from the experimentation described in Section 5.1, and discusses the changes in cell characteristics with SoC by considering PLC performance.

Using the S21 magnitude and phase shift data of the 100 sweeps performed, and taking into account the standard deviation within such single set of measurements and the reproducibility in cell charging, the achieved error margins are ±0.1 dB and ±1.0°, respectively.

5.2.1 S21 Analysis

Figure 5.7 shows the change in S21 magnitude of the Li-ion cell as the SoC is decreased in comparison to the baseline of 95 % SoC, presented in Figure 5.6. It can be seen that the change in S21 magnitude is dependent on the frequency tested. This may be due to multipath fading, which as stated in Section 2.7, is caused by signals transmitted through multiple paths reaching the receiver at different times, resulting in a reduction in S21 magnitude which can degrade communication performance. The changes in S21 magnitude with frequency may therefore be due to the changing intensity of attenuation caused by the multipath fading. It is expected that significant attenuation in S21 magnitude will also cause increases in EVM, BER, and SER, indicating the relationship between increased communication error and decreased S21 magnitude. Furthermore, it can also be seen in Figure 5.7 that some frequencies display greater change with SoC than others. However, the measured S21 magnitude presented in

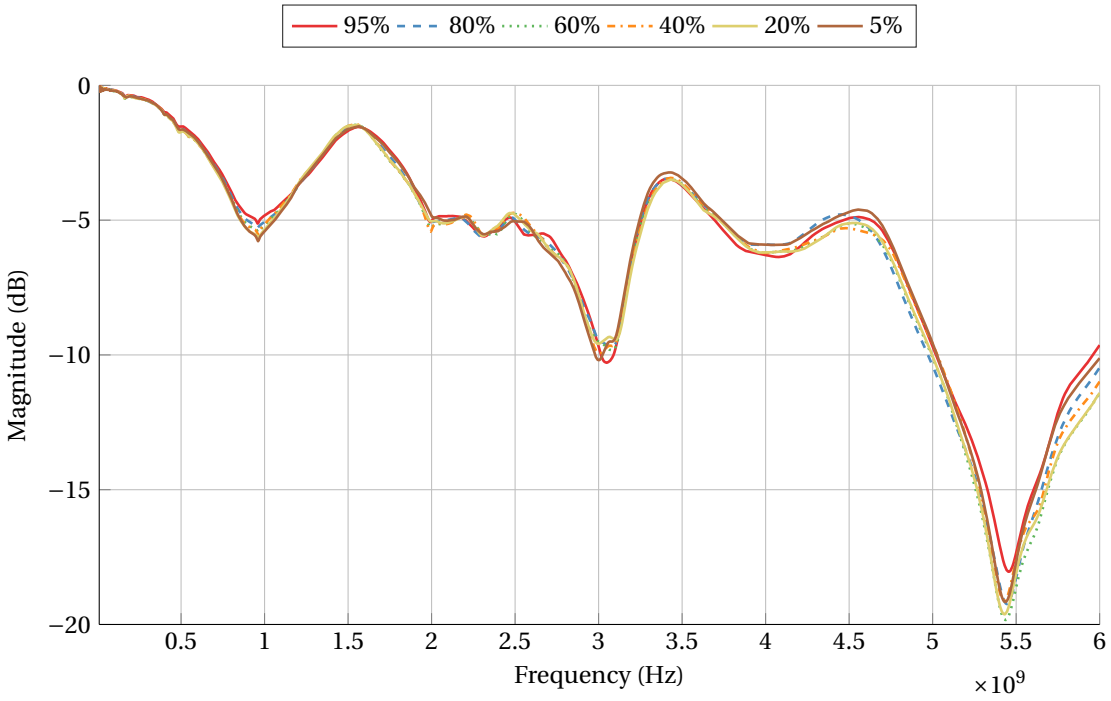

Figure 5.6: Measured S21 magnitude of a Li-ion cell at various SoCs.

Figure 5.6 shows that the carrier frequency has the most significant impact on the S21 magnitude. By comparing the changes in S21 magnitude with each SoC, the effects of the experimental setup, such as the cell holder on multipath fading, are eliminated, allowing for specific analysis of the effects of the cell SoC on the communication channel, rather than the full experimental setup.

The variations in S21 magnitude with SoC are now observed and analysed. The first relatively major deviation in S21 magnitude can be seen at 964 MHz, whereby the S21 magnitude of the signal across the Li-ion cell at 5 % SoC is decreased by 0.7 dB in comparison to the baseline of 95 % SoC. In addition, between frequencies of 904 MHz and 975 MHz, it can also be observed that there is a gradual, almost linear trend between the S21 magnitude of the signal and the SoC, whereby the S21 magnitude is reduced with decreasing SoC.These results are summarised in Table 5.1. Within these range of frequencies, the characteristics of the Li-ion have changed with SoC such that the difference in S21 magnitude is noticeable. However, Figure 5.6 shows that these differences in S21 magnitude between the various SoCs tested are far smaller

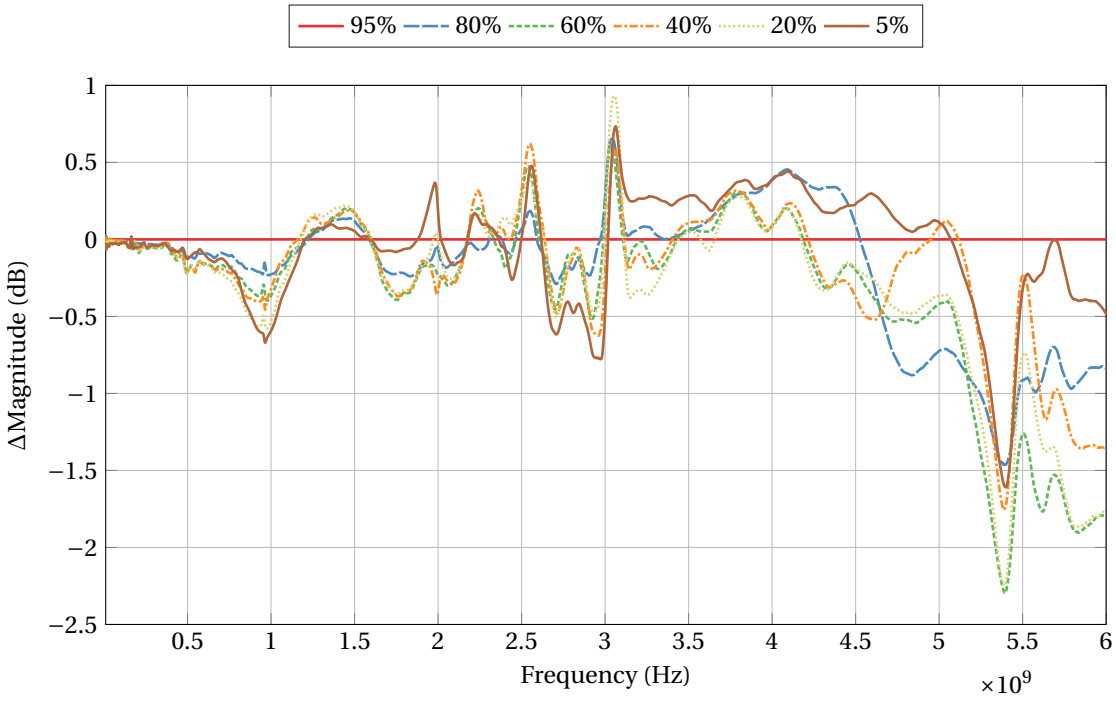

Figure 5.7: Change in S21 magnitude of the Li-ion cell at various SoCs, using 95 % SoC as a baseline.

than the decrease in S21 magnitude for all of the SoCs tested, with a local minimum of –5 dB for 95 % SoC. At this local minimum, it can be deduced that a destructive effect is occurring at the receiver due to the multipath effect, in addition to a slight dependence on the cell SoC. Despite this relatively small alteration in S21 magnitude with SoC, it will be later shown that the root mean square (RMS) EVM of 5 % SoC deviates significantly by –6 dB at 1 GHz, demonstrating that changes in SoC do have a noticeable effect on the communication system. However, this effect could only be seen with RMS EVM, as the BER and SER did not indicate any additional error within 904 MHz to 975 MHz.

This linear trend is broken as the frequency rises from 975 MHz whereby the change in magnitude with SoC decreases to becoming SoC independent in the frequency range from 1157 MHz and 1225 MHz. The S21 magnitudes for all SoCs begin to rise, reaching a local maxima of –2 dB at 1500 MHz. At this frequency, it can be deduced that neither the cell SoC nor the experimental setup has any significant effect on the S21 magnitude. Hence, a carrier frequency of 1500 MHz may therefore

Table 5.1: Changes in S21 magnitude (in dB) with SoC at selected frequencies using a baseline of 95 % SoC.

Frequency \ SoC	5 %	20 %	40 %	60 %	80 %
964 MHz	–0.7 dB	–0.6 dB	–0.5 dB	–0.4 dB	–0.2 dB
1982 MHz	0.4 dB	0.0 dB	–0.3 dB	–0.2 dB	–0.1 dB
2549 MHz	0.5 dB	0.4 dB	0.6 dB	0.5 dB	0.2 dB
2709 MHz	–0.6 dB	–0.5 dB	–0.5 dB	–0.4 dB	–0.3 dB
2978 MHz	–0.8 dB	–0.3 dB	–0.6 dB	–0.2 dB	0.0 dB
3052 MHz	0.7 dB	0.9 dB	0.6 dB	0.5 dB	0.6 dB
5397 MHz	–1.6 dB	–2.2 dB	–1.7 dB	–2.3 dB	–1.5 dB
6000 MHz	–0.5 dB	–1.8 dB	–1.4 dB	–1.8 dB	–0.8 dB

be preferred for an in-situ battery PLC system as the communication channel is not affected by changes in SoC and the effects of multipath fading are reduced. Despite these facts, this frequency displays changes in phase with SoC, as it will be shown in Section 5.2.2. Therefore, the receiver must be able to perform phase compensation in order for synchronisation and QAM demodulation to be correctly performed. The magnitude then begins to decrease, where at 1982 MHz, a small peak of 0.4 dB can be seen with 5 % SoC only, with the other SoCs remaining with a negative magnitude relative to the baseline. As the frequency increases, the change in magnitude with SoC rises and falls between ±0.5 dB with no clear trend visible. Within 2000 MHz to 2500 MHz, the measured S21 magnitudes for all SoCs remain relatively constant at –5 dB. In addition, the measured phases between these frequencies rise constantly from 50° to 75°. When the 95 % baseline is considered however, it can be observed that changes in phase magnitude do occur within ±2.5°, as explained in Section 5.2.2. With adequate phase compensation on the QAM transceivers, it is possible to obtain a bandwidth of 500 MHz within this range of frequencies thanks to the lack of changes in S21 magnitude. At 2549 MHz, a peak of 0.6 dB can be seen with 40 % SoC. Peaks of smaller change in magnitude can also be observed with the other SoCs, where with

80 % SoC having the smallest change in magnitude relative to the baseline.

Moreover, this peak in magnitude sharply falls to a broad negative peak from 2592 MHz to 3018 MHz. Within this range, a weak trend can be seen between 2662 MHz and 3009 MHz whereby 5 % SoC shows the lowest magnitude relative to the baseline. This trend is briefly lost between 2757 MHz and 2867 MHz where 20 % to 80 % SoC are less than –0.2 dB and within 0.1 dB of each other, whilst 5 % SoC remains more than –0.4 dB from the baseline. A sharp peak can be seen at 3052 MHz which shows the greatest positive difference in magnitude of 0.9 dB relative to the baseline for all frequencies tested. This trend coincides with a large minimum at 3000 MHz in S21 magnitude for all SoCs tested reaching –10 dB, suggesting an increased behaviour of attenuation due to multipath fading. Due to this minimum in S21 magnitude and also the change in magnitude with SoC, this frequency will not be suitable for use in an in-situ battery PLC system.

After this peak, the change in magnitude falls and remains within ±0.5 dB until 4500 MHz where the magnitudes begin to decrease relative to the baseline. At this frequency, the measured S21 magnitude begins to decrease from –5 dB up to nearly –20 dB at 5397 MHz, demonstrating great attenuation. In addition, the differences in magnitude between SoCs continues to increase with a peak at 5397 MHz of –2.3 dB for 60 % SoC. At this peak, whilst 80 % SoC displays the lowest change in magnitude relative to the baseline compared to the other SoCs, it is the greatest change in magnitude from the baseline for this SoC for all frequencies tested. After this peak, the magnitudes of each SoC remain the furthest apart up to 6000 MHz, with 5 % SoC approaching the baseline, whereas the other SoCs are spread relatively evenly up to –1.9 dB. Therefore, carrier frequencies above 4500 MHz should not be selected for an in-situ battery PLC system. This is not only due to the increased effect of multipath fading in the measured S21 magnitude, but also due to the greatest change in magnitude with SoC, which may increase as additional cells are added to the configuration, as investigated in Chapter 6. However, the communication error testing performed in this chapter does not exhibit any change in error above 4500 MHz. This is due to the capability of the VST to utilise synchronisation and to perform normalisation, effectively correcting for the impact of the Li-ion cell on the communication channel.

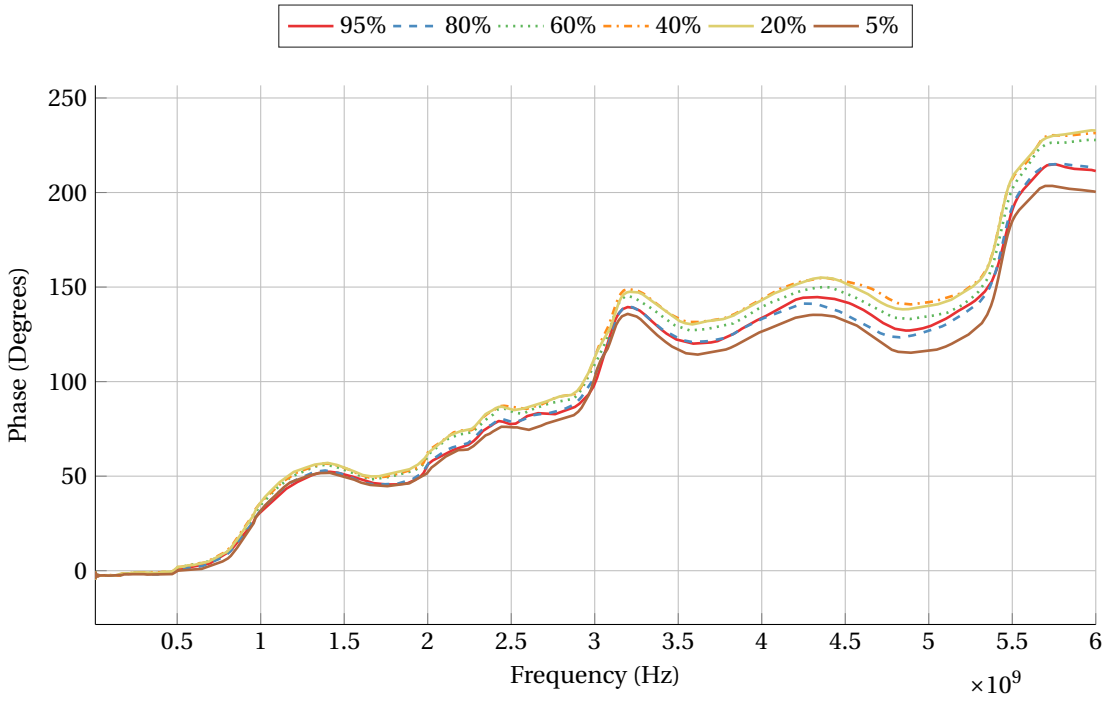

Figure 5.8: Measured phase of a Li-ion cell at various SoCs with carrier frequency.

5.2.2 Phase Analysis

The measured phase for all SoCs tested are presented in Figure 5.8, and the change in phase of the Li-ion cell as the SoC is decreased in comparison to the baseline of 95 % SoC is shown in Figure 5.9. Similar to the changes in S21 magnitude described in Section 5.2.1, it can be observed that the most significant changes in phase occur with changes in the tested carrier frequencies. Some sharp changes in phase occur at the same frequencies where sharp changes in S21 magnitude take place, however there are some distinct differences between them, particularly for 5 % SoC, as shown in Table 5.2. Furthermore, it is also seen that there are changes in phase with SoC of up to 17.1°. An analysis of these results is presented in this section.

As the frequency increases from 10 MHz, the difference in phase shifts for all SoCs decrease in comparison with the 95 % SoC baseline, and follow a weak negative trend whereby lower SoCs display a greater phase shift, but only when 5 % SoC is not considered. The lowest SoC of 5 % yields the smallest phase shift, whilst the phase shift of 20 % remains farthest from the baseline. The measured phase shown in Figure 5.8

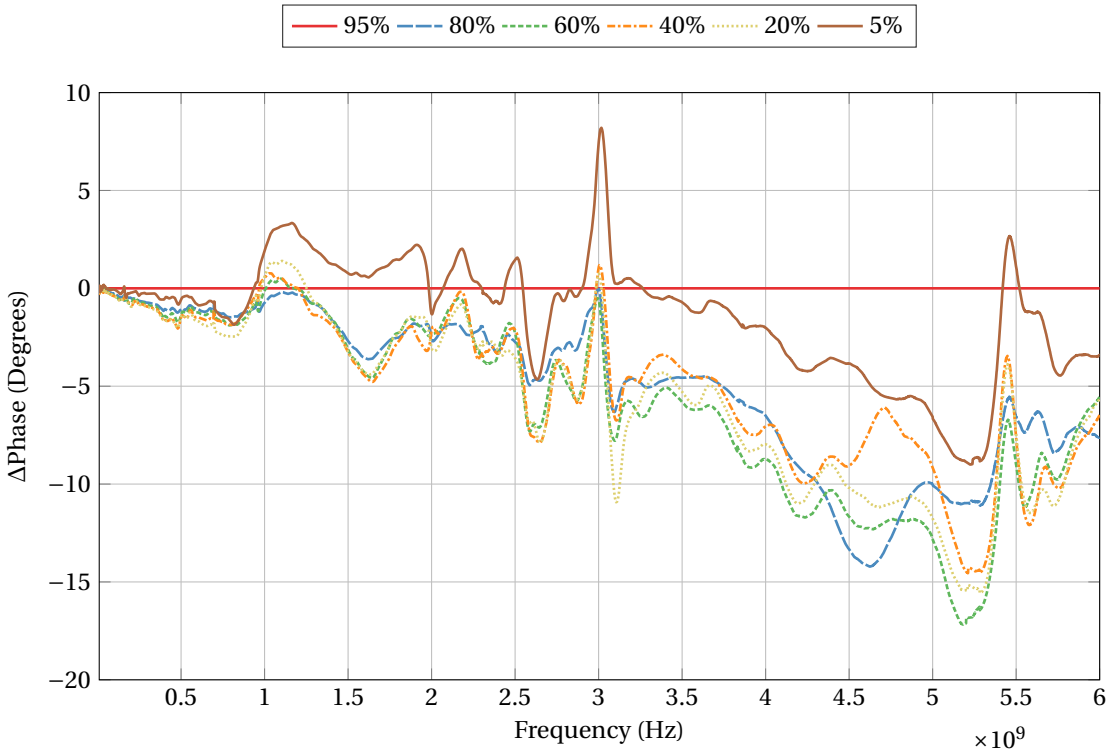

Figure 5.9: Change in phase of a Li-ion cell at various SoCs, using 95 % SoC as a baseline.

shows a relatively constant phase close to 0° up to a carrier frequency of 875 MHz, which coincides with a change in the weak trend in the magnitude of the change in phase shift with SoCs, whereafter the phase shifts of all individual SoCs begin to decrease by varying amounts in comparison to the baseline, whilst the measured phase begins to increase. Such a change in phase at this frequency is caused by changes in the reactance of the communication channel. Despite this fact, the change in phase with SoC at 875 MHz shows only a maximum difference in phase shift of 3°, demonstrating that the Li-ion cell does not change in reactance with SoC, but is rather caused by the entire communication channel, including the cell. This change in reactance may cause multipath fading, which can cause signal attenuation and a phase shift due to the propagation of signal on various paths that reach the receiver at different times, leading to constructive or destructive interference. At this frequency, a destructive interference is occurring due to the change in phase shift, whereas at

Table 5.2: Change in phase shift (in degrees) with SoC at select frequencies using a baseline of 95 % SoC.

Frequency \ SoC	5 %	20 %	40 %	60 %	80 %
820 MHz	−1.6°	−2.2°	−1.8°	−1.6°	−1.5°
1165 MHz	3.6°	1.4°	0.1°	0.2°	−0.3°
1649 MHz	1.0°	−4.1°	−4.8°	−4.4°	−3.7°
2001 MHz	−1.1°	−2.8°	−2.2°	−2.2°	−2.7°
2632 MHz	−4.4°	−7.2°	−7.8°	−6.9°	−4.6°
3015 MHz	8.4°	0.5°	1.0°	−1.4°	−0.7°
3106 MHz	0.5°	−10.5°	−6.7°	−7.5°	−6.0°
5187 MHz	−8.6°	−15.2°	−14.3°	−17.1°	−11.0°
5450 MHz	2.6°	−3.7°	−3.6°	−6.8°	−5.6°
6000 MHz	−3.2°	−5.4°	−6.5°	−5.6°	−7.6°

frequencies below 875 MHz, a multipath fading effect cannot not be observed.

From 936 MHz, the phase shift of 5 % SoC rises, reaching a peak of 3.3° at 1165 MHz. The phase shifts of the other SoCs also rise with respect to the baseline of 95 %, but by a much lower amount. In fact, only the phase shift of 80 % SoC remains negative at this frequency with a value of –0.2°. The phase shift of all SoC continues to rise gradually at 1165 MHz, suggesting a continuation of the increasing multipath fading beginning from 875 MHz. The difference in relative phase shift between 5 % SoC and the other SoCs remains intact. This behaviour continues through the minimum in phase at 1649 MHz whereby 40 % SoC displays the highest relative phase shift of –4.8°, followed closely by 60 %, 20 % and 80 % SoC. This result demonstrates that the SoC is having a negative effect on the communication channel due to changes in cell reactance with SoC. These changes in phase with SoC indicate that the receiver is required to perform synchronisation at regular intervals to ensure that the correct phase offset is applied as the Li-ion cell, that is being used as a communication channel, is being charged and

discharged. The relatively large phase shift of 5 % SoC begins to subside at 1925 MHz and approaches the other SoCs at 2001 MHz. At this frequency, the relatively stable phase shift of all SoCs between 1200 MHz to 2001 MHz begins to increase once again, continuing at an almost constant gradient until 2907 MHz reaching a phase of 100°. At 2001 MHz, the change in phase shift of 5 % SoC remains up to 7.5° from any other SoC apart from the baseline. Despite this behaviour, the same features that are present with the other SoCs are also displayed in 5 % SoC. This includes the sharp minimum at 2632 MHz whereby 5 % SoC reaches a relative phase shift of –4.7°, whereas the largest phase shift recorded at this frequency is –7.8° with 40 % SoC. At this frequency, the phase shift of 80 % SoC is shown to deviate from the SoCs of 20 %, 40 % and 60 % where at lower frequencies these SoCs are within 1° from each other, the phase shift of 80 % SoC is now the same as that for 5 % SoC. This deviation in phase shift between the SoCs tested is also noticeable in Figure 5.8, and demonstrates that between 2001 MHz and 2907 MHz the phase shift of the communication system is not only affected by the changes in cell SoC, but also by the entire experimental setup and by the fixed characteristics of the cell, i.e. the characteristics that do not change with SoC.

Beginning at 2907 MHz, a large maximum develops in phase shift with respect to the baseline SoC of 95 %. At 3015 MHz, 5 % SoC produces the greatest rise in phase shift at this frequency, reaching a peak of 8.2°. The same feature can be seen in the other SoCs, whereby the positive change in phase shift causes the relative negative phase shift of these SoCs to approach the baseline. After this peak, the phase shifts of all SoCs with respect to the baseline begin to fall, with the phase shift of 5 % SoC approaching the baseline, and the other SoCs becoming more negative, with 20 % SoC reaching –10.9° at 3106 MHz. The phase shift for all SoCs display an increased rate of change from 3015 MHz, reaching a peak at 3106 MHz of 150°. At this peak, the difference in phase shift with SoC is noticeable in Figure 5.8, and is also observed in Figure 5.9, the difference in phase between SoCs only becomes greater until the maximum frequency measured of 6000 MHz is reached. In this range of frequencies it can be deduced that both the fixed characteristics of the Li-ion cell and the differences in characteristics with SoC are causing these changes in phase shift due to the changes in the reactance of the cell.

As the frequency increases from 3015 MHz, both the relative phase shifts to the

baseline and the phase shifts of all SoCs increase. Between 3180 MHz and 4000 MHz minor peaks exist in SoCs of 5 %, 20 %, 40 % and 60 % relative to the baseline of 95 %. In contrast, 80 % SoC does not display such features, but rather gradually increases its phase shift, similar to the other SoCs, and continues to do so from 4350 MHz. Where the phase shifts of the other SoCs cease to increase here, the phase shift of 80 % SoC reaches a local maximum of –14.2°. This indicates a non-linear characteristic behaviour of the Li-ion cell, where the internal reactance is changing with SoC, but not with a noticeable trend. Because of these significant changes in phase shift with SoC, frequent synchronisation would be required at the QAM receiver in order to correctly compensate for this phase shift whilst the Li-ion cell is charging or discharging. The phase shift measured for all SoCs continues to remain between 120° and 152° until 5400 MHz, demonstrating a potentially viable bandwidth of 1200 MHz where the change in phase shift is not significant for a QAM transceiver system utilising periodic synchronisation, such as by using pilot symbols as discussed in Section 2.7. However, the change in phase shift with SoC becomes greatest within this bandwidth at 5187 MHz, hence the use of synchronisation may be necessary to avoid data corruption with changing SoC, as described later.

The phase shift of 40 % SoC decreases at 4700 MHz in comparison to the baseline of 95 % SoC, approaching the phase shift of 5 % SoC, and reaching a local minimum of –6.1°. Despite this behaviour, the phase shift of 40 % SoC rapidly increases and approaches 20 %, 40 % and 60 % SoC, whilst the phase shift of 80 % SoC decreases. The largest maximum of –17.2° develops at 5187 MHz with 60 % SoC. Following this, a sharp decrease in absolute phase shift occurs, with a local minimum of –3.5° at 5450 MHz with 40 % SoC, and the phase shift of 5 % SoC becoming positive. After this sharp peak, the phase shifts of all SoCs gradually decrease until 6000 MHz where the maximum relative phase shift is –7.6° with 80 % SoC.

Some features of relative phase shift discussed can be observed in all of the SoCs presented in Figure 5.8. It is shown that the actual phase shift of the 95 % SoC baseline exhibits such features as the sharp peak at 3015 MHz, which leads to proportional changes in phase shift of the other SoCs tested. This section has shown that changes in phase occur due to change in cell reactance which changes with frequency, and also with changes in SoC, in varying amounts over the frequencies tested. The effects

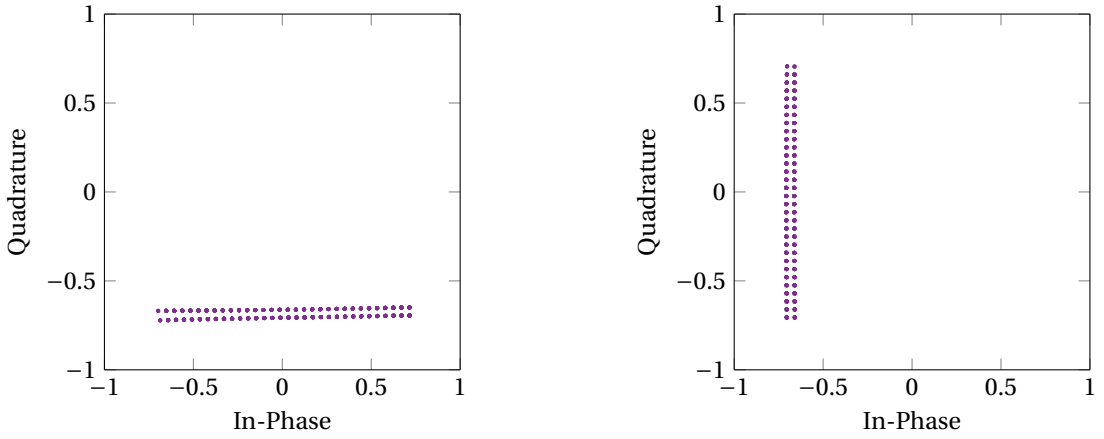

(a) Carrier frequency of 550 MHz.

(b) Carrier frequency of 600 MHz.

Figure 5.10: Scatter plots of the first 100 QAM symbols received by the VST during 1024-QAM PLC.

of the change in SoC on the communication error is addressed in Section 5.2.3.

5.2.3 Communication Error Analysis

In this section, the BER, SER and EVM of the PLC system are analysed and compared with each other and also with the results of the S21 magnitude and phase shift. The full results for BER and SER are presented in Figures 5.13 and 5.14, respectively. The results are the same for both –9 dBm and –27 dBm output power, hence the results for –27 dBm are omitted for brevity without loss of generality. These results indicate that there is no significant attenuation or phase shift on the PLC channel that results in any bit or symbol errors. However, the VST performs automatic filtering of the input RF signal, including synchronisation, normalisation and phase compensation. These techniques are typically required for QAM demodulators, as they allow for correct mapping of QAM symbols to the constellation space [170]. However, changes in S21 magnitude and phase shift during communication may still cause data errors should the frequency of synchronisation not be high enough before the changes in Li-ion cell characteristics become significant enough to cause such errors. As such, this investigation provides recommendations of communication parameters in order to mitigate such errors.

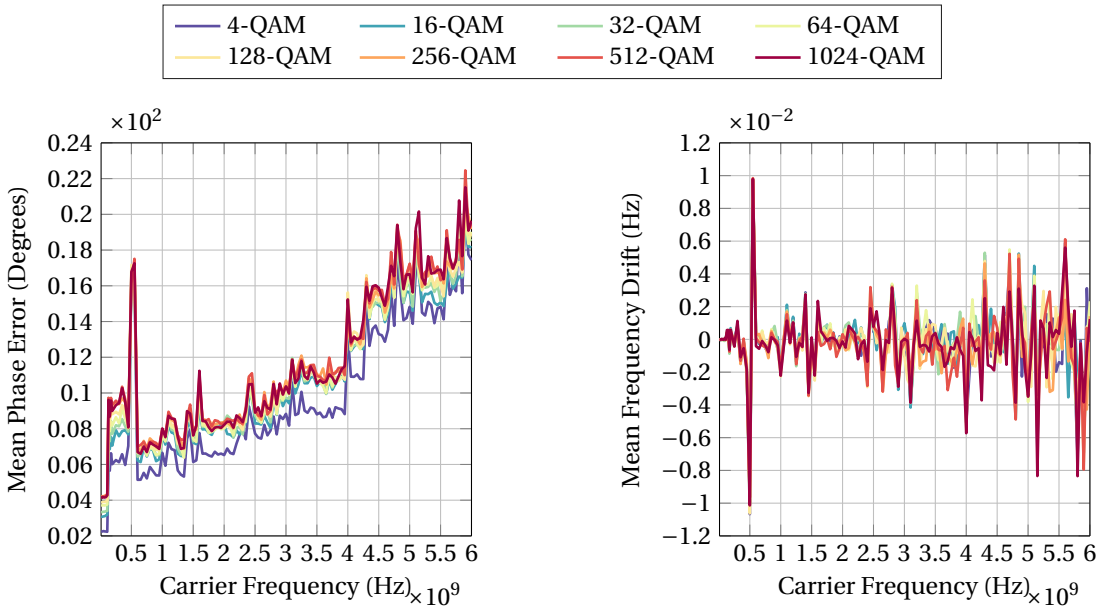

(a) Mean Phase Error

(b) Mean Frequency Drift

Figure 5.11: Mean phase error and mean frequency drift as detected by the VST for the 20 % SoC test.

The normalisation and phase compensation performed on the input RF signal removes all errors but a single increase in BER and SER at 550 MHz with 20 % and 40 % SoCs. At this frequency, the automatic phase shift compensation fails for the highest modulation order of 1024-QAM. Figure 5.10 displays the scatter plots of the first 100 symbols during a test of 1024-QAM at 550 MHz and 600 MHz, respectively. Whereas 600 MHz shows the lowest error ratio possible, the constellation of the 550 MHz symbol trace is phase shifted by –90°, which causes the maximum in BER and SER. The BER and SER measurements at –9 dBm demonstrates that the Li-ion cell as a communication channel does not cause any significant issue in this communication system when a QAM transceiver with signal conditioning techniques is utilised. These results highlight that communication errors can be reduced by reducing the modulation order of QAM or by increasing the magnitude of signal conditioning on the communication channel, as explained later in Section 5.3.

In Figures 5.11a and 5.11b at 550 MHz, a slight increase in mean phase error and frequency drift can be observed, respectively. The definitions of mean phase error and frequency drift can be found in [143]. These increases in error and drift can

be associated with the observation of incorrect phase shift compensation shown in Figure 5.10. Furthermore, EVM results presented in Figures 5.15 and 5.16 all display a large increase in EVM at 550 MHz, which remains constant regardless of the output power. Conversely, no significant peak can be seen at 550 MHz in S21 magnitude or phase shift, as presented in Sections 5.2.1 and 5.2.2. It can therefore be hypothesised that this error is not likely to be due to a change in characteristics of the Li-ion cell, but rather caused by an external factor, including the signal path and filter configuration used within the VST causing higher error ratios at this specific frequency.

The EVM results for –9 dBm and –27 dBm output power are presented in Figures 5.15 and 5.16, respectively. It can be observed that the reduced output power causes a slight rise in EVM for all carrier frequencies tested. This behaviour is due to the reduced output power being more susceptible to the effects of noise on the communication channel, such as EMI and multipath propagation. Due to time considerations, only –9 dBm and –27 dBm output powers have been tested in this chapter, but it is shown that some carrier frequencies display increased levels of EVM when a reduced output power of –27 dBm is used. It can be safely assumed that the reduction in output power would increase the effects of noise on the communication channel, and may therefore result in an increased number of data errors. Due to the stable response in BER and SER measured for these output powers, it is more beneficial to observe the EVM of the communication system which can be used to deduce thresholds of EVM with which data errors may begin to occur. The first large increase in EVM with an output power of –27 dBm is from 130 MHz to 400 MHz, whereby the EVM rises from –58 dB to –44 dB for all SoCs. In Figure 5.16e a peak in EVM of 1024-QAM occurs, reaching a maximum of –39 dB, before returning to the same EVM levels seen with other SoCs. There is no noticeable correlation between this wide peak in EVM with the S21 magnitude and phase results determined with the VNA. It may therefore be hypothesised that this increase in EVM is due to effects caused by the internal signal path and processing system of the VST, rather than changes in the characteristics of the communication channel. Another peak in EVM occurs at 800 MHz for 5 % SoC, as shown in Figure 5.16a, for 4, 32, 64 and mostly for 16-QAM, which reaches a value of –41.2 dB.

Another peak specific to 5 % SoC is seen at 1000 MHz, whereby the EVM of only

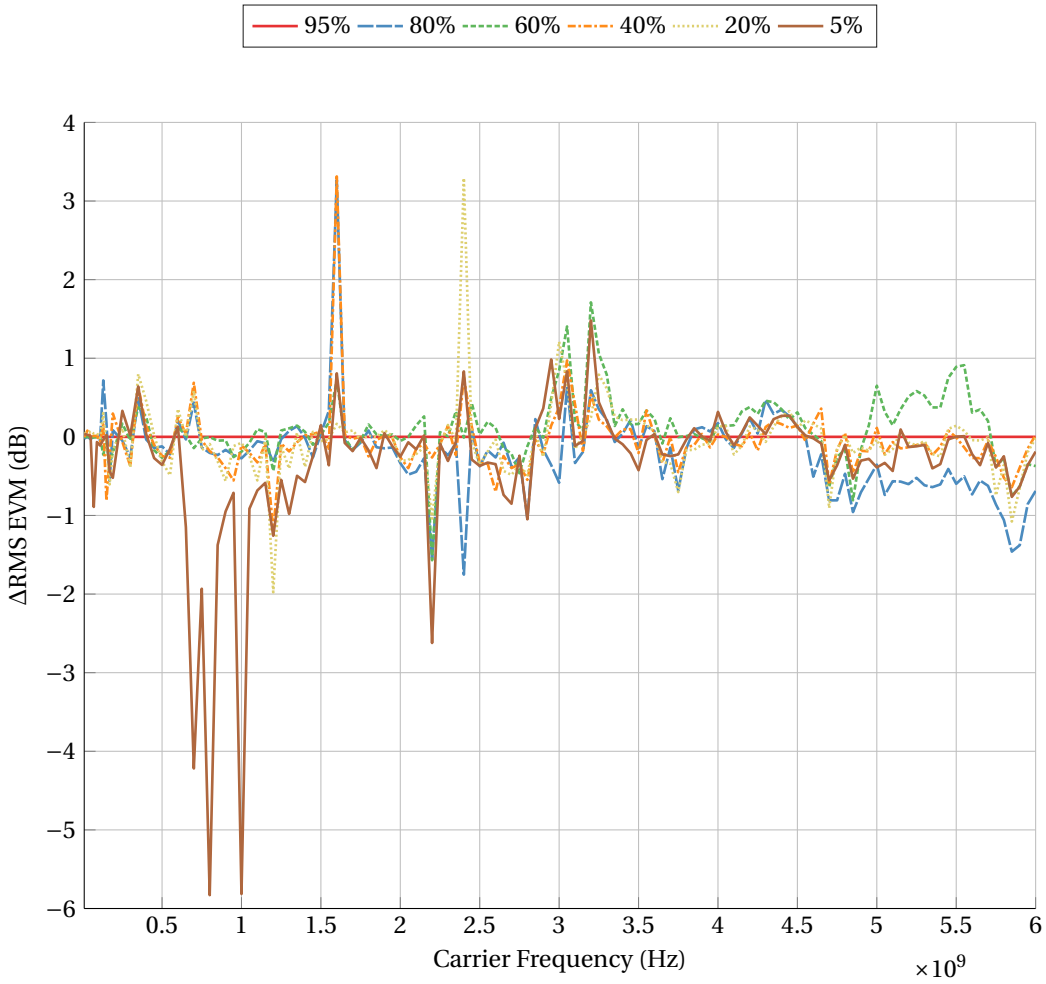

Figure 5.12: Change in RMS EVM of 4-QAM with SoC, using 95 % SoC as a baseline.

4-QAM rises to –49.5 dB. This peak may also be attributed to the sudden alteration in S21 magnitude and phase shift, where 5 % SoC shows changes distinct from the other SoCs tested. Since only 4-QAM shows this increase in EVM, it may be deduced that the VNA is unable to normalise or phase-compensate the 4-QAM symbol trace as effectively as the other modulation orders tested.

Figure 5.12 clarifies how significant the changes in EVM are at the frequencies of 700 MHz, 800 MHz and 900 MHz for 5 % SoC which reach –4.2 dB, –5.8 dB and –5.8 dB relative to the baseline of 95 % SoC, respectively. Because of the reduced step in frequency used on the VST in comparison to the VNA as discussed in Section 3.3,

the peak in EVM at these specific frequencies is not recorded. Hence the specific cause of this increased level of EVM may be multipath fading which also causes the corresponding peaks in both phase and S21 magnitude. It should be noted that the normalisation and phase compensation process of the VNA is unable to completely filter this peak in EVM for these modulation orders, but is able to do this for 128, 256, 512, and 1024-QAM.

The next peak in EVM occurs at 1600 MHz for all SoCs, reaching an absolute value of –43.0 dB. Figure 5.12 shows that relative to 95 % SoC, 40 % SoC has the greatest EVM at this peak, whereas 95 % SoC has the lowest EVM. At this frequency, a correlation can be observed with the gradual minima occurring in S21 magnitude and a peak in negative phase shift, relative to their baselines. At this frequency, only a gradual change in the measured S21 magnitude and phase shift occurs with all SoCs tested, suggesting that a change in SoC does in fact cause an increase in EVM. Despite this fact, this increase in EVM is not profound enough to cause any data corruption.

A smaller peak in EVM occurs at 2200 MHz, reaching to an EVM of –50.6 dB with 5 % SoC. At this frequency, Figure 5.12 shows that there is a variation of up to –2.6 dB in EVM, where 5 % SoC has the highest EVM and 95 % SoC has the lowest. Furthermore, the largest peak in EVM can be seen at 2400 MHz, reaching –42.2 dB with 80 % SoC. A large variation in EVM occurs at this frequency, with 20 % SoC showing the least EVM of –47.3 dB. As it has already been shown, small peaks in both S21 magnitude and phase also occur at these frequencies relative to the baseline. However, at this frequency no significant changes in S21 magnitude and phase occur for all SoCs tested. This suggests that at 2200 MHz, only the sudden change in the phase relative to the 95 % SoC baseline, and hence the change in the cell reactance with SoC, may have caused this increase in EVM.

Commencing 3500 MHz, the EVM for all SoCs tested begins to rise gradually up to 6000 MHz. At 4700 MHz, the differences in EVM between the SoCs tested begin to diverge to a maximum of 1.5 dB. This increase in EVM may be attributed to numerous factors, including the increase in phase, and hence the reactance of the Li-ion cell, which increases sharply at 5500 MHz. Another factor is the S21 magnitude of the cell which displays its highest attenuation at the same frequency, in addition to the greatest change in S21 magnitude with SoC. This therefore demonstrates the greatest

change in the impedance of the communication channel, but also the change in impedance of the cell with SoC. Both the mean phase error and the mean frequency drift presented in Figure 5.11 have been shown to increase as the carrier frequency is also increased. As such, it may be hypothesised that the increase in carrier frequency towards the maximum capable of the VST used may have caused these increases in error correction limits of the VST. A broad minimum in EVM can be observed at 5700 MHz, which decreases in all SoCs. These characteristics can be seen in both S21 magnitude and phase results for all SoCs tested, which display a decrease in S21 magnitude and phase shift.

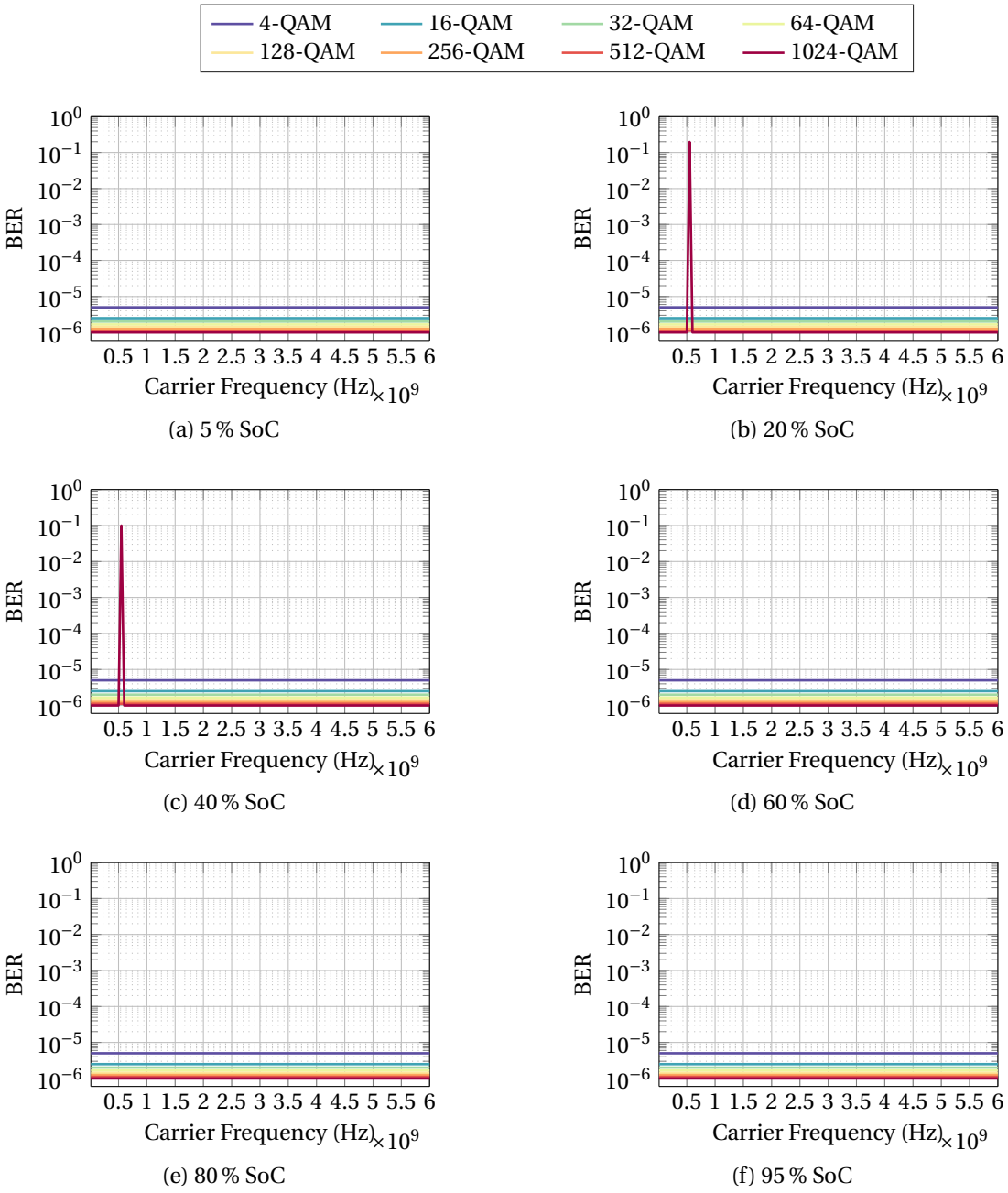

(a) 5 % SoC

(b) 20 % SoC

(c) 40 % SoC

(d) 60 % SoC

(e) 80 % SoC

(f) 95 % SoC

Figure 5.13: BER for QAM-signals transmitted with a peak output power of –9 dBm through a Li-ion cell at various SoC. Each QAM order is represented in a different colour. Each order of QAM has a different minimum BER since the number of transmitted symbols is kept constant, rather than the number of transmitted bits.

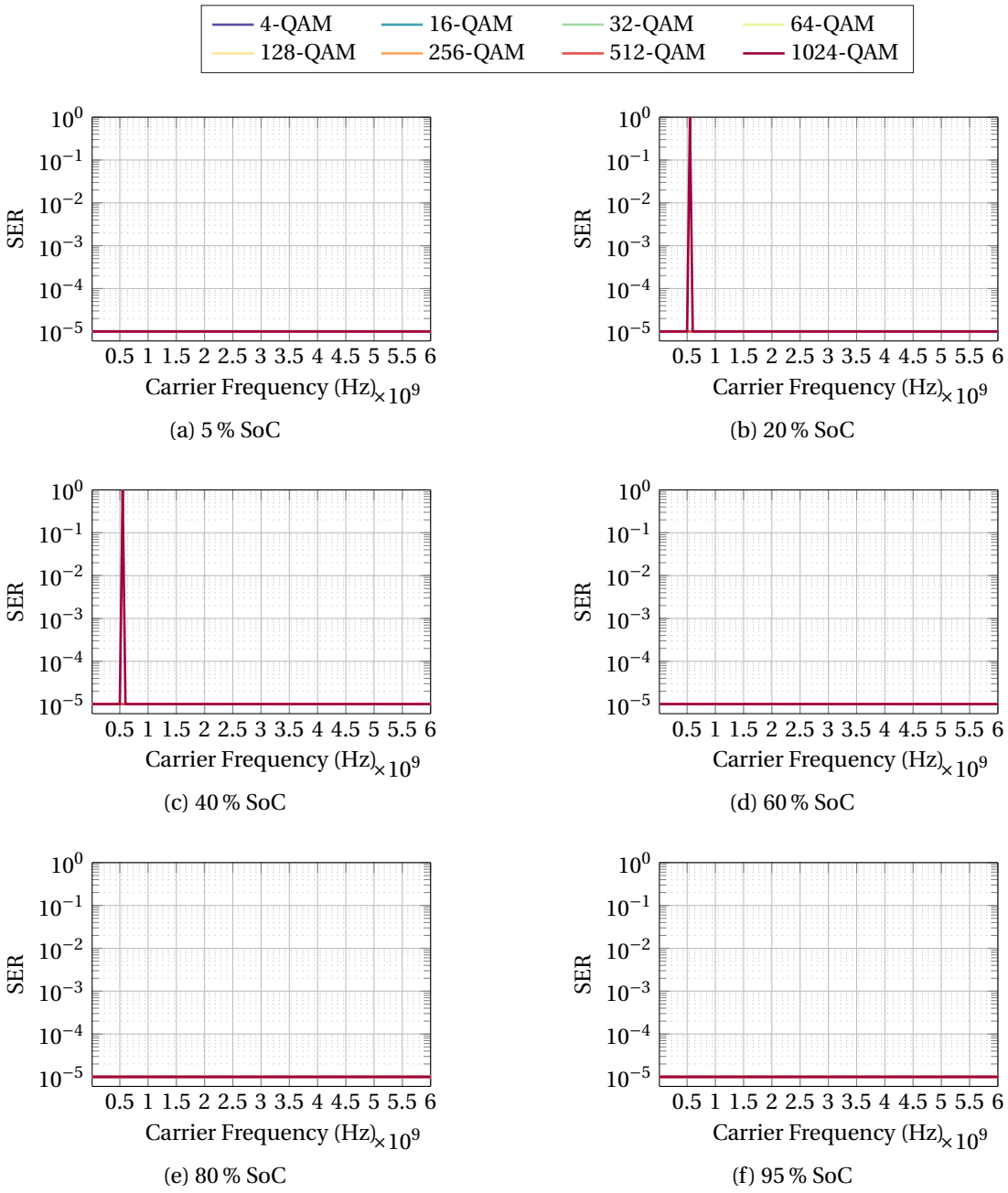

(a) 5 % SoC

(b) 20 % SoC

(c) 40 % SoC

(d) 60 % SoC

(e) 80 % SoC

(f) 95 % SoC

Figure 5.14: SER for QAM-signals transmitted with a peak output power of –9 dBm through a Li-ion cell at various SoC. Each QAM order is represented in a different colour.

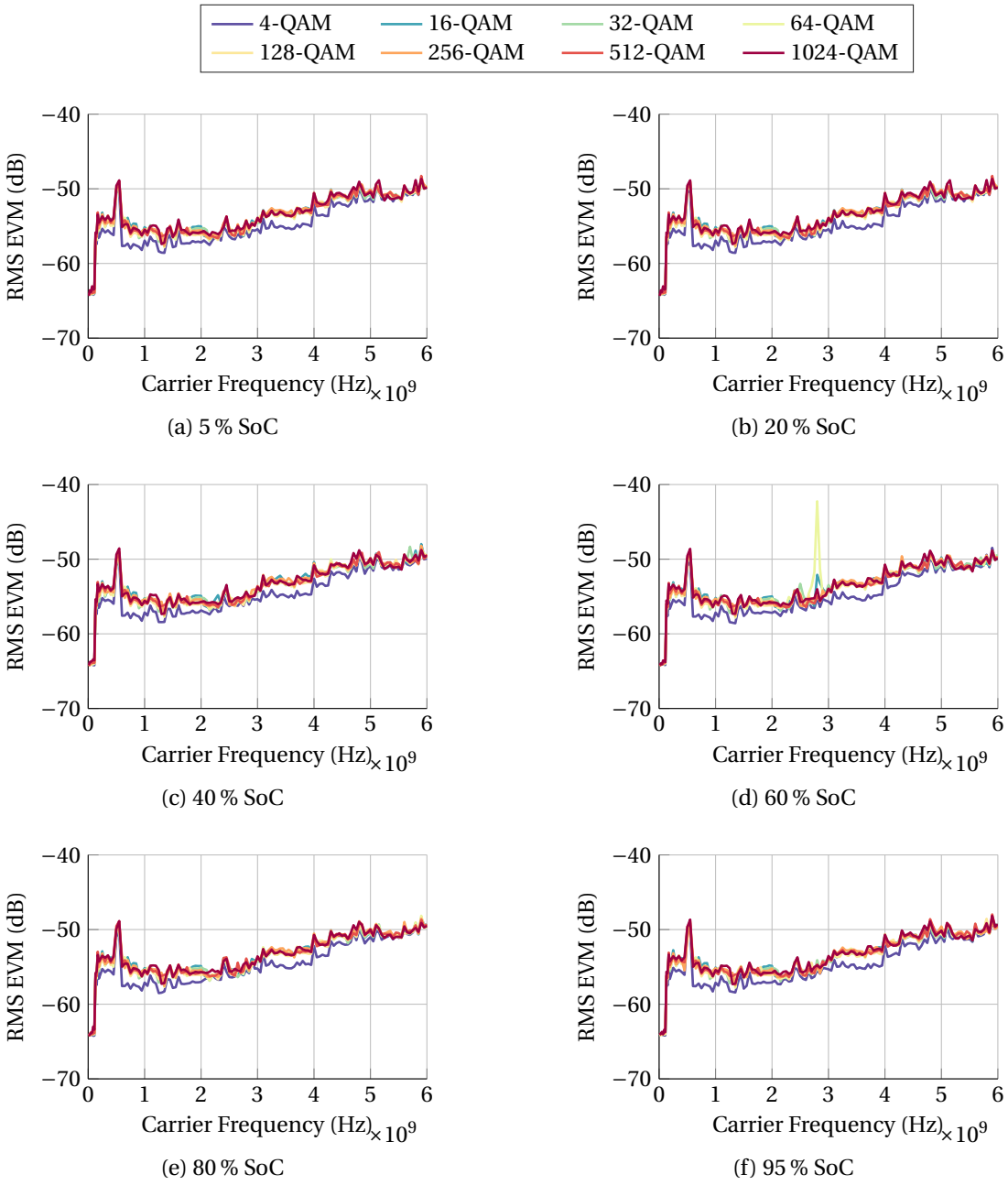

(a) 5 % SoC

(b) 20 % SoC

(c) 40 % SoC

(d) 60 % SoC

(e) 80 % SoC

(f) 95 % SoC

Figure 5.15: RMS EVM for QAM-signals transmitted with a peak output power of –9 dBm through a Li-ion cell at various SoC. Each QAM order is represented in a different colour.

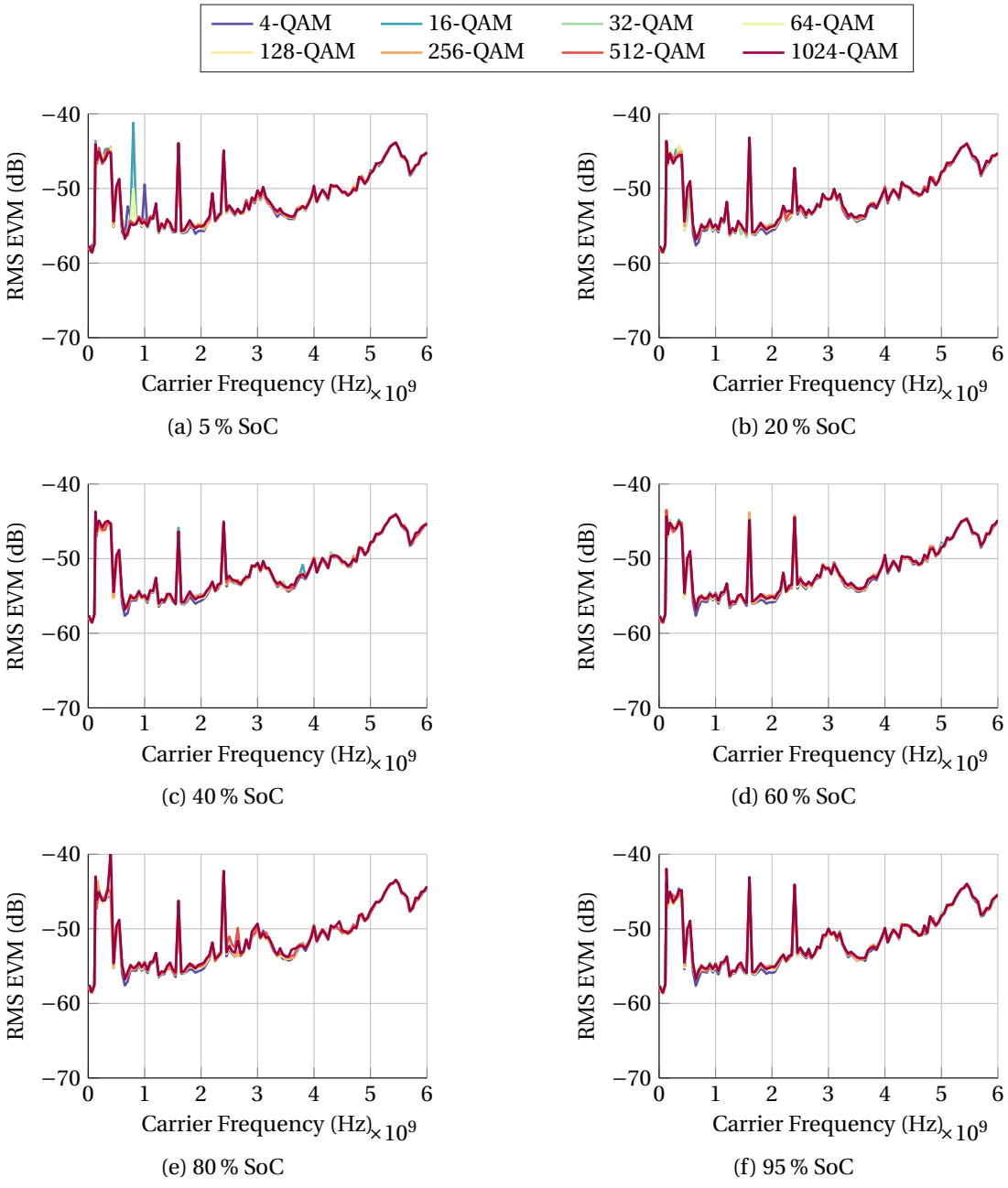

(a) 5 % SoC

(b) 20 % SoC

(c) 40 % SoC

(d) 60 % SoC

(e) 80 % SoC

(f) 95 % SoC

Figure 5.16: RMS EVM for QAM-signals transmitted with a peak output power of –27 dBm through a Li-ion cell at various SoC.

5.2.4 Overall Analysis and Discussions

The presented experimental results have shown that changes in Li-ion cell SoC lead to changes in in-situ PLC channel characteristics of both the S21 magnitude and phase over the RF frequency range from 10 MHz to 6 GHz. At some frequencies, sharp changes in these characteristics occur which cause an increase in EVM. Exemplary frequencies include sharp changes in S21 magnitude and phase at 1165 MHz and 3015 MHz, respectively, which occur for all SoCs tested relative to the respective baselines of 95 % SoC. In addition, it is shown that 5 % SoC yields the largest change in phase shift for most frequencies, whereas the largest change in magnitude is not observable with 5 % SoC. In fact, 60 % SoC displays the largest change in magnitude for all frequencies tested at 5397 MHz. At certain frequencies, some trends between the SoC and both the S21 magnitude and phase are noticed, whereby the S21 magnitude and phase characteristics are in a almost linear order of 95 % to 5 % SoC. This behaviour can be observed between frequencies of 904 MHz and 975 MHz for S21 magnitude, and a weaker trend at 10 MHz and 875 MHz for phase shift, where only the phase shift of 5 % SoC deviates from this trend by remaining consistently between 95 % and 80 % SoC.

The EVM results verify that some increases in error can be attributed to certain changes in the characteristics of the Li-ion cell, such as impedance. In particular, it is found that large changes in S21 magnitude and phase correlate to specific increases in EVM, such as for carrier frequencies between 1600 MHz and 2400 MHz. However, BER and SER results indicate that these increases in EVM are not significant to impede the successful demodulation of the signal data by the VST. The VST uses a filtered signal path, with normalisation and phase shift compensation, which is expected to automatically improve the results. Nevertheless, these are features which are available to most QAM demodulators, as discussed in Section 5.1.

Based on this study, it can be implied that smaller changes in S21 magnitude and phase with SoC at a given frequency will benefit an in-situ Li-ion PLC network. This is because less reconfiguration of the transmitter and the receiver will be required as the Li-ion cell's SoC changes. For example, if 3000 MHz is selected as a PLC carrier frequency, it is possible that data corruption can occur when the SoC of the Li-ion cell is decreased to 5 % due to the relatively large changes that occur in S21 magnitude

and phase shift of 0.9 dB and 8.2°, respectively.

From the results presented in this study, the appropriate carrier frequencies for an in-situ Li-ion PLC network with consideration of the SoC of the Li-ion cell, can be established. Firstly, the frequency range from 50 MHz to 400 MHz displays little variation in S21 magnitude and phase shift with SoC of 0.1 dB and 1.7°, respectively, and also relatively little variation in the phase and S21 magnitude of the full experimental setup. This variation in S21 magnitude and phase shift increases marginally up to 800 MHz, whereas significant changes in EVM begin to occur at 600 MHz with multiple peaks present up to 1050 MHz. In addition, for frequencies between 1133 MHz and 1652 MHz, the difference in S21 magnitude and phase shift between SoCs is insignificant, remaining at less than 0.2 dB and 4.8°, respectively. Further carrier frequencies of recommendation include the range from 3300 MHz to 4000 MHz, which illustrates low variation in S21 magnitude and phase shift of the Li-ion cell with SoC of a maximum of 0.4 dB and –11.6°, respectively. At 5500 MHz, the S21 magnitude is at its lowest of –20 dB, with the phase also showing erratic changes at the same frequency. These results show an increased multipath fading effect at this frequency. Furthermore, the communication channel properties are also shown to change with SoC at this frequency, highlighting that the communication channel is particularly sensitive to changes in cell characteristics with SoC. Hence, the frequency of 5500 MHz must be avoided.

Because of commonly used normalisation and phase compensation techniques already established within QAM demodulation, it is unlikely that an increase in QAM order will have a negative effect on the PLC system's performance in this particular communication system. Nevertheless, the limitations of the QAM signal filtering must be considered before increasing QAM order. The presented BER and SER data show that the VST is unable to correctly phase compensate a 1024-QAM symbol trace. It is therefore appropriate to select a lower modulation order QAM to ensure a higher immunity to external factors, such as noise.

5.3 Conclusions

In this chapter, the changing characteristics of an 18650-model lithium-ion cell with varying state of charge (SoC) as an in-situ power line communication (PLC) channel have been identified. The performance of the in-situ Li-ion PLC system has been validated for SoCs of 5 %, 20 %, 40 %, 60 %, 80 % and 95 % and for the entire communication channel, by conducting communication tests with data modulated with quadrature amplitude modulation (QAM) in orders of 4, 16, 32, 64, 128, 256, 512, and 1024-QAM for high throughput communication.

These experiments reveal that reduced transmission power results in an increase in error vector magnitude. Consequently, selecting a lower modulation order of QAM is necessary for enhanced tolerance to changes in Li-ion cell characteristics with SoC and to external factors such as noise.

It has been shown that the SoC of the Li-ion cell has an impact on the PLC channel characteristics of the transmission coefficient's S21 magnitude and phase. These changes in SoC strongly depend on the used carrier frequency. In fact, it was found that the Li-ion cell at 5 % SoC had the most significant negative impact on both the S21 magnitude and phase, occurring at 1165 MHz, 3015 MHz and 5450 MHz. At these frequencies significant changes in both S21 magnitude and phase shift are observed, reaching maxima of 2.4 dB and 19.9° with respect to the baseline, respectively. Despite the strong correlation with the change in SoC and the carrier frequency, it has also been shown that the fixed characteristics of the Li-ion have a more profound effect on the communication channel, which varies greatly with carrier frequency. However, the only errors in BER and SER are due to the change in cell SoC, showing that the cell SoC must be taken into account when designing an in-situ battery PLC system. Based upon empirical evidence presented within this chapter, it can be concluded that the most appropriate parameters for an in-situ Li-ion PLC system that utilises QAM should be selected as follows: the selection of a carrier frequency between 50 MHz to 400 MHz, 1133 MHz to 1652 MHz, or 3300 MHz to 4000 MHz; using a maximum modulation order of 512-QAM; and the use of normalisation and phase compensation within the QAM demodulator.

The changes in S21 magnitude and phase with carrier frequency and with cell SoC are due to changes in the characteristics of the communication channel, whereby

the impedance of the Li-ion cell changes with both SoC and carrier frequency, as demonstrated in this chapter. These changes in impedance (and hence reactance and resistance) of the communication channel may cause constructive and destructive signal interference due to multipath fading, which has been addressed in Section 2.7.

The effects of multiple cells within a battery is presented in Chapter 6, which will determine the significance of the addition of cells in series and parallel on the communication channel and whether a correlation exists between the battery configuration and the characteristics of the communication channel.

Chapter 6

Effects of Lithium-Ion Battery Configuration on QAM-based Power Line Communication

In Chapter 5, the effects of state of charge (SoC) on an in-situ lithium-ion (Li-ion) cell power line communication (PLC) system were analysed to evaluate the performance of the communication system as the energy storage system is charged or discharged. Such analysis is useful to determine the effects of the changing Li-ion cell characteristics when used within a battery electric vehicle (BEV) or a smart grid energy storage system, where cell cycling is the norm. Such energy storage systems are considered large-scale due to the number of battery cells that they are comprised of. These large-scale energy storage systems may be configured in various ways to change their output voltage and current. Online battery reconfiguration may be employed to dynamically alter these parameters as needed by the system. As presented in Chapter 1, the ability for real-time coordination features, such as battery reconfiguration, can improve battery performance and safety. A potential example of a safety feature enabled by this smart technology is the ability to disconnect faulty cells or cells of poor health from the battery as soon as faults are detected to mitigate a cascade of dangerous events, such as thermal runaway and explosion. Hence, this research presents a PLC system that allows for coordination features to become achievable within large-scale energy storage systems without adding complexity or weight. Each smart cell within this

next-generation battery pack consists of an embedded processing system that utilises a PLC peripheral for communication with other smart cells. As such, the next stage of this research is to determine the effects of battery configuration on the performance of an in-situ Li-ion cell PLC system.

In this chapter the effects of Li-ion battery configuration on an in-situ PLC system are evaluated for carrier frequencies of 10 MHz to 6 GHz. Similarly to the experimental method described in Chapter 5, a vector network analyser (VNA) and vector signal transceiver (VST) are used to perform communication channel analysis using S21 scattering parameter measurements and actual data transfer tests using PLC with quadrature amplitude modulation (QAM). Such analysis is performed on 18650-model Li-ion battery configurations of single cell, two cells in series (2S), two cells in parallel (2P), and two cells in series and parallel (2S2P). These distinct configurations form a baseline with which larger configurations, such as those seen in common BEVs as shown in Table 2.3, are based upon. Performing this research on small battery configurations as opposed to large-scale battery systems is advantageous for the following reasons:

- Existing battery systems have not been designed for use with in-situ PLC. As such, the design of the batteries, such as the connections between the cells and to the bus bar, have not been characterised in the context of wired and high frequency communication. Hence, it is practically impossible to accurately determine whether changes in in-situ PLC performance and battery impedance are due to the Li-ion cells, the configuration of Li-ion cells, and/or due to the connections of the cells and the battery bus bar. In this research, the bespoke shunt-through configurable cell holder presented in Section 3.4.2 is designed to reduce the effects of the connections between the cells within the battery configuration and to the measurement devices in order to focus on how the configuration of cells and the cells themselves affect the impedance of the communication channel and the performance of the PLC system. This bespoke cell holder uses features such as high frequency SMA connectors and careful PCB routing to reduce the effects of the cell holder on the measurements. In contrast, existing battery systems do not have such features that benefit high frequency communication. This configurable shunt-through cell holder is used

within these experiments for ease of battery reconfiguration without necessitating the removal of cells from the circuit or requiring re-calibration between measurements.

- The small battery configurations characterised in this research can be used to derive the characteristics of large-scale battery systems and future smart battery systems. Performing such characterisation on a specific large-scale battery does not yield the same benefits, as it would not be clear how further changes to the battery configuration cause changes to the characteristics that affect the in-situ PLC system.

- This research performs measurements of four distinct battery configurations that are within the ±10 V rating of the measurement equipment for battery impedance and communication quality, and the results of this research can be used to determine the expected PLC performance of a large-scale battery and to make requirements on communication parameters and the most suitable battery configuration.

Each Li-ion cell is charged to an SoC of 95 %, to allow for comparisons with the 95 % baseline in the investigation of the effects of SoC on the communication channel in Chapter 5.

Comparisons of error vector magnitude (EVM), symbol error ratio (SER), and bit error ratio (BER) between battery configurations are used to determine the effects of battery configuration on the PLC system. Further comparisons with the S21 forward transmission coefficient of the communication channel are made to determine the expected communication performance of the battery configurations tested. Using this analysis, predictions can be made about the communication performance of the PLC system based upon the battery configuration and the S21 magnitude measured. The analysis of the changes in S21 magnitude and PLC performance through a Li-ion battery of various cell configurations, up to high carrier frequencies of 6 GHz, is a main contribution to the research community.

Overall, this method enables an evaluation of the limitations within the communication system, and recommendations are made on the parameters of such a PLC system as well as on the design of a large-scale battery pack. This research benefits

the BEV and the smart grid as it allows for smarter energy management using direct PLC between the smart cells within the BEV battery pack directly to the smart grid. This technique in turn grants remote online diagnostics of specific cells, improved safety and performance of the smart battery, and optimal utilisation of the BEV when attached to the smart grid.

The key contributions of this work are as follows:

1. Carrier frequencies of 10 MHz to 6 GHz are investigated in scattering parameter (S-parameter) measurements and real PLC testing with QAM up to orders of 1024, to evaluate their effectiveness of noise rejection and data rate with battery configurations of single cell, two cells in series (2S), two cells in parallel (2P) and a four cell configuration of two cells in parallel and in series (2S2P).

2. A configurable cell holder for 18650-model Li-ion cells is designed to allow for ease of reconfiguration without the removal of the cell from the circuit or requiring re-calibration between measurements.

3. An analysis is provided on the relationships between PLC performance, S-parameter magnitude, and battery configuration, and how the expected data rate may be determined based on these relationships.

4. Recommendations on parameters are made for prospective in-situ PLC systems based upon empirical evidence, such as appropriate carrier frequencies and PLC orders.

The results indicate that the addition of cells in parallel increases error ratios with high-order QAM, and that this effect changes substantially with carrier frequency.

6.1 Experimental Details

The Rohde & Schwarz (R&S) ZNA43 VNA is used to perform scattering parameters measurements of the Li-ion battery configuration as a PLC channel, which enables determining impedance and insertion loss. Further details on how a VNA is utilised to derive the performance of PLC are given in Chapter 3. In this chapter, the S21 magnitudes are presented to demonstrate the changes in PLC channel performance with

carrier frequency and battery configuration. Hence, the changes in S21 magnitude of the cell affect the performance of PLC communication. The VNA is configured to perform S21 measurements for frequencies of 10 MHz to 6 GHz with a step of 100 kHz, and is 'One-Path Two-Port' calibrated using the R&S ZN-Z129 calibration kit with a single cell holder for the same frequencies, simplifying the comparison between the cell configurations. These measurements are performed 20 times for each configuration and are then averaged to reduce the effects of outliers, noise, and interference.

The NI PXIe-5840 vector signal transceiver VST is used to perform real PLC testing of the battery with QAM orders of 4, 16, 32, 64, 128, 256, 512, and 1024-QAM. As described in Chapter 3, the VST is configured to transmit 100,000 QAM symbols with a symbol rate of 100 kHz at carrier frequencies of 10 MHz to 6 GHz with a step of 50 MHz. These QAM symbols include pilot symbols required for the VST to perform the synchronisation used by QAM demodulation, as explained in Section 2.10. The step size used with the VST is higher than that configured with the VNA due to experimental time considerations. The modulated signal is transmitted across the battery with an output power of –9 dBm or –27 dBm. The signal received on the VST input is demodulated into QAM symbols and further into bits of data. The QAM symbols are compared to a reference QAM constellation to obtain the root mean square (RMS) EVM. The decoded bits of data received are compared with the transmitted data to obtain the BER and the SER. Since 100,000 QAM symbols are transmitted in this experiment, the theoretical minimum achievable SER is 1×10^{-5}.

Each Li-ion cell is clamped within a bespoke shunt-through configurable cell holder as shown in Figure 3.9, and is connected to the VST and VNA as shown in Figure 6.1 and Figure 6.2, respectively. This cell holder has been designed to simplify its connection with other cell holders, making cell reconfiguration easier. As discussed in Section 3.4, the design of the cell holder minimises the effect of electromagnetic interference (EMI) on the signal, which includes using short traces and via stitching on the ground plane.

The shunt-through configuration is used because of its increased accuracy in measuring low-ohmic impedances [139]. In the employed shunt-through configuration, the negative terminal of the Li-ion cell is connected to ground. It is therefore expected that a decrease in internal resistance of the Li-ion cell will increase the attenuation of the

Figure 6.1: Cell holders connected in 2P shunt-through configuration to the VST.

signal. Both the VNA and the VST are connected to the battery in shunt-through configuration via SubMiniature version A (SMA) coaxial cables rated for frequencies up to 18 GHz. Figure 6.3 shows a circuit representation of the shunt-through configurations used in this experiment.

To further reduce the effects of EMI, this experiment is conducted within the same anechoic chamber used in Chapter 5. All of the Li-ion cells used in this research are NCR18650BD-model, and have the same SoC of 95 % and the same state of health (SoH). Due to manufacturing inaccuracies, each Li-ion cell will have slightly varying impedance characteristics, even within the same batch and model. Furthermore, where the VNA is calibrated with a single cell holder, further additional cell holders to form larger battery configurations will cause additional changes in S21 magnitude and phase delay. In this experiment, both the effects of the cells and their configurations on the PLC channel as well as the effects caused by the battery bus bar are of interest. It is important to consider that each battery pack model manufacturer may have different designs, including the shape and size of the bus bar, the type and quality

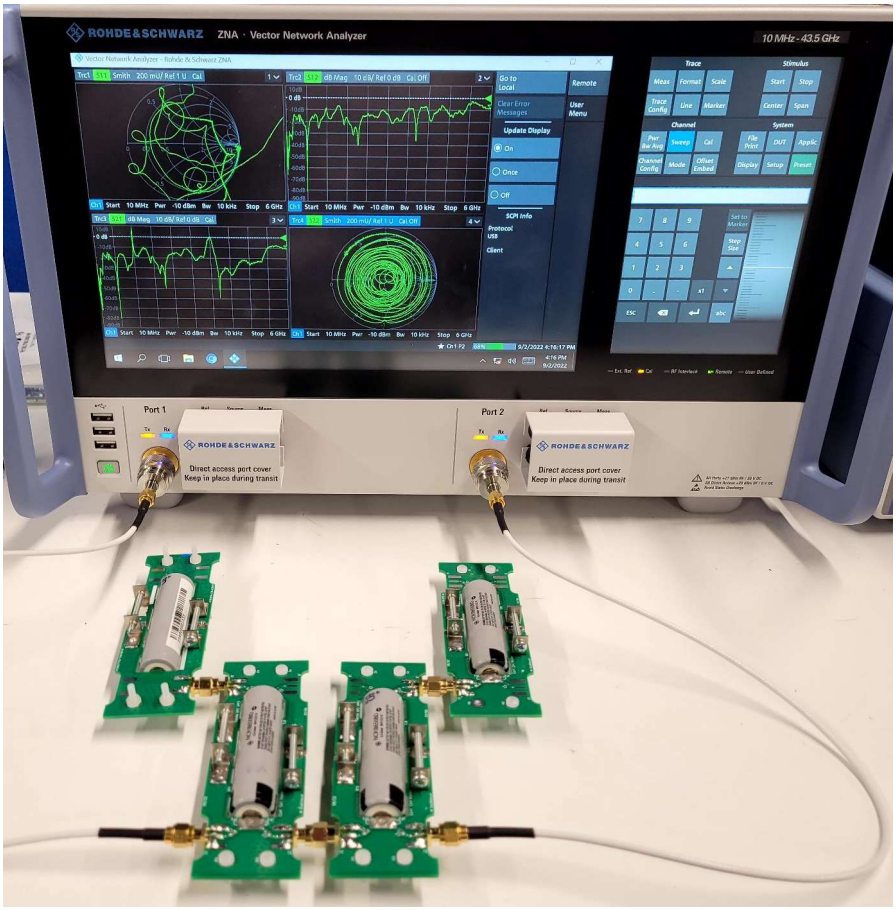

Figure 6.2: Cell holders connected in 2S2P shunt-through configuration to the VNA.

of the cell connections to the power bus, and the cell model used. Hence, in this work, a single calibration is used for all four investigated battery configurations, not correcting for additional scattering from interconnections between individual cell holders. As already stated, using a single calibration profile provides a straightforward comparison between the battery configurations tested.

As the wavelengths associated to the frequency range of 10 MHz to 6000 MHz approach the dimensions from the Li-ion cell and holder, in a first step it is verified to what extent RF power is radiated by them. For this test inside an anechoic chamber, an Electro-Metrics EM-6116 omni-directional antenna is placed 50 cm away from and oriented in parallel to a Li-ion cell that is clamped within the cell holder and connected to the VST. In addition, RF absorber tiles are placed around the antenna and cell to

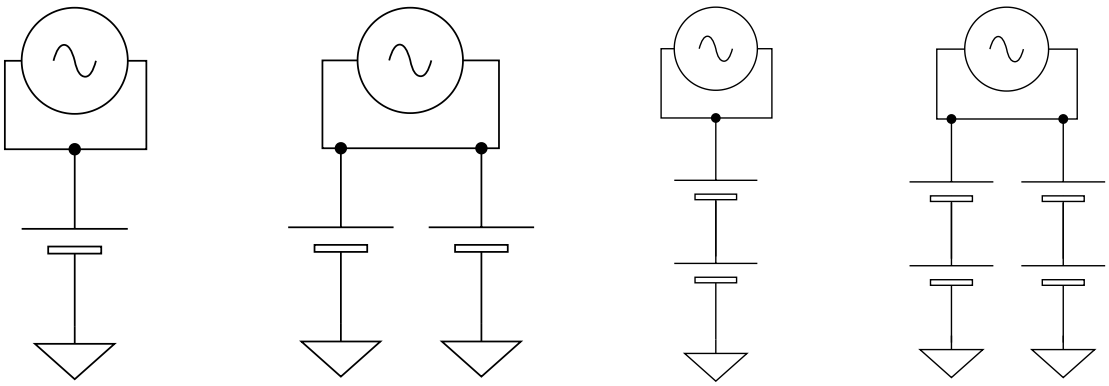

(a) Single Cell (b) 2P (c) 2S (d) 2S2P

Figure 6.3: Circuit diagrams of shunt-through cell holder connections for each Li-ion cell configuration of: (a) Single Cell; (b) 2P; (c) 2S; and, (d) 2S2P.

prevent reflected power from the setup itself affecting the results. The frequency range from 2 GHz to 6 GHz is investigated for radiated emissions, with the EM-6116 having a typical gain of 1.1 dB to 2.3 dB. The cell is placed 50 cm from the antenna to be in its far-field region. The antenna is connected to a R&S FSVA3000 signal and spectrum analyser, which is configured to perform 20 sweeps in a frequency step of 250 MHz, with the maximum power measured to be recorded. The VST is configured to continuously transmit the same stream of 16-QAM symbols used in the main experiment of testing various battery configurations at an output power of –27 dBm, as already described. Table 6.1 shows the maximum power measured by the spectrum analyser for each frequency tested. In each spectrum only the selected VST carrier frequency can be observed and any possible harmonics or other signals are below the VNA's noise level of approximately –87 dBm.

In addition to this test, the orientation of the cell holder is changed twice such that it is perpendicular, and then upright, to the antenna. For the frequency of 3.25 GHz, which results in the highest recorded power radiated in the parallel arrangement, the measured power is –72.84 dBm and –78.24 dBm for perpendicular and upright orientations, respectively.

Taking into account the optimal alignment, the antenna distance, the EM-6116 antenna gain, and assuming a hypothetical transmitting antenna gain of 0 dB for the

Frequency (GHz)	Received Power (dBm)	FSPL (dB)	Excess Loss (dB)
2	-80.8	31.1	22.7
2.25	-79.5	32.2	20.4
2.5	-83.6	33.1	23.5
2.75	-83.9	34.0	22.9
3	-78.3	34.8	16.5
3.25	-75.0*	34.9	13.1
3.5	-79.9	35.0	17.9
3.75	-77.0	35.7	14.3
4	-76.1	36.4	12.7
4.25	-82.2	36.8	18.4
4.5	-83.4	37.2	19.2
4.75	-90.1	38.0	25.2
5	-83.6	38.7	17.9
5.25	-86.1	38.9	20.1
5.5	-87.0	39.1	20.9
5.75	-87.0	39.7	20.3
6	-85.0	40.2	17.8

Table 6.1: Maximum power radiated by the Li-ion cell and cell holder when it is placed parallel to the antenna. The highest power measured is marked with *. In addition, the calculated free-space path loss and excess loss related to the measurement conditions are presented.

Li-ion cell, the expected free-space path loss (FSPL) can be calculated using

$$\text{FSPL} = 20\log_{10}(d) + 20\log_{10}(f) + 20\log_{10}\left(\frac{4\pi}{c}\right) - G_{Tx} - G_{Rx} \tag{6.1}$$

and are provided in Table 6.1, where d is the distance between the antenna and the Li-ion cell, f is the frequency, c is the speed of light, G_{Tx} is the transmitter (the Li-ion cell) gain and is assumed to be 0, and G_{Rx} is the receiver gain of which the values are obtained from the antenna data sheet. Comparing these values with the differences between the output power of the VST and the received power levels of the VNA for each selected frequency, the excess loss can be determined, which represents the power fraction that is radiated by the Li-ion cell clamped within the cell holder. These tests have thus demonstrated that for all investigated frequencies, the majority of the power is transmitted through the Li-ion cell and not radiated by it.

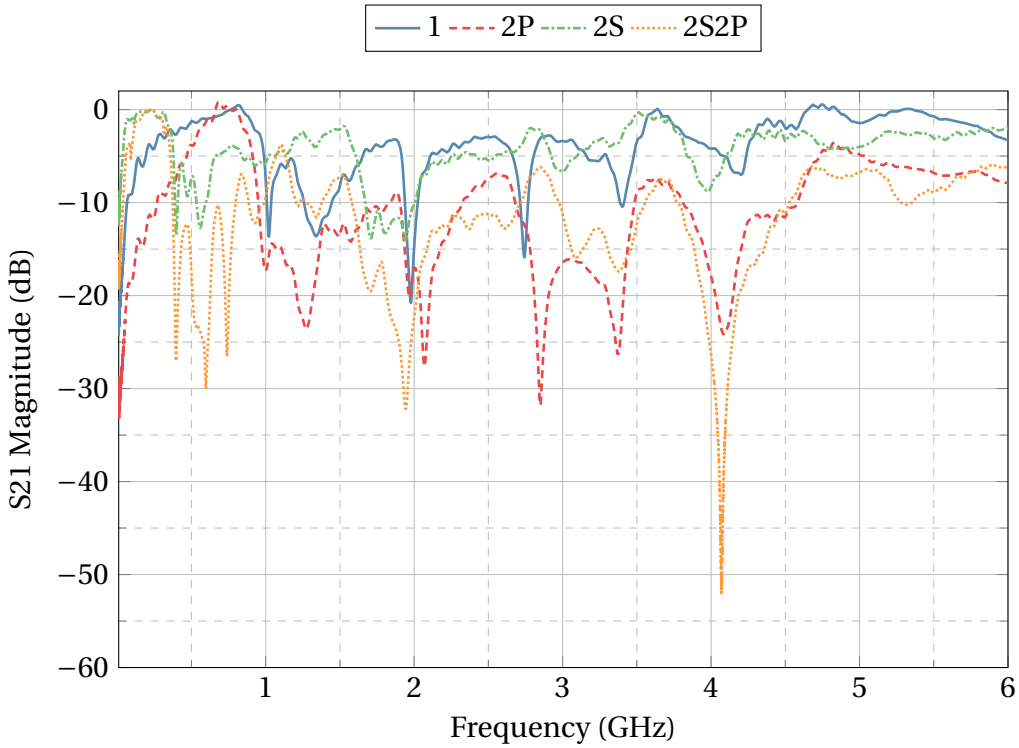

Figure 6.4: S21 magnitude of four different battery configurations.

6.2 Results and Discussions

This section presents the results of the experimentation described in Section 6.1 and discusses the changes in PLC performance with battery configuration.

Using the S21 magnitude and phase shift data of the 20 sweeps performed, and by taking into account the standard deviation within such single set of measurements and the reproducibility in clamping the cells within the cell holders, the achieved error margins are ±0.1 dB and ±1.0°, respectively.

6.2.1 S21 Magnitude Analysis

The S21 magnitude of the four battery configurations tested are shown in Figure 6.4. It can be seen that both the carrier frequency and the battery configuration have a significant impact on the S21 magnitude. However, the battery configurations tested yield similar characteristics, such as peaks in S21 magnitude at the same frequencies.

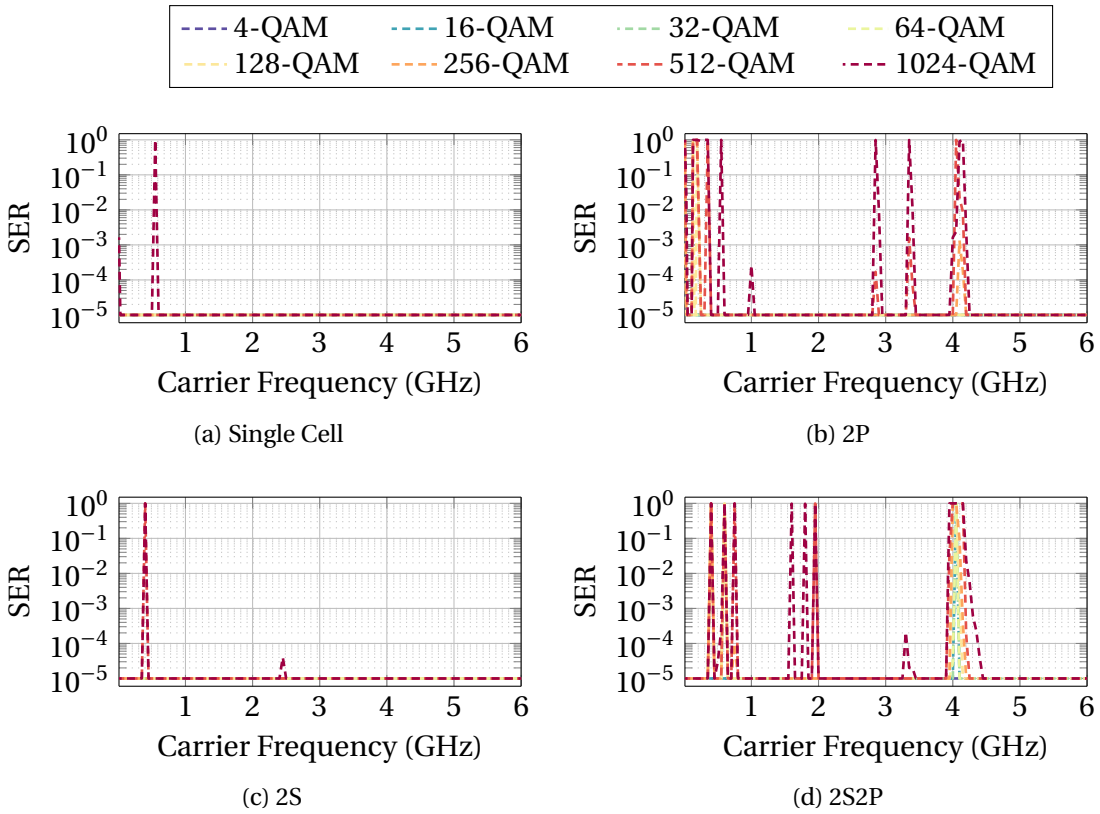

(a) Single Cell

(b) 2P

(c) 2S

(d) 2S2P

Figure 6.5: SER of PLC at –27 dBm through Li-ion cell configurations of: (a) Single Cell; (b) 2P; (c) 2S; and, (d) 2S2P.

Further discussion on these similarities and how they may have been caused are now presented.

At 10 MHz, the S21 magnitudes for all battery configurations begin with varying levels of attenuation of –19 dB, –33 dB, –12 dB and –20 dB for single cell, 2P, 2S and 2S2P battery configurations, respectively. This result indicates attenuation of the signal through the communication channel, which is contrary to the results of the changes with SoC presented in Chapter 5. This is because in Chapter 5, a series-through cell holder was utilised to transmit data through the Li-ion cell, whereas this experimental work uses a shunt-through cell holder design which transmits data across the positive terminals of the cells, as if the data was being communicated over a bus bar. Hence, at 10 MHz, the resistance of the Li-ion cells are so low that the signal transmitted across the battery is being significantly attenuated. This is further

demonstrated with the 2P configuration, which shows the greatest signal attenuation of all the configurations tested, since the effective resistance of the communication channel is approximately halved in comparison to a single cell configuration. On the other hand, the 2S and 2S2P configurations shows the least attenuation at 10 MHz due to the increase in the resistance of the configuration due to the series arrangement of the cells. It can therefore be deduced that the addition of cells in parallel will increase the attenuation effect of the PLC signal, whereas a series configuration may reduce this effect. As it will be described later in this section, this behaviour depends on the carrier frequency. From 10 MHz, a minor trend can be seen whereby the single cell and 2P battery configurations show similar properties, as well as 2S and 2S2P. In fact, the S21 magnitudes for both 2S and 2S2P rise close to 0 dB by 200 MHz, indicating little to no loss in signal power and therefore a very good communication channel using this carrier frequency. On the other hand, the S21 magnitudes for both single cell and 2P rise at a slower rate, and eventually tend close to 0 dB at 650 MHz. At this frequency however, 2S and 2S2P display large reductions in signal power of up to –30 dB, indicating that a change in battery configuration, such as from 1S to 2S for example, will negatively impact the PLC system at 597 MHz. This change in the signal power between battery configuration indicates that this frequency is unsuitable for the smart battery technique of battery reconfiguration unless significant signal conditioning is introduced.

The S21 magnitudes for 2S and 2S2P diverge at 300 MHz, with 2S falling to a minimum of –13 dB at 398 MHz, whereas 2S2P falls much further to a minimum of –27 dB at 396 MHz. Such behaviour may be attributed to differences in multipath fading, whereby an increased destructive interference is seen to occur with the 2S2P configuration in comparison to the 2S configuration at these frequencies. A further two minima occur with both of these battery configurations, whereby 2S shows two small peaks of –9 dB and –13 dB at 474 MHz and 555 MHz, respectively, and 2S2P shows two large peaks of –30 dB and –26 dB at 597 MHz and 739 MHz, respectively. It can be seen that the 2S2P battery configuration is having the most profound effect on the S21 magnitude from 369 MHz to 955 MHz, where the destructive interference, which causes signal attenuation, becomes even more significant. Within this range of carrier frequencies, it is expected that the effect of noise, as in a decrease in signal

to noise ratio (SNR), on the communication channel will become more significant. In Section 6.2.2, it will be shown that certain S21 thresholds exist above which the investigated communication channels are capable of successful transmission of a PLC signal with a certain QAM order through these battery configurations tested.

The minor trend of similar properties between 2S and 2S2P, and also with single cell and 2P, which seemingly occur due to their high and low resistances, respectively, ceases at 955 MHz. Instead, the S21 magnitude for 2S2P and single cell begin to show similarities, whereby another local minimum can be seen at 1338 MHz of –12 dB and –14 dB, respectively. It may be concluded that the impact of the addition of cells in the battery configuration on the performance of the communication channel is reduced at this frequency, since the difference in S21 magnitude compared to the single cell is minimal. In addition, at this frequency, a slight peak can also be observed for 2S with an S21 magnitude of –4 dB, which exhibits the least signal attenuation in this comparison. In contrast, 2P displays a similar peak at 1277 MHz, but with the greatest attenuation and an S21 magnitude of –24 dB. This observation aligns with the fact that arranging the cells in series increases the resistance of the signal path to ground and therefore reduces attenuation, whereas the addition of cells in parallel reduces this resistance, hence increasing signal attenuation.

Starting from 1530 MHz, the S21 magnitude of both 2S and 2S2P battery configurations fall from –2 dB and –7 dB to –14 dB and –32 dB at 1943 MHz. It is also shown that these two battery configurations have a similar trend for the rates at which their S21 magnitudes decrease, and that such trend indicates an increased significance of the destructive interference caused by the multipath effect. Furthermore, the S21 magnitudes of the single cell and 2P configuration continue to rise until 1883 MHz, where a much sharper peak then occurs with a minimum S21 magnitude of –21 dB and –20 dB, respectively. After this peak, the S21 magnitudes of all battery configurations rise and eventually settle at 2570 MHz with S21 magnitudes of –3 dB, –7 dB, –5 dB and –12 dB for the single cell, 2P, 2S and 2S2P battery configurations, respectively. This improvement in S21 magnitude suggests that the multipath effect still occurs, but the timing of the signals at the receiver may be such that a constructive interference is occurring at this carrier frequency. Various factors, such as the length, connections and material of the bus bar may change the magnitude of this effect at

various carrier frequencies. Between the frequencies of 2200 MHz to 2700 MHz, the high S21 magnitude indicates a favourable PLC channel with minimal signal loss, suggesting adequate communication quality and reliable data transmission with these battery configurations. This channel allows for a bandwidth of 500 MHz. Despite this fact, it can be clearly seen that the addition of Li-ion cells in parallel reduces the S21 magnitude, thereby indicating that adding further cells to the battery configuration will cause signal attenuation and potentially poor performance and reduced data reliability. It is expected that as the number of cells within the battery configuration increases, the number of signal conditioning utilities, such as signal repeaters, will be added into the communication network. However, the signal output power and/or the number of signal repeaters can be reduced by selecting a bandwidth with a high S21 magnitude as indicated in these battery configuration tests presented here. The performance of this bandwidth is later verified in Section 6.2.2.

Between 2700 MHz and 2900 MHz, a minimum peak occurs in both single cell and 2P battery configurations, whereas a maximum peak occurs in both 2S and 2S2P battery configurations. These peaks illustrate the minor trends due to multipath fading as already stated, whereby single cell and 2P, and 2S and 2S2P battery configurations demonstrate similar properties.

After the local maximum in 2S and 2S2P battery configurations, a minimum occurs at 3001 MHz and 3091 MHz with S21 magnitudes of –7 dB and –16 dB, respectively. The S21 magnitude for the 2S battery configuration gradually rises after this peak. However, the single cell, 2P and 2S2P battery configurations all have a minimum peak at 3398 MHz, 3373 MHz and 3385 MHz with S21 magnitudes of –10 dB, –26 dB and –17 dB, respectively. This phenomenon shows a deviation in the minor trend of properties between the 2S and 2S2P battery configurations, whereby 2P and 2S2P now have increased their likeliness until 6000 MHz. This suggests that arranging the cells in parallel has a dominant effect on the S21 magnitude compared to arranging the cell in series. At 3640 MHz, a local maximum can be seen in all battery configurations, with S21 magnitudes of 0 dB, –7 dB, –1 dB and –8 dB for single cell, 2P, 2S and 2S2P, respectively, again highlighting a very good communication channel for all battery configurations. At this frequency, it is expected that the addition of cells in parallel and series will have the least effect on the S21 magnitude, and hence the PLC performance,

in comparison to all the other frequencies tested. However, the addition of cells in parallel clearly has a negative effect on the S21 magnitude in comparison to the addition of cells in series. Therefore, increasing the number of cells in parallel, even at 3640 MHz where the change in S21 magnitude between battery configuration is lowest, may still have a detrimental effect on the PLC system. As it will be stated later, these results can be used to deduce the signal filtering required in order to mitigate the effects of the addition of cells in parallel, which is inevitable in BEV energy storage systems. The S21 magnitudes then decrease, with 2S2P decreasing very sharply and displaying the greatest attenuation for all frequencies tested at 4070 MHz with an S21 magnitude of –52 dB. This low S21 magnitude indicates significant attenuation at this frequency, hence it is most unsuitable for a PLC system as a signal repeater would be required for each additional 2S2P configuration within the battery, thereby increasing complexity, weight and cost of the smart communication system. In addition, at this frequency of 4070 MHz, a large peak also occurs for 2P with an S21 magnitude of –24 dB. After these peaks, the S21 magnitudes all rise above –10 dB and remain nearly frequency-independent, hence improving their suitability as a PLC system. Between 4450 MHz to 6000 MHz, the S21 magnitude for all battery configurations indicates that due to low signal attenuation on the communication channel, the number of signal repeaters required within the battery system can be reduced, in comparison with other frequencies, such as 4070 MHz, which shows very low S21 magnitude. This range in high S21 magnitude for frequencies of 4450 MHz to 6000 MHz allows for a bandwidth of 1550 MHz. By designing the in-situ battery PLC system to use this bandwidth, either through orthogonal frequency division multiplexing (OFDM) or as a wide-band single carrier, the signal conditioning required, such as the use of signal repeaters, can be minimised. This reduces the cost and complexity of integrating a PLC system within a battery.

6.2.2 Communication Error Analysis

The results of the SER and BER measurements demonstrate identical behaviour, hence the BER results are omitted for brevity and without loss of generality. Furthermore, the results for –27 dBm output power display greater errors than for –9 dBm, hence the focus of the following analysis is on the former results, i.e. –27 dBm.

Figure 6.5 presents the SER of the PLC system with the four battery configurations using an output power of –27 dBm. It is shown that similarly to the S21 magnitude, the SER changes with battery configuration, carrier frequency, and QAM order. As expected, where errors in SER occur, the highest QAM order of 1024-QAM exhibits the highest SER, whereas 4-QAM does not show a single symbol error for all carrier frequencies and battery configurations. Despite this behaviour, there are large carrier frequency ranges where the VST is able to decode all symbols correctly, even for 1024-QAM. Such carrier frequency ranges include 1050 MHz to 2800 MHz, and 4250 MHz to 6000 MHz for the 2P battery configuration. Similarly, the 2S2P battery configuration displays no symbol errors between ranges of 2000 MHz to 3250 MHz, and 4450 MHz to 6000 MHz. In contrast, the single cell and 2S battery configurations show very little occurrences of symbol error, with errors only in 1024-QAM at 10 MHz and 550 MHz for single cell, and in 1024-QAM and 512-QAM at 400 MHz and additionally in 1024-QAM at 2450 MHz for 2S. Crucially, these symbol errors correspond with instances where the S21 magnitude is most attenuated. For instance, at 400 MHz, the S21 magnitude for the 2S configuration is at a local minimum of –13 dB, which corresponds to the peak in SER with 1024-QAM at the same frequency. Furthermore, both 2P and 2S2P battery configurations demonstrate this trend in high SER with S21 magnitude attenuation. It is also shown that the peaks in S21 magnitude at 395 MHz, 597 MHz and 739 MHz of –27 dB, –30 dB and –26 dB correspond to sharp peaks in SER at 400 MHz, 600 MHz and 750 MHz, with an SER of 1 for 1024 and 512-QAM for all three peaks, and an SER of 1 for 256, 128, 64, and 32-QAM for the first of these two peaks, respectively. The greatest attenuation in S21 magnitude with 2S2P at 4070 MHz of –52 dB also demonstrates the greatest SER at the same frequency. In fact, the SER of 1024-QAM sharply rises to an SER of 1 at 3950 MHz, and only decreases from 4150 MHz onwards to a minimum SER at 4450 MHz. At 4050 MHz, only 4-QAM does not have an SER of 1, which continues to remain at the lowest SER.

This communication analysis indicates that there is a strong correlation with S21 magnitude attenuation and SER. Moreover, it can be seen that the addition of cells in parallel significantly reduces the S21 magnitude, which causes signal attenuation and an increase in SER. This increase in SER is most pronounced in higher modulation orders of QAM, which require a higher signal to noise ratio in order to function cor-

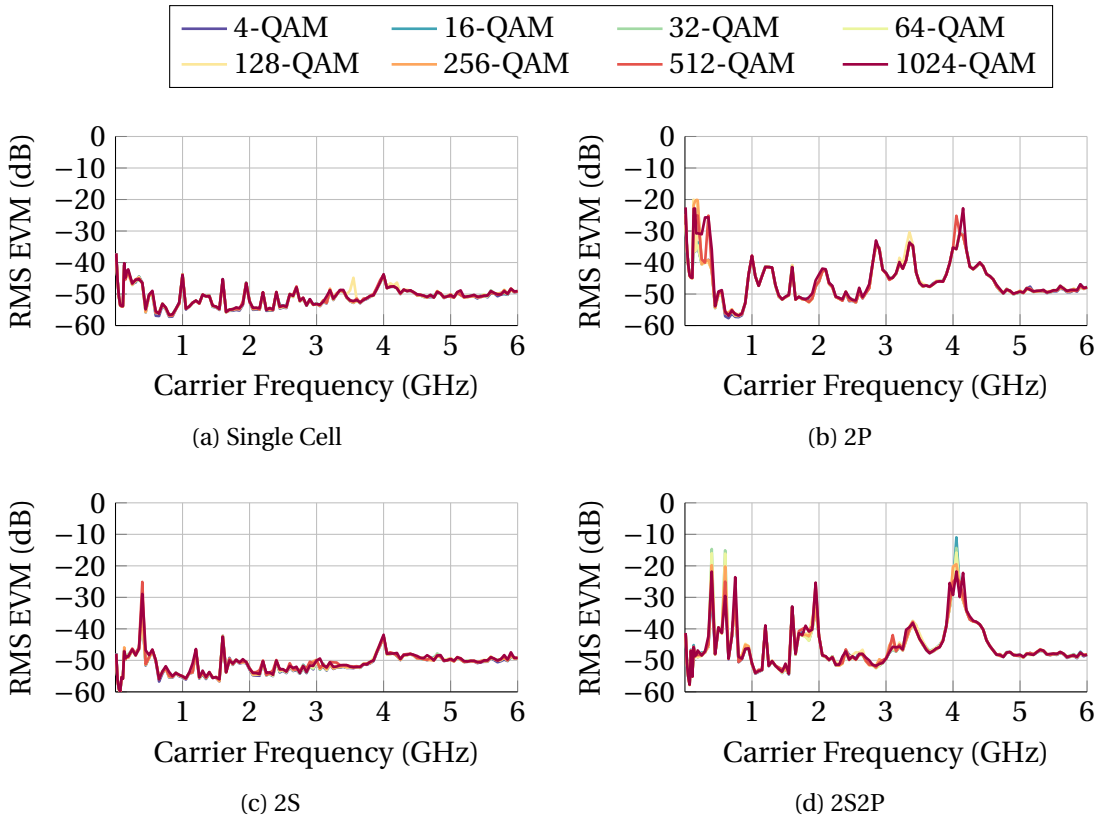

(a) Single Cell

(b) 2P

(c) 2S

(d) 2S2P

Figure 6.6: RMS EVM of PLC at –27 dBm through Li-ion cell configurations of: (a) Single Cell; (b) 2P; (c) 2S; and, (d) 2S2P.

rectly without error. Further evidence of these trends are observed in the RMS EVM measurements presented in Figure 6.6 whereby rises in RMS EVM correlate with rises in SER. The largest attenuation in S21 magnitude with the 2S2P battery configuration at 4070 MHz corresponds with the high RMS EVM at 4050 MHz of –11 dB for 16-QAM. At the same frequency, the 2P battery configuration reaches a high RMS EVM of –23 dB, whereas 2S and single cell show a low RMS EVM of –42 dB and –44 dB, respectively.

For a VST output power of –27 dBm, the thresholds of S21 magnitude below which symbol errors begin to occur for QAM orders of 16, 32, 64, 128, 256, 512 and 1024 are –30 dB, –27 dB, –26 dB, –25 dB, –24 dB, –21 dB and –16 dB, respectively. At this output power, no symbol error occurred for 4-QAM. This highlights the trend, that with decreasing QAM order, the threshold in S21 magnitude to symbol error continues to increase as well. Using these relationships between S21 magnitude, RMS EVM and

SER, it is possible to estimate both the SER and RMS EVM based upon measurements of the S21 magnitude of a cell configuration, allowing for a much simpler verification procedure during the early design stage of a smart cell system.

In addition to EVM, the SNR is another crucial metric for evaluating signal quality. As explained in Section 2.11, SNR quantifies the ratio of signal power to noise power, influencing the overall robustness of transmission and its susceptibility to noise-induced errors. On the other hand, EVM measures the accuracy of received signals compared to expected data by considering phase and amplitude errors, which is indicative of transmission distortion. Whereas SNR and EVM offer distinct insights into signal quality, they are not directly interchangeable as a high SNR does not necessarily guarantee low EVM and vice versa. This fact may be due to signal conditioning techniques that can be utilised by the communication system to mitigate the effects of high noise, and therefore the effects of low SNR, on data transmission. Hence, both metrics are essential for assessing different aspects of signal fidelity and reception quality in communication systems. Despite this fact, the SNR was not under investigation within this experimental work as it is not an objective to determine the limitations of the signal conditioning utilised within the VST used. Instead, this experimental work determines the change in the quality of communication channel solely dependant on the configuration of the Li-ion cells and the carrier frequency, with a focus on keeping external factors, such as the SNR, constant. However, the effects of drive cycle noise within a simulated BEV battery system has been addressed in Chapter 4.

6.2.3 Recommendations

From the results of this work it can be deduced that the PLC performance is affected most by the 2P and 2S2P battery configurations, whereas the PLC performance of the 2S battery configuration is least affected compared to that of a single cell. This is most likely due to a reduction in the real resistance of the circuit under test, as the two cells in the 2P configuration act as two resistors in parallel. In contrast, placing two cells in series, and hence increasing the real resistance of the circuit, demonstrates slightly improved PLC performance. It is unlikely that the reactance of this circuit has a profound effect on the PLC performance due to the effectiveness of phase compensation processing found in common QAM demodulators, particularly when

the magnitude of the received signal is above a certain threshold. In addition to the changing resistance in the shunt configuration of the batteries tested, an impedance mismatch may be causing a multipath effect, whereby the signal propagates onto additional paths causing it to arrive at the receiver at different time intervals, as mentioned previously. These effects can cause data corruption and/or loss as measured with SER and RMS EVM in this research. The number of cells in parallel and series must therefore be taken into account when designing a battery pack, as increasing the number of cells in parallel will reduce the PLC performance and the achievable data rate, whereas a decrease will reduce the maximum rated current output of the battery pack.To mitigate this reduction in the PLC performance with the addition of Li-ion cells in the battery configuration, the following techniques can be utilised:

- The addition of cells placed in series should be prioritised over the number of cells in parallel due to the relatively lower impact on the performance of PLC.
- Increase the output power of the PLC signal to reduce the impact of attenuation caused by the communication channel.
- Adding signal repeaters in the communication system per number of cells. The selection of a frequency and bandwidth that has been demonstrated in this research to show the least attenuation in S21 magnitude, will require fewer signal repeaters than a bandwidth that has high attenuation in S21 magnitude.

Various trends in S21 magnitude between battery configurations have been identified which indicate that certain changes in battery configuration do not result in a significant change in S21 magnitude, thereby scarcely affecting the PLC performance in terms of SER. These trends change in strength with carrier frequency, and in the instance at 3373 MHz, the trend in single cell and 2P battery configuration weakens and changes in favour of the trend in the 2P and 2S2P configurations which remains strong up to 6000 MHz. In fact, at 3600 MHz, the similarity in S21 magnitude and SER between single cell and 2S, and also 2P and 2S2P, demonstrates that the addition of cells in series does not have any significant effect on the PLC channel. Hence, these measurements have highlighted that the addition of cells in series does not impact the expected data rate that could be achieved from PLC within a large-scale battery pack system.

In addition, it can be concluded that suitable carrier frequencies for all investigated battery configurations and QAM orders tested are within the range of 2200 MHz to 2700 MHz, 3500 MHz to 3800 MHz and 4450 MHz to 6000 MHz. Within these ranges, the achievable data rate of the PLC system is expected to be the highest. The range of suitable carrier frequencies may be increased by utilising a lower QAM order, but then the advantages in QAM data rate are also reduced. For large-scale battery systems with an increased number of cells in parallel configuration, signal conditioning techniques may be used to mitigate attenuation, which in turn may increase the cost and complexity of the communication system.

These recommendations are based upon the 18650-model Li-ion cell tested in this research. From existing literature, it can be found that the SoC, SoH, battery model, and battery chemistry have an effect on the S21 magnitude. It is therefore required that the presented experimentation is performed for each different battery design to consider PLC performance differences caused by these characteristics. These results can be validated by utilising impedance simulations of Li-ion cells to predict the PLC performance [1].

6.3 Conclusions

In this chapter, a PLC network within four battery configurations was evaluated for its effectiveness as a future smart battery communication system. The 18650-model Li-ion cells were used as a communication channel for in-situ PLC. This technique allows for future smart cells to communicate large amounts of embedded sensor data, such as core cell temperature, to other smart cells in the battery system and to an external battery management system (BMS), using the existing battery bus bar and without the addition of a wire harness which would increase the complexity, cost, and weight of the battery. The performance of a real large-scale Li-ion battery pack can be derived from the experimental results of the four battery configurations presented in this chapter. The use of QAM up to modulation orders of 1024 was analysed for its usability as a modern modulation scheme in this battery system, and is also the highest modulation order defined in the HomePlug AV standard.

This research has demonstrated that battery configuration, carrier frequency, and

QAM order, all affect the performance of this PLC system. Based on these results, recommendations for a future smart battery PLC network within BEV and smart grid environments have been proposed. Furthermore, the results display trends in the PLC performance with battery configuration, and that certain thresholds in S21 magnitude correspond to the occurrence of symbol errors. For instance, a high S21 magnitude of –16 dB indicates that 1024-QAM PLC is possible at a carrier frequency of 3650 MHz with a bandwidth of ~300 MHz and as such will exceed the physical layer data rate capabilities found in IEEE 1901, for example [171]. This research thus allows for future smart cells to communicate vast amounts of sensor data to the BMS and the smart grid using PLC on the bus bar for improved performance, safety, and energy management. Such sensor data communication within a smart battery system may include temperature, cell balancing, and cell reconfiguration data, as previously explained in Section 1.1.

The performance of large-scale battery systems can be determined using the methods used within this experimental work. In addition, an estimation as to the characteristics of large-scale battery systems may be made based upon the four distinct configurations tested within this research. These results demonstrate that whereas some carrier frequencies show significant S21 magnitude attenuation even with two cells in series (2S), other carrier frequencies do not. With these exemplary frequencies, such as 3600 MHz, the EVM and the SER also demonstrated good performance, and therefore a relationship with the measured S21 magnitude. This relationship allows for future designs of smart batteries to be verified for their in-situ battery PLC performance by only requiring a measurement of the communication channel S21 magnitude. With such measurements, an appropriate carrier frequency can be chosen based on the attenuation recorded in the S21 magnitude, but also the selection and magnitude of any signal filtering techniques, such as signal repeaters. Such signal filtering may be required when the number of cells within the communication system increases, which has been demonstrated in this experimental work by the fact that an increase of cells, such as from 2S to 2S2P, increased the attenuation of the S21 magnitude and also reduced the performance of the in-situ battery PLC system with some carrier frequencies that produced inferior communication performance. For instance, the carrier frequency of 4070 MHz demonstrated the highest SER with all orders of QAM

apart from the lowest modulation order tested of 4-QAM.

Chapter 7

Conclusions and Future Work

The use of power line communication (PLC) within lithium-ion (Li-ion) batteries has been investigated in this thesis for performance in both data rate and noise rejection within a system of smart cells for next-generation energy storage systems. Extensive simulations and laboratory experiments have demonstrated the feasibility of utilising a PLC system within large-scale Li-ion energy storage systems, such as for battery electric vehicles (BEVs) and smart grids. These applications stand to benefit from the PLC system presented, allowing for the improvement of battery performance, capacity, and safety, such as BEV driving distance on a single charge, or smart grid capabilities to smooth out fluctuations in energy demand. It has been shown that this system has the capability to withstand changes in the electrical characteristics of battery cells, ensuring reliable communication even under varying operating conditions. This chapter summarises the research motivations and highlights the novel contributions made to the research field within this thesis. Moreover, suggestions on future research opportunities on this topic are provided.

7.1 Conclusions

Li-ion cells are established as one of the most popular battery chemistries in use due to their high power and energy densities. However, the potential dangers of their use, such as thermal runaway caused by circuit overload, necessitates the need for a battery management system (BMS) to control the use of such cells. The BMS makes

measurements of the Li-ion cell voltage, discharge and charge current, and impedance, in order to deduce the cell state of charge (SoC) and state of health (SoH), and to perform tasks that improve safety, including cell balancing, over-voltage and over-current protections. Using general characterisation data of the Li-ion cell, the BMS makes assumptions as to the performance limitations of the cell, including the maximum capability of the cell to be used as a current source and sink for discharging and charging, respectively. Recent work has presented the idea of smart cells to improve the safety and performance of Li-ion cells by utilising smarter battery management systems, such as through the use of embedded sensors and computer systems within the Li-ion cell [40]. When using embedded sensors and cell instrumentation, the smart cell is able to obtain real-time characterisation data of the Li-ion cell it is embedded within, to use these data to determine accurate discharge and charge capabilities. Furthermore, these real-time data can be used with applications based on state-of-the-art research, such as constant-temperature constant-voltage (CT-CV) charging profiles [172], to further improve the charging speed of Li-ion cells. The effectiveness of the smart cell can be further enhanced through the use of a communication system to enable the coordination of smart cells as a system that allows for techniques such as online battery reconfiguration, cell disconnection, and fault diagnosis with external systems.

In this thesis a PLC system was selected for use within such an application as it does not require an additional wire harness within the battery. The challenges of using PLC within Li-ion batteries in order to create a smart and connected battery system capable of improving both safety and performance have now been addressed. In addition, the use of quadrature amplitude modulation (QAM) has been tested as a modern modulation scheme to increase data throughput. Chapter 1 has provided an introduction into the context and significance of the research and the key research contributions. Chapter 2 presented a thorough literature review on the various instrumentation and embedded technologies that are used within a Li-ion smart battery system. Based upon three key experimental studies, this thesis has presented the following novel contributions to the research community:

1. The ability to carry out accurate simulations of PLC with QAM communication performance through a Li-ion cell using existing electrochemical impedance

spectroscopy (EIS) characterisation data within the electrical environment of a driving BEV.

2. Understanding the changes in communication performance of PLC with QAM as the Li-ion cell's SoC is changed, such as due to charging or discharging, for carrier frequencies of up to 6 GHz.

3. Measuring the changes in communication performance of PLC with QAM in various Li-ion battery configurations, such as due to online reconfiguration of smart cells, or differences in battery architecture.

The experimental details pertaining to the three experimental works are presented in Chapter 3, where the use of the vector network analyser (VNA), vector signal transceiver (VST), and bespoke cell holders, have been described. It is shown that the VNA is used to perform S21 measurements of the Li-ion battery as a communication channel, and that the VST is used to perform real communication tests with QAM symbols transmitted through the Li-ion battery. In addition, the two bespoke cell holder designs used within this research were detailed, including their use in improving the accuracy of cell characterisation. The use of this equipment to perform such measurements with changing SoC and battery configuration is a novel contribution to the research field.

As a precursor to performing tests on a real Li-ion battery, Chapter 4 defined the use of existing Li-ion cell characterisation data to perform PLC performance simulations using the QAM scheme through two Li-ion cells in series and separately, two in parallel. In this work, it has been shown that the effects of noise from the BEV, which are mainly produced by the DC-DC converter, has no effect on the communication performance. However, a real BEV drive profile load, recorded as it was driven on a local motorway, was shown to have a significant effect on the performance of the PLC system due to substantial attenuation of the communication signal. In fact, the constant load profile of 1 Ω only showed minor improvement in communication error. This chapter concluded that such a PLC system within a BEV will require automatic gain control to compensate for significant signal attenuation, and also phase compensation to counteract the substantial phase shift caused by the characteristics of the Li-ion cells. In addition, it has been deduced that for the carrier frequencies tested of 100 kHz to

200 MHz, the frequency range of 13 MHz to 40 MHz, demonstrates the least change in phase shift and attenuation with carrier frequency, and is therefore most suitable for use in an in-situ Li-ion battery PLC system. This is in comparison to the existing HomePlug AV standard, which uses 1155 orthogonal frequency division multiplexing (OFDM) 24.414 kHz spaced subcarriers in a frequency range of 1.8 MHz to 30 MHz. For the frequency range of 13 MHz to 40 MHz it is possible to achieve 1105 OFDM subcarriers equally spaced at 24.414 kHz. In comparison to HomePlug AV which offers a maximum physical layer throughput of 200 Mbit/s, based on the results presented in this research, it is possible for an in-situ battery PLC system to offer a throughput of approximately 190 Mbit/s when the same modulation techniques, such as QAM order, are utilised. It has also been demonstrated that increasing the QAM order increases the communication error due to the decreased noise rejection performance of the communication channel. Hence, the throughput of the in-situ battery PLC system may be diminished due to the harsh nature of the in-situ battery communication channel. Despite this fact, modulation techniques used in newer standards, such as the use of multiple transmitters and receivers in the HomePlug AV2 and IEEE 1901 standards, can be used to increase the performance of PLC within this harsh environment. For instance, HomePlug AV2 can reach a maximum physical layer data rate of 2024 Mbit/s. Furthermore, whilst the simulations presented in this research has demonstrated the relatively harsh nature of the Li-ion cell as a communication channel, it is known that BEVs use energy storage systems that utilise many cells. The sheer number of cells will therefore have a significant impact on the performance of the in-situ PLC system. The effect of the number of cells and their configuration within the battery pack has been investigated in Chapter 6. In this harsh environment, the use of HomePlug Green PHY may be used instead, which offers low power, low cost, and most importantly, reliable communication [173]. This technology has been specifically designed for use with the smart grid, and this research has outlined the potential use of such technology with Li-ion batteries.

The changes in communication performance with Li-ion cell SoC have been determined in Chapter 5. It has been shown that such changes were of greater significance at certain carrier frequencies. Specifically, and using a maximum modulation order of 512-QAM, for the tested carrier frequencies of 10 MHz to 6 GHz, carrier

frequency ranges of 50 MHz to 400 MHz, 1133 MHz to 1652 MHz, and 3300 MHz to 4000 MHz were determined to be most suitable for an in-situ Li-ion PLC system when changes due to SoC are taken into consideration. These ranges of carrier frequencies offer much wider bandwidths than those specified in existing PLC standards, such as HomePlug AV 2 which uses 3455 equally spaced OFDM subcarriers in the range of 1.8 MHz to 86.13 MHz. Using a range of 3300 MHz to 4000 MHz would allow for 28672 OFDM subcarriers. The advantage of such a wide frequency range of suitability allows for communication with very large-scale energy storage systems with many thousands of smart cells on a single network. Moreover, this wide frequency range allows for ease of selection of a reduced bandwidth that is most appropriate not only based on the changes with SoC of the cells, but also on the configuration of the cells within the battery, as it has been presented in Chapter 6. Finally, the effects of SoC on the communication system may increase with the addition of cells in the battery, hence it may be appropriate to select a smaller bandwidth based on a higher threshold of S21 magnitude attenuation. This work has demonstrated the relationships between the measured S21 magnitude and phase of the Li-ion cell as a communication channel, and with the symbol error ratio (SER) and error vector magnitude (EVM) of the data transmitted through the cell using PLC. Moreover, it has been shown that measuring only S-parameters enables an adequate derivation of the expected communication performance.

The effects of battery configuration on the PLC performance has been studied in Chapter 6. These battery configurations were accomplished using a bespoke shunt-through cell holder designed and fabricated within this research for the purpose of straightforward reconfiguration within the experiment, high frequency capability, and low electromagnetic interference (EMI). Using four different battery configurations to represent a baseline of large-scale configurations used in BEV and smart grid systems, it has been shown that the PLC performance changes with battery configuration, and that increasing the number of Li-ion cells in series has a consequential negative impact on the communication performance. Furthermore, these changes in communication performance are carrier frequency dependent, whereby certain carrier frequencies such as 4000 MHz show the maximum SER with modulation orders of 512-QAM and 1024-QAM, whereas other frequencies such as 2400 MHz show no SER

and very low EVM. Specifically, the ranges of acceptable carrier frequencies for all battery configurations tested are determined to be 2000 MHz to 2800 MHz, 3500 MHz to 3800 MHz and 4450 MHz to 6000 MHz, wherein 1024-QAM can be used to achieve the highest data rates. For example, it is expected that using 1024-QAM with a carrier frequency of 3600 MHz with a bandwidth of approximately 300 MHz will exceed the physical layer data rate capabilities found in IEEE 1901 [171]. Similarly to the findings in Chapter 5 whereby the range of suitable carrier frequencies for a Li-ion at various SoCs is large, the range of suitable carrier frequencies for an in-situ PLC in various battery configurations is also large. Despite this fact, only the frequency range of 3500 MHz to 3800 MHz remains suitable for both change in battery configuration and battery SoC. In addition, it is expected that the addition of cells in parallel configuration will reduce the bandwidth and the performance of the communication system. To mitigate this drawback, this research has shown that the addition of cells in series reduces this attenuation in S21 magnitude. Hence, the architecture of future battery systems may be able to take these results into account when designing large-scale energy storage systems with an in-situ PLC system. For a bandwidth of 300 MHz, 12288 equally spaced OFDM subcarriers may be utilised. When using the same techniques as HomePlug AV2, a theoretical maximum physical rate of 7190 Mbit/s may be achieved. This value far exceeds the performance that would be required of a large-scale battery system based on the data that each smart cell would communicate, such as temperature and voltage sensor data. However, as already stated, this performance is expected to change dependant on the configuration of the battery.

When considering the ranges of suitable carrier frequencies for an in-situ Li-ion battery PLC system with QAM with the simulated BEV environment presented in Chapter 4, for the changes with Li-ion cell SoC presented in Chapter 5, and for the changes with Li-ion battery configuration presented in Chapter 6, it is determined that the overall suitable carrier frequency ranges are 30 MHz to 50 MHz, and 3500 MHz to 3800 MHz. At these carrier frequencies, the PLC system was able to function with little hindrance from changes to both SoC and battery configuration. However, the simulated environment created and used in Chapter 4 is limited to a maximum carrier frequency of 200 MHz due to the available Li-ion characteristic data available in existing literature obtained using EIS. Furthermore, the configuration of the PLC

system will impact these ranges of suitable carrier frequencies depending on whether a series-through or shunt-through topology is chosen. This research demonstrates that an increase in internal impedance of the Li-ion cell increases communication error with series-through and decreases communication error with shunt-through topologies.

These key contributions of this research explained above, have for the first time, demonstrated the possibilities of using PLC and QAM within Li-ion batteries of various SoC and cell configuration. My research has categorically demonstrated that under certain conditions, it is possible to achieve high data rate capabilities despite the changing characteristics of the Li-ion cell with SoC and cell configuration.

Through these contributions, this research has achieved the objectives outlined in the Introduction:

- The requirements of a communication system capable of operating within large-scale energy storage have been defined in Chapter 2.
- The parameters for the characterisation of Li-ion cells relevant to PLC have been defined and explained in Chapter 3.
- Existing methodologies for the characterisation of Li-ion cells as a communication channel have been evaluated in Chapter 2 and supplement the techniques used in the research methodology presented in Chapter 3. Such existing methods include the use of EIS for measuring various characteristics of the Li-ion cell, such as SoH, using low frequency alternating current (AC). The research presented in this thesis, however, performs S-parameter measurements for high frequencies up to 6 GHz for cell characterisation as a communication channel.
- Improvements to Li-ion cell characterisation methods to enhance the reproducibility and accuracy of communication performance tests have been presented in Chapter 3. The methodology used in this thesis includes the use of the VNA and VST for communication channel and performance testing, with the inclusion of bespoke cell holders for improving the reproducibility and accuracy of the results.

- The performance of an in-situ Li-ion battery communication system has been determined in a variety of circumstances:
  - when the Li-ion battery is under the load of a driving BEV, presented in Chapter 4;
  - when the Li-ion battery is at different SoC due to charging or discharging, presented in Chapter 5;
  - and when the Li-ion battery is configured in single cell, two cells in parallel, two cells in series, and two cells in parallel and in series, presented in Chapter 6.
- New experimental methodologies for testing the performance of PLC in Li-ion cells have been defined and implemented throughout this thesis.
- Parameters of carrier frequency, QAM order, and battery configuration for an in-situ Li-ion battery PLC system have been proposed within this Conclusions and Future Work chapter.

7.2 Future Work

The high data rate capabilities within the Li-ion battery using PLC and QAM as demonstrated within this thesis will enable the development of academically interesting and applicable research topics. Further research may include, firstly, determining the changes in communication performance with Li-ion SoH in order to understand how changes in the characteristics of the Li-ion cell, such as internal impedance, may impact the PLC due to cell ageing and charge cycles. Such research is important for long-term usage of Li-ion batteries to ensure that the PLC system can continue to operate for the full lifetime of the energy storage system and that it does not diminish in functionality with cell ageing. Since the SoH of Li-ion cells change with calendar ageing and cycling, reliably reproducing and controlling the SoH for such testing may be challenging.

Secondly, to understand the changes in communication performance with batteries of different chemistries. Notwithstanding exploration of Li-ion cells of different

models, with the aim to determine any relationships between the characteristics of the parameters of the battery, such as the thickness of the jelly roll, with the performance of the in-situ PLC system. Using such research, it will be possible to determine the most appropriate battery technology when an in-situ PLC is considered.

Thirdly, the realisation of a mesh network of smart cells within a large-scale battery, and understanding the limits in communication performance due to EMI and the sheer number of connected cells. Since a large-scale battery may consist of thousand of cells, it is vital to determine factors that may limit the performance of PLC within this system, including noise, signal reflections, and propagation of changing Li-ion cell characteristics. These factors will affect the communication round trip time which affects the smart cell's ability to limit packet loss due to data corruption caused by significant noise, for example.

Finally, the latency between a safety event, such as cell overheating, and the communication of such an event with other smart cells or an external BMS must be measured to determine whether the smart cell is capable of performing safety critical actions within the small window of time with which an overheat event may cause thermal runaway. The smart cell and the BMS must be able to act quickly to mitigate loss of thermal stability within Li-ion cells.

7.3 Summary

This work has shown that PLC within Li-ion batteries can be used as a high throughput communication system, with optimal parameters provided to utilise QAM as a modulation scheme to enhance data rate for carrier frequencies up to 6 GHz. Through the simulation methods presented in Chapter 4, an optimal battery architecture can be designed for the purpose of smart battery communication, with Chapters 5 and 6 detailing the analysis of real performance data with various battery SoCs and cell configurations. These key pertinent contributions are beneficial to improving energy storage safety and performance in BEVs and smart grids.

Bibliography

[1] M. J. Koshkouei, E. Kampert, A. D. Moore and M. D. Higgins, 'Evaluation of an in situ QAM-based power line communication system for lithium-ion batteries,' *IET Electrical Systems in Transportation*, vol. 12, no. 1, pp. 15–25, 2021. DOI: 10.1049/els2.12033.

[2] M. J. Koshkouei, E. Kampert, A. D. Moore and M. D. Higgins, 'Impact of battery state of charge on in-situ power line communication within an intelligent electric vehicle,' in *2022 IEEE 25th International Conference on Intelligent Transportation Systems (ITSC)*, IEEE, Oct. 2022. DOI: 10.1109/itsc55140.2022.9921800.

[3] M. J. Koshkouei, E. Kampert, A. D. Moore and M. D. Higgins, 'Impact of lithium-ion battery state of charge on in situ QAM-based power line communication,' *Sensors*, vol. 22, no. 16, p. 6144, Aug. 2022, ISSN: 1424-8220. DOI: 10.3390/s22166144.

[4] M. J. Koshkouei, E. Kampert, A. D. Moore and M. D. Higgins, 'In-situ QAM-based power line communication for large-scale intelligent battery management,' in *2022 7th International Conference on Robotics and Automation Engineering (ICRAE)*, IEEE, Nov. 2022. DOI: 10.1109/icrae56463.2022.10056199.

[5] M. J. Koshkouei, E. Kampert, A. D. Moore and M. D. Higgins, 'Battery configuration dependence to PLC using high-order QAM,' *under review*, 2022.

[6] E. Kampert, M. J. Koshkouei, Y. K. Mo and M. D. Higgins, 'OTA 5G and beyond channel evaluation in a manufacturing environment,' in *2022 3rd URSI Atlantic and Asia Pacific Radio Science Meeting (AT-AP-RASC)*, IEEE, May 2022. DOI: 10.23919/at-ap-rasc54737.2022.9814165.

[7] Y. Liu, V. Sanchez, P. J. Freire, J. E. Prilepsky, M. J. Koshkouei and M. D. Higgins, 'Attention-aided partial bidirectional RNN-based nonlinear equalizer in coherent optical systems,' *Optics Express*, vol. 30, no. 18, p. 32 908, Aug. 2022. DOI: 10.1364/oe.464159.

[8] G. Boyle, *Renewable Energy Power for a Sustainable Future, Power for a Sustainable Future*. Oxford University Press, 2012, p. 512, ISBN: 9780199545339.

[9] BP. 'Bp statistical review of world energy 2019 - full report.' (14th Jun. 2019), [Online]. Available: https://www.bp.com/content/dam/bp/business-sites/en/global/corporate/pdfs/energy-economics/statistical-review/bp-stats-review-2019-full-report.pdf (visited on 30/09/2022).

[10] J. Boyd. 'Hook moor wind farm from footpath looking north.' (30th Dec. 2021), [Online]. Available: https://www.geograph.org.uk/photo/7067519.

[11] Greens MPs. 'Aerial photo of the PS10 concentrating solar thermal power plant.' (), [Online]. Available: https://www.flickr.com/photos/greensmps/6497633977 (visited on 29/12/2022).

[12] Scottish Government. 'Pelamis P2 wave energy device.' (Jul. 2011), [Online]. Available: https://www.flickr.com/photos/scottishgovernment/7020981211 (visited on 29/12/2022).

[13] P. Breeze, *Hydropower*. Elsevier Science & Technology Books, 2018, p. 150, ISBN: 9780128129067. DOI: 10.1016/c2016-0-03622-7.

[14] J. Ekanayake, K. Liyanage, J. Wu, A. Yokoyama and N. Jenkins, *Smart Grid*. Wiley, Feb. 2012. DOI: 10.1002/9781119968696.

[15] Z. Shahan. 'Largest pumped-hydro facility in world turns on in china,' CleanTechnica. (4th Jan. 2022), [Online]. Available: https://cleantechnica.com/2022/01/04/largest-pumped-hydro-facility-in-world-turns-on-in-china/.

[16] SMS. 'SMS energises 50MW battery energy storage site in cambridgeshire.' (31st Jan. 2022), [Online]. Available: https://www.sms-plc.com/insights/sms-energises-50mw-battery-energy-storage-site-in-cambridgeshire/.

[17] Department for Transport and Office for Zero Emission Vehicles. 'Transitioning to zero emission cars and vans: 2035 delivery plan.' (14th Jul. 2021), [Online]. Available: https://www.gov.uk/government/publications/transitioning-to-zero-emission-cars-and-vans-2035-delivery-plan.

[18] European Commission. 'Zero emission vehicles: First 'fit for 55' deal will end the sale of new co2 emitting cars in europe by 2035.' (28th Oct. 2022), [Online]. Available: https://ec.europa.eu/commission/presscorner/detail/en/ip_22_6462.

[19] M. Bini, D. Capsoni, S. Ferrari, E. Quartarone and P. Mustarelli, 'Rechargeable lithium batteries,' in *Rechargeable Lithium Batteries*, Elsevier, 2015, pp. 1–17. DOI: 10.1016/b978-1-78242-090-3.00001-8.

[20] J. N. Barkenbus, 'Prospects for electric vehicles,' *Sustainability*, vol. 12, no. 14, p. 5813, 2020. DOI: 10.3390/su12145813.

[21] N. T. Kalyani and S. Dhoble, 'Energy materials: Applications and propelling opportunities,' in *Energy Materials*, Elsevier, 2021, pp. 567–580. DOI: 10.1016/b978-0-12-823710-6.00011-x.

[22] S. Simons, J. Schmitt, B. Tom, H. Bao, B. Pettinato and M. Pechulis, 'Advanced concepts,' in *Thermal, Mechanical, and Hybrid Chemical Energy Storage Systems*, Elsevier, 2021, pp. 569–596. DOI: 10.1016/b978-0-12-819892-6.00010-1.

[23] S. B. Sarmah, P. Kalita, A. Garg *et al.*, 'A review of state of health estimation of energy storage systems: Challenges and possible solutions for futuristic applications of li-ion battery packs in electric vehicles,' *Journal of Electrochemical Energy Conversion and Storage*, vol. 16, no. 4, 2019. DOI: 10.1115/1.4042987.

[24] H. C. a. Adhirath Mandal Haengmuk Cho Adhirath Mandal, 'Greenhouse gas emission from electric vehicle's and li-ion battery – a review,' *International Journal of Mechanical and Production Engineering Research and Development*, vol. 9, no. 3, pp. 61–74, 2019. DOI: 10.24247/ijmperdjun20197.

[25] X. Zeng, M. Li, D. A. El-Hady *et al.*, 'Commercialization of lithium battery technologies for electric vehicles,' *Advanced Energy Materials*, vol. 9, no. 27, p. 1 900 161, 2019. DOI: 10.1002/aenm.201900161.

[26] A. Faraz, A. Ambikapathy, S. Thangavel, K. Logavani and G. A. Prasad, 'Battery electric vehicles (BEVs),' in *Electric Vehicles*, Springer Singapore, 2020, pp. 137–160. DOI: 10.1007/978-981-15-9251-5_8.

[27] A. Masias, J. Marcicki and W. A. Paxton, 'Opportunities and challenges of lithium ion batteries in automotive applications,' *ACS Energy Letters*, vol. 6, no. 2, pp. 621–630, Jan. 2021. DOI: 10.1021/acsenergylett.0c02584.

[28] D. Andrea, *Battery Management Systems for Large Lithium Battery Packs*. Artech House Publishers, Sep. 2010, 300 pp., ISBN: 1608071049.

[29] J. Q. Yevgen Barsukov, *Battery Power Management for Portable Devices*. Artech House Publishers, Apr. 2013, 200 pp., ISBN: 1608074919.

[30] L. Lu, X. Han, J. Li, J. Hua and M. Ouyang, 'A review on the key issues for lithium-ion battery management in electric vehicles,' *Journal of Power Sources*, vol. 226, pp. 272–288, Mar. 2013. DOI: 10.1016/j.jpowsour.2012.10.060.

[31] X. Tang, C. Zou, K. Yao *et al.*, 'A fast estimation algorithm for lithium-ion battery state of health,' *Journal of Power Sources*, vol. 396, pp. 453–458, 2018. DOI: 10.1016/j.jpowsour.2018.06.036.

[32] F. H. Gandoman, V. Nasiriyan, B. Mohammadi-Ivatloo and D. Ahmadian, 'The concept of li-ion battery control strategies to improve reliability in electric vehicle (ev) applications,' in *Electric Vehicle Integration via Smart Charging: Technology, Standards, Implementation, and Applications*, V. Vahidinasab and B. Mohammadi-Ivatloo, Eds. Springer International Publishing, 2022, pp. 35–48, ISBN: 978-3-031-05909-4. DOI: 10.1007/978-3-031-05909-4_2.

[33] J. Fleming, T. Amietszajew, J. Charmet, A. J. Roberts, D. Greenwood and R. Bhagat, 'The design and impact of in-situ and operando thermal sensing for smart energy storage,' *Journal of Energy Storage*, vol. 22, pp. 36–43, 2019. DOI: 10.1016/j.est.2019.01.026.

[34] G. Han, J. Yan, Z. Guo, D. Greenwood, J. Marco and Y. Yu, 'A review on various optical fibre sensing methods for batteries,' *Renewable and Sustainable Energy Reviews*, vol. 150, p. 111 514, 2021. DOI: 10.1016/j.rser.2021.111514.

[35] Y. Yu, T. Vincent, J. Sansom, D. Greenwood and J. Marco, 'Distributed internal thermal monitoring of lithium ion batteries with fibre sensors,' *Journal of Energy Storage*, vol. 50, p. 104 291, Jun. 2022. DOI: 10.1016/j.est.2022.104291.

[36] F. Ji, L. Liao, T. Wu, C. Chang and M. Wang, 'Self-reconfiguration batteries with stable voltage during the full cycle without the dc-dc converter,' *Journal of Energy Storage*, vol. 28, p. 101 213, Apr. 2020. DOI: 10.1016/j.est.2020.101213.

[37] Y. Shang, K. Liu, N. Cui, N. Wang, K. Li and C. Zhang, 'A compact resonant switched-capacitor heater for lithium-ion battery self-heating at low temperatures,' *IEEE Transactions on Power Electronics*, vol. 35, no. 7, pp. 7134–7144, 2020. DOI: 10.1109/tpel.2019.2954703.

[38] L. Patnaik, A. V. J. S. Praneeth and S. S. Williamson, 'A closed-loop constant-temperature constant-voltage charging technique to reduce charge time of lithium-ion batteries,' *IEEE Transactions on Industrial Electronics*, vol. 66, no. 2, pp. 1059–1067, 2019. DOI: 10.1109/tie.2018.2833038.

[39] S. Steinhorst, 'Design and verification methodologies for smart battery cells,' in *2016 International Symposium on Integrated Circuits (ISIC)*, IEEE, 2016. DOI: 10.1109/isicir.2016.7829706.

[40] T. A. Vincent, B. Gulsoy, J. E. Sansom and J. Marco, 'In-situ instrumentation of cells and power line communication data acquisition towards smart cell development,' *Journal of Energy Storage*, vol. 50, p. 104 218, 2022. DOI: 10.1016/j.est.2022.104218.

[41] C. Vlachou and S. Henri, *A Practical Guide to Power Line Communications*. Cambridge University Press, May 2022. DOI: 10.1017/9781108890823.

[42] HomePlug Power Line Alliance, 'Homeplug 1.0 technology white paper,' 11th Feb. 2005. [Online]. Available: https://www.solwise.co.uk/downloads/files/hp_1.0_technicalwhitepaper_final.pdf.

[43] European Commission, Directorate General for Communication, *The European climate law*. Publications Office, 2020. DOI: 10.2775/790913.

[44] S. Hemavathi, 'Overview of cell balancing methods for li-ion battery technology,' *Energy Storage*, vol. 3, no. 2, Sep. 2020. DOI: 10.1002/est2.203.

[45] D. Li, L. Wang, C. Duan, Q. Li and K. Wang, 'Temperature prediction of lithium-ion batteries based on electrochemical impedance spectrum: A review,' *International Journal of Energy Research*, vol. 46, no. 8, pp. 10 372–10 388, Mar. 2022. DOI: 10.1002/er.7905.

[46] K. Desmond, *Innovators in battery technology, profiles of 93 influential electrochemists*. 2016, p. 271, ISBN: 9780786499335.

[47] J. Warner, 'History of vehicle electrification,' in *The Handbook of Lithium-Ion Battery Pack Design*, Elsevier, 2015, pp. 9–21. DOI: 10.1016/b978-0-12-801456-1.00002-6.

[48] Y. Nishi, 'Past, present and future of lithium-ion batteries,' in *Lithium-Ion Batteries*, Elsevier, 2014, pp. 21–39. DOI: 10.1016/b978-0-444-59513-3.00002-9.

[49] J. Warner, 'Lithium-ion and other cell chemistries,' in *The Handbook of Lithium-Ion Battery Pack Design*, Elsevier, 2015, pp. 65–89. DOI: 10.1016/b978-0-12-801456-1.00007-5.

[50] K. Mizushima, P. Jones, P. Wiseman and J. Goodenough, 'Lixcoo2: A new cathode material for batteries of high energy density,' *Materials Research Bulletin*, vol. 15, no. 6, pp. 783–789, Jun. 1980. DOI: 10.1016/0025-5408(80)90012-4.

[51] M. V. Reddy, A. Mauger, C. M. Julien, A. Paolella and K. Zaghib, 'Brief history of early lithium-battery development,' *Materials*, vol. 13, no. 8, p. 1884, Apr. 2020. DOI: 10.3390/ma13081884.

[52] M. Li, J. Lu, Z. Chen and K. Amine, '30 years of lithium-ion batteries,' *Advanced Materials*, vol. 30, no. 33, p. 1 800 561, Jun. 2018. DOI: 10.1002/adma.201800561.

[53] B. Li, Y. Wang, W. Tu *et al.*, 'Improving cyclic stability of lithium nickel manganese oxide cathode for high voltage lithium ion battery by modifying electrode/electrolyte interface with electrolyte additive,' *Electrochimica Acta*, vol. 147, pp. 636–642, Nov. 2014. DOI: 10.1016/j.electacta.2014.09.151.

[54] K. Xu, 'Nonaqueous liquid electrolytes for lithium-based rechargeable batteries,' *Chemical Reviews*, vol. 104, no. 10, pp. 4303–4418, Sep. 2004. DOI: 10.1021/cr030203g.

[55] J. B. Goodenough, 'Rechargeable batteries: Challenges old and new,' *Journal of Solid State Electrochemistry*, vol. 16, no. 6, pp. 2019–2029, May 2012. DOI: 10.1007/s10008-012-1751-2.

[56] W. Ren, Y. Zheng, Z. Cui, Y. Tao, B. Li and W. Wang, 'Recent progress of functional separators in dendrite inhibition for lithium metal batteries,' *Energy Storage Materials*, vol. 35, pp. 157–168, Mar. 2021. DOI: 10.1016/j.ensm.2020.11.019.

[57] M. E. H. Assad, A. Khosravi, M. Malekan, M. A. Rosen and M. A. Nazari, 'Energy storage,' in *Design and Performance Optimization of Renewable Energy Systems*, Elsevier, 2021, pp. 205–219. DOI: 10.1016/b978-0-12-821602-6.00016-x.

[58] M. U. Ali, A. Zafar, S. H. Nengroo, S. Hussain, M. Junaid Alvi and H.-J. Kim, 'Towards a smarter battery management system for electric vehicle applications: A critical review of lithium-ion battery state of charge estimation,' *Energies*, vol. 12, no. 3, 2019, ISSN: 1996-1073. DOI: 10.3390/en12030446. [Online]. Available: https://www.mdpi.com/1996-1073/12/3/446.

[59] R. Satpathy and V. Pamuru, 'Off-grid solar photovoltaic systems,' in *Solar PV Power*, Elsevier, 2021, pp. 267–315. DOI: 10.1016/b978-0-12-817626-9.00007-1.

[60] F. H. Gandoman, J. Jaguemont, S. Goutam *et al.*, 'Concept of reliability and safety assessment of lithium-ion batteries in electric vehicles: Basics, progress, and challenges,' *Applied Energy*, vol. 251, p. 113 343, 2019. DOI: 10.1016/j.apenergy.2019.113343.

[61] H. Löbberding, S. Wessel, C. Offermanns *et al.*, 'From cell to battery system in BEVs: Analysis of system packing efficiency and cell types,' *World Electric Vehicle Journal*, vol. 11, no. 4, p. 77, Dec. 2020. DOI: 10.3390/wevj11040077.

[62] R. Schröder, M. Aydemir and G. Seliger, 'Comparatively assessing different shapes of lithium-ion battery cells,' *Procedia Manufacturing*, vol. 8, pp. 104–111, 2017. DOI: 10.1016/j.promfg.2017.02.013.

[63] F. Lambert. 'Tesla model 3 battery packs have capacities of 50 kwh and 75 kwh, says elon musk.' (Aug. 2017), [Online]. Available: https://electrek.co/2017/08/08/tesla-model-3-battery-packs-50-kwh-75-kwh-elon-musk/ (visited on 23/05/2019).

[64] F. Lambert. 'Tesla model 3: Exclusive first look at tesla's new battery pack architecture,' Electrek. (24th Aug. 2017), [Online]. Available: https://electrek.co/2017/08/24/tesla-model-3-exclusive-battery-pack-architecture/ (visited on 28/05/2019).

[65] 'BYD Yuan EV360 specification (chinese),' Autohome. (2018), [Online]. Available: https://www.autohome.com.cn/spec/33506/ (visited on 23/05/2019).

[66] *2016 nissan leaf specifications*, Sep. 2015. [Online]. Available: https://nissannews.com/media_storage/downloads/2016_Nissan_LEAF_Specs_FINAL.pdf (visited on 23/05/2019).

[67] 'BYD tang SUV PHEV available for pre-orders starting at 48.3k before incentives; twice that for performance model.' (23rd Jan. 2015), [Online]. Available: https://www.greencarcongress.com/2015/01/20150123-tang.html (visited on 23/05/2019).

[68] 'BAOJUN E100 EV specs.' (2018), [Online]. Available: https://wattev2buy.com/electric-vehicles/baojun-electric-vehicles/baojun-e100-ev/ (visited on 23/05/2019).

[69] T. de Feijter. 'The baojun E100 is a general motors electric city car.' (13th Dec. 2016), [Online]. Available: https://carnewschina.com/2016/12/13/the-baojun-e100-is-a-general-motors-electric-city-car/ (visited on 23/05/2019).

[70] *Outlander PHEV brochure*, 13th Dec. 2018. [Online]. Available: https://www-cms.prod.mipulse.co/content/dam/mitsubishi-motors-gb/images/site-images/brochures/brochure-files/outlander_phev.pdf (visited on 23/05/2019).

[71] 'Mitsubishi bringing 2018 outlander phev to us in december.' (28th Sep. 2017), [Online]. Available: https://www.greencarcongress.com/2017/09/20170928-outlander.html (visited on 28/05/2019).

[72] *Rechargeable lithium-ion battery e63*, LG Chem, 2018.

[73] 'Chery eq ev (qq ev).' (2016), [Online]. Available: https://chinaautoweb.com/car-models/chery-eq-ev/ (visited on 23/05/2019).

[74] 'Emgrand ev.' (2019), [Online]. Available: http://global.geely.com/car/emgrand-ev-2/ (visited on 23/05/2019).

[75] K. Berman, J. Dzluba, C. Hamilton, R. Carlson, J. Jackson and P. Sklar, 'The lithium ion battery and the ev market: The science behind what you can't see,' BMO Capital Markets Ltd, London, Tech. Rep., 2018. [Online]. Available: http://www.fullertreacymoney.com/system/data/files/PDFs/2018/February/22nd/BMO_Lithium_Ion_Battery_EV_Mkt_(20_Feb_2018).pdf (visited on 28/05/2019).

[76] R. Gupta-Chaudhary, G. M. Adler, M. Anderman *et al.*, 'Electric vehicles - ready(ing) for adoption,' Citi GPS: Global Perspectives & Solutions, New York City, Tech. Rep., 2018. [Online]. Available: https://www.citibank.com/commercialbank/insights/assets/docs/2018/electric-vehicles.pdf (visited on 28/05/2019).

[77] 'BYD e5 EV450 review.' (2018), [Online]. Available: https://wattev2buy.com/electric-vehicles/byd-electric-vehicles/byd-e5-300-ev/ (visited on 23/05/2019).

[78] J. Wang. 'Spy shots: BYD e5 ev sedan is ready for the chinese auto market,' CarNewsChina. (5th Mar. 2015), [Online]. Available: http://carnewschina.com/2015/03/05/spy-shots-byd-e5-ev-sedan-is-ready-for-the-chinese-auto-market/ (visited on 23/05/2019).

[79] J. Trop. 'Why lfp batteries are poised to bring down entry-level ev prices,' Techcrunch. (26th Jun. 2022), [Online]. Available: https://techcrunch.com/2022/06/26/why-lfp-batteries-are-poised-to-bring-down-entry-level-ev-prices/ (visited on 10/10/2022).

[80] K. Liu, Y. Wang and X. Lai, 'Introduction to battery full-lifespan management,' in *Data Science-Based Full-Lifespan Management of Lithium-Ion Battery*, Springer International Publishing, 2022, pp. 1–25. DOI: 10.1007/978-3-031-01340-9_1.

[81] Y. Liu, Y. He, H. Bian, W. Guo and X. Zhang, 'A review of lithium-ion battery state of charge estimation based on deep learning: Directions for improvement and future trends,' *Journal of Energy Storage*, vol. 52, p. 104 664, 2022. DOI: 10.1016/j.est.2022.104664.

[82] L. Komsiyska, T. Buchberger, S. Diehl *et al.*, 'Critical review of intelligent battery systems: Challenges, implementation, and potential for electric vehicles,' *Energies*, vol. 14, no. 18, p. 5989, Sep. 2021. DOI: 10.3390/en14185989.

[83] S. K. Pradhan and B. Chakraborty, 'Battery management strategies: An essential review for battery state of health monitoring techniques,' *Journal of Energy Storage*, vol. 51, p. 104 427, 2022. DOI: 10.1016/j.est.2022.104427.

[84] S. Ma, M. Jiang, P. Tao *et al.*, 'Temperature effect and thermal impact in lithium-ion batteries: A review,' *Progress in Natural Science: Materials International*, vol. 28, no. 6, pp. 653–666, 2018. DOI: 10.1016/j.pnsc.2018.11.002.

[85] M. H. Lipu, M. Hannan, T. F. Karim *et al.*, 'Intelligent algorithms and control strategies for battery management system in electric vehicles: Progress, challenges and future outlook,' *Journal of Cleaner Production*, vol. 292, p. 126 044, 2021. DOI: 10.1016/j.jclepro.2021.126044.

[86] H. Gabbar, A. Othman and M. Abdussami, 'Review of battery management systems (BMS) development and industrial standards,' *Technologies*, vol. 9, no. 2, p. 28, Apr. 2021. DOI: 10.3390/technologies9020028.

[87] M.-K. Tran and M. Fowler, 'A review of lithium-ion battery fault diagnostic algorithms: Current progress and future challenges,' *Algorithms*, vol. 13, no. 3, p. 62, Mar. 2020. DOI: 10.3390/a13030062.

[88] J. Tian, Y. Wang and Z. Chen, 'Sensor fault diagnosis for lithium-ion battery packs based on thermal and electrical models,' *International Journal of Electrical Power & Energy Systems*, vol. 121, p. 106 087, Oct. 2020. DOI: 10.1016/j.ijepes.2020.106087.

[89] K. Liu, T. Ashwin, X. Hu, M. Lucu and W. D. Widanage, 'An evaluation study of different modelling techniques for calendar ageing prediction of lithium-ion batteries,' *Renewable and Sustainable Energy Reviews*, vol. 131, p. 110 017, Oct. 2020. DOI: 10.1016/j.rser.2020.110017.

[90] H. Li, H. Sun, B. Chen *et al.*, 'A cubature kalman filter for online state-of-charge estimation of lithium-ion battery using a gas-liquid dynamic model,' *Journal of Energy Storage*, vol. 53, p. 105 141, Sep. 2022. DOI: 10.1016/j.est.2022.105141.

[91] W. Bai, X. Zhang, Z. Gao *et al.*, 'State of charge estimation for lithium-ion batteries under varying temperature conditions based on adaptive dual extended kalman filter,' *Electric Power Systems Research*, vol. 213, p. 108 751, Dec. 2022. DOI: 10.1016/j.epsr.2022.108751.

[92] Q. Ke, S. Jiang, W. Li, W. Lin, X. Li and H. Huang, 'Potential of ultrasonic time-of-flight and amplitude as the measurement for state of charge and physical changings of lithium-ion batteries,' *Journal of Power Sources*, vol. 549, p. 232 031, Nov. 2022. DOI: 10.1016/j.jpowsour.2022.232031.

[93] M. Adaikkappan and N. Sathiyamoorthy, 'Modeling, state of charge estimation, and charging of lithium-ion battery in electric vehicle: A review,' *International Journal of Energy Research*, vol. 46, no. 3, pp. 2141–2165, Oct. 2021. DOI: 10.1002/er.7339.

[94] M. Mussi, L. Pellegrino, M. Restelli and F. Trovò, 'An online state of health estimation method for lithium-ion batteries based on time partitioning and data-driven model identification,' *Journal of Energy Storage*, vol. 55, p. 105 467, Nov. 2022. DOI: 10.1016/j.est.2022.105467.

[95] J. Wu, L. Fang, G. Dong and M. Lin, 'State of health estimation of lithium-ion battery with improved radial basis function neural network,' *Energy*, vol. 262, p. 125 380, Jan. 2023. DOI: 10.1016/j.energy.2022.125380.

[96] Z. Wang, G. Feng, D. Zhen, F. Gu and A. D. Ball, 'State of health estimation of lithium-ion batteries from charging data: A machine learning method,' in *Proceedings of IncoME-VI and TEPEN 2021*, Springer International Publishing, Sep. 2022, pp. 707–719. DOI: 10.1007/978-3-030-99075-6_57.

[97] K. Luo, X. Chen, H. Zheng and Z. Shi, 'A review of deep learning approach to predicting the state of health and state of charge of lithium-ion batteries,' *Journal of Energy Chemistry*, vol. 74, pp. 159–173, Nov. 2022. DOI: 10.1016/j.jechem.2022.06.049.

[98] G. Vennam, A. Sahoo and S. Ahmed, 'A survey on lithium-ion battery internal and external degradation modeling and state of health estimation,' *Journal of Energy Storage*, vol. 52, p. 104 720, Aug. 2022. DOI: 10.1016/j.est.2022.104720.

[99] N. Bouchhima, M. Gossen, S. Schulte and K. P. Birke, 'Lifetime of self-reconfigurable batteries compared with conventional batteries,' *Journal of Energy Storage*, vol. 15, pp. 400–407, Feb. 2018. DOI: 10.1016/j.est.2017.11.014.

[100] L. He, Z. Yang, Y. Gu, C. Liu, T. He and K. G. Shin, 'SoH-aware reconfiguration in battery packs,' *IEEE Transactions on Smart Grid*, vol. 9, no. 4, pp. 3727–3735, Jul. 2018. DOI: 10.1109/tsg.2016.2639445.

[101] N. Wassiliadis, J. Schneider, A. Frank *et al.*, 'Review of fast charging strategies for lithium-ion battery systems and their applicability for battery electric vehicles,' *Journal of Energy Storage*, vol. 44, p. 103 306, 2021. DOI: 10.1016/j.est.2021.103306.

[102] N. Martiny, A. Rheinfeld, J. Geder, Y. Wang, W. Kraus and A. Jossen, 'Development of an all kapton-based thin-film thermocouple matrix for in situ temperature measurement in a lithium ion pouch cell,' *IEEE Sensors Journal*, vol. 14, no. 10, pp. 3377–3384, Oct. 2014. DOI: 10.1109/jsen.2014.2331996.

[103] S.-O. Yang, S. Lee, S. H. Song and J. Yoo, 'Development of a distributed optical thermometry technique for battery cells,' *International Journal of Heat and Mass Transfer*, vol. 194, p. 123 020, 2022. DOI: 10.1016/j.ijheatmasstransfer.2022.123020.

[104] Y. Yu, E. Vergori, D. Worwood *et al.*, 'Distributed thermal monitoring of lithium ion batteries with optical fibre sensors,' *Journal of Energy Storage*, vol. 39, p. 102 560, 2021. DOI: 10.1016/j.est.2021.102560.

[105] E. McTurk, T. Amietszajew, J. Fleming and R. Bhagat, 'Thermo-electrochemical instrumentation of cylindrical li-ion cells,' *Journal of Power Sources*, vol. 379, pp. 309–316, 2018, ISSN: 0378-7753. DOI: 10.1016/j.jpowsour.2018.01.060.

[106] M. S. Wahl, L. Spitthoff, H. I. Muri, A. Jinasena, O. S. Burheim and J. J. Lamb, 'The importance of optical fibres for internal temperature sensing in lithium-ion batteries during operation,' *Energies*, vol. 14, no. 12, p. 3617, Jun. 2021. DOI: 10.3390/en14123617.

[107] B. Gulsoy, T. Vincent, J. Sansom and J. Marco, 'In-situ temperature monitoring of a lithium-ion battery using an embedded thermocouple for smart battery applications,' *Journal of Energy Storage*, vol. 54, p. 105 260, Oct. 2022. DOI: 10.1016/j.est.2022.105260.

[108] Z. Wei, J. Zhao, H. He, G. Ding, H. Cui and L. Liu, 'Future smart battery and management: Advanced sensing from external to embedded multi-dimensional measurement,' *Journal of Power Sources*, vol. 489, p. 229 462, 2021. DOI: 10.1016/j.jpowsour.2021.229462.

[109] D. F. Frost and D. A. Howey, 'Completely decentralized active balancing battery management system,' *IEEE Transactions on Power Electronics*, vol. 33, no. 1, pp. 729–738, 2018. DOI: 10.1109/tpel.2017.2664922.

[110] P. Liu, D. Liu, Y. Shen, G. Ge, X. Yuan and X. Yang, 'Distributed online active balancing scheme for battery energy storage system,' *IET Electric Power Applications*, vol. 16, no. 1, pp. 29–40, 2021. DOI: 10.1049/elp2.12132.

[111] R. Zhang, J. Wu, R. Wang, R. Yan, Y. Zhu and X. He, 'A novel battery management system architecture based on an isolated power/data multiplexing transmission bus,' *IEEE Transactions on Industrial Electronics*, vol. 66, no. 8, pp. 5979–5991, 2019. DOI: 10.1109/tie.2018.2873143.

[112] R. Gozdur, T. Przerywacz and D. Bogdański, 'Low power modular battery management system with a wireless communication interface,' *Energies*, vol. 14, no. 19, p. 6320, 2021. DOI: 10.3390/en14196320.

[113] V. Marsic, T. Amietszajew, P. Igic, S. Faramehr and J. Fleming, 'Wireless communication test on 868 MHz and 2.4 GHz from inside the 18650 li-ion enclosed metal shell,' *Sensors*, vol. 22, no. 5, p. 1966, 2022. DOI: 10.3390/s22051966.

[114] N. Martiny, T. Mühlbauer, S. Steinhorst, M. Lukasiewycz and A. Jossen, 'Digital data transmission system with capacitive coupling for in-situ temperature sensing in lithium ion cells,' *Journal of Energy Storage*, vol. 4, pp. 128–134, Dec. 2015. DOI: 10.1016/j.est.2015.10.001.

[115] M. K. Lee, R. E. Newman, H. A. Latchman, S. Katar and L. Yonge, 'HomePlug 1.0 powerline communication LANs - protocol description and performance results,' *International Journal of Communication Systems*, vol. 16, no. 5, pp. 447–473, 2003. DOI: 10.1002/dac.601.

[116] J. Armstrong, 'OFDM for optical communications,' *Journal of Lightwave Technology*, vol. 27, no. 3, pp. 189–204, Feb. 2009. DOI: 10.1109/jlt.2008.2010061.

[117] H. A. Latchman, S. Katar, L. Yonge and S. Gavette, *Homeplug AV and IEEE 1901 A Handbook for PLC Designers and Users, A Handbook for PLC Designers and Users*. Wiley & Sons, Limited, John, 2013, ISBN: 9781118527535.

[118] Y.-A. Jung and Y.-H. You, 'Complexity effective sampling frequency offset estimation method for OFDM-based HomePlug green PHY systems,' *Symmetry*, vol. 10, no. 11, p. 544, Oct. 2018. DOI: 10.3390/sym10110544.

[119] L. Yonge, J. Abad, K. Afkhamie *et al.*, 'An overview of the HomePlug AV2 technology,' *Journal of Electrical and Computer Engineering*, vol. 2013, pp. 1–20, 2013. DOI: 10.1155/2013/892628.

[120] G. E. Elmore, 'Surface wave transmission system over a single conductor having e-fields terminating along the conductor,' US7567154B2, 2009.

[121] L. D. Bert, S. D'Alessandro and A. M. Tonello, 'Enhancements of g3-PLC technology for smart-home/building applications,' *Journal of Electrical and Computer Engineering*, vol. 2013, pp. 1–11, 2013. DOI: 10.1155/2013/746763.

[122] D. O. Abdeslam, Ed., *Smart Meters*. Springer International Publishing, 2023. DOI: 10.1007/978-3-031-27556-2.

[123] 'Prime alliance.' (17th Jun. 2023), [Online]. Available: https://www.prime-alliance.org/.

[124] T. T. Ha, *Theory and Design of Digital Communication Systems*. Cambridge University Press, Oct. 2010. DOI: 10.1017/cbo9780511778681.

[125] N. Andreadou and F.-N. Pavlidou, 'Modeling the noise on the OFDM power-line communications system,' *IEEE Transactions on Power Delivery*, vol. 25, no. 1, pp. 150–157, Jan. 2010. DOI: 10.1109/tpwrd.2009.2035295.

[126] T. Bai, H. Zhang, J. Wang *et al.*, 'Fifty years of noise modeling and mitigation in power-line communications,' *IEEE Communications Surveys - Tutorials*, vol. 23, no. 1, pp. 41–69, 2021. DOI: 10.1109/comst.2020.3033748.

[127] R. N. Youngworth, B. B. Gallagher and B. L. Stamper, 'An overview of power spectral density (PSD) calculations,' in *SPIE Proceedings*, H. P. Stahl, Ed., SPIE, Aug. 2005. DOI: 10.1117/12.618478.

[128] J. H. Fernandez, A. Omri and G. Oligeri, 'A noise reduction scheme for OFDM NB-PLC systems,' *e-Prime - Advances in Electrical Engineering, Electronics and Energy*, vol. 2, p. 100 043, 2022. DOI: 10.1016/j.prime.2022.100043.

[129] M. Zimmermann and K. Dostert, 'Analysis and modeling of impulsive noise in broad-band powerline communications,' *IEEE Transactions on Electromagnetic Compatibility*, vol. 44, no. 1, pp. 249–258, 2002. DOI: 10.1109/15.990732.

[130] J. Fleming, T. Amietszajew and A. Roberts, 'In-situ electronics and communications for intelligent energy storage,' *HardwareX*, vol. 11, E00294, 2022. DOI: 10.1016/j.ohx.2022.e00294.

[131] V. Marsic, T. Amietszajew, C. Gardner, P. Igic, S. Faramehr and J. Fleming, 'Impact of li-ion battery on system's overall impedance and received signal strength for power line communication (PLC),' *Sensors*, vol. 22, no. 7, p. 2634, 2022. DOI: 10.3390/s22072634.

[132] T. F. Landinger, G. Schwarzberger and A. Jossen, 'A novel method for high frequency battery impedance measurements,' in *2019 IEEE International Symposium on Electromagnetic Compatibility, Signal & Power Integrity (EMC+SIPI)*, IEEE, 2019. DOI: 10.1109/isemc.2019.8825315.

[133] *THVD8000: RS-485 transceiver with OOK modulation for power line communication*, Texas Instruments Inc., 2021. [Online]. Available: https://www.ti.com/product/THVD8000 (visited on 30/01/2023).

[134] *CC1200: Low power and high performance wireless transceiver*, Texas Instruments Inc., 2014. [Online]. Available: https://www.ti.com/product/CC1200 (visited on 30/01/2023).

[135] *CC2520: Second generation 2.4 ghz zigbee/ieee 802.15.4 wireless transceiver*, Texas Instruments Inc., 2007. [Online]. Available: https://www.ti.com/product/CC2520 (visited on 30/01/2023).

[136] V. Marsic, T. Amietszajew, P. Igic, S. Faramehr and J. Fleming, 'DC power line communication (PLC) on 868 MHz and 2.4 GHz wired RF transceivers,' *Sensors*, vol. 22, no. 5, p. 2043, 2022. DOI: 10.3390/s22052043.

[137] *SIG60: UART/LIN transceiver ic over DC power line*, 2022. [Online]. Available: https://yamar.com/product/sig60/ (visited on 30/01/2023).

[138] T. A. Vincent, B. Gulsoy, J. E. H. Sansom and J. Marco, 'A smart cell monitoring system based on power line communication—optimization of instrumentation and acquisition for smart battery management,' *IEEE Access*, vol. 9, pp. 161 773–161 793, 2021. DOI: 10.1109/access.2021.3131382.

[139] A. P. Talei, W. A. Pribyl and G. Hofer, 'Considerations for a power line communication system for traction batteries,' *e & i Elektrotechnik und Informationstechnik*, vol. 138, no. 1, pp. 3–14, 2021. DOI: 10.1007/s00502-020-00861-2.

[140] T. A. Vincent and J. Marco, 'Development of smart battery cell monitoring system and characterization on a small-module through in-vehicle power line communication,' *IEEE Access*, vol. 8, pp. 220 658–220 671, 2020. DOI: 10.1109/access.2020.3043657.

[141] T. F. Landinger, G. Schwarzberger and A. Jossen, 'A physical-based high-frequency model of cylindrical lithium-ion batteries for time domain simulation,' *IEEE Transactions on Electromagnetic Compatibility*, vol. 62, no. 4, pp. 1524–1533, Aug. 2020. DOI: 10.1109/temc.2020.2996414.

[142] A. P. Talie, W. A. Pribyl and G. Hofer, 'Electric vehicle battery management system using power line communication technique,' in *2018 14th Conference on Ph.D. Research in Microelectronics and Electronics (PRIME)*, IEEE, 2018. DOI: 10.1109/prime.2018.8430304.

[143] M. S. Alencar and V. C. da Rocha Jr., *Communication Systems*. Springer International Publishing, 2020. DOI: 10.1007/978-3-030-25462-9.

[144] L. L. Hanzo, S. X. Ng, T. Keller and W. Webb, 'Introduction and background,' in *Quadrature Amplitude Modulation*, IEEE, 2004. DOI: 10.1109/9780470010594.

[145] F. Xiong, *Digital Modulation Techniques, Second Edition (Artech House Telecommunications Library)*. Artech House Publishers, 2006, p. 1046, ISBN: 9781580538633.

[146] N. Benvenuto, *Principles of communications networks and systems*. Wiley, 2011, ISBN: 9780470744314.

[147] NI. 'The NI vector signal transceiver hardware architecture.' (17th Apr. 2023), [Online]. Available: https://www.ni.com/en-gb/support/documentation/supplemental/12/the-ni-vector-signal-transceiver-hardware-architecture.html (visited on 26/06/2023).

[148] M. Dörpinghaus, *On the Achievable Rate of Stationary Fading Channels*. Springer Berlin Heidelberg, 2011. DOI: 10.1007/978-3-642-19780-2.

[149] L. Hanzo and T. Keller, *OFDM and MC-CDMA, A Primer*. Wiley-IEEE Press, 2006, p. 430, ISBN: 9780470030073.

[150] I. Collins, 'Phase-locked loop (PLL) fundamentals,' *AnalogDialogue*, 2018. [Online]. Available: Phase-Locked%20Loop%20(PLL)%20Fundamentals.

[151] J. V. Stone, *Information Theory A Tutorial Introduction, A Tutorial Introduction*. Sebtel Press, 2015, p. 260, ISBN: 9780956372857.

[152] M. A. Bhagyaveni, R. Kalidoss and K. S. Vishvaksenan, *Introduction to Analog and Digital Communication*. River Publishers, 2022, ISBN: 9781000795172.

[153] A. G. Merkulov, Y. P. Shkarin, S. E. Romanov, V. A. Kharlamov and Y. V. Nazarov, *High Voltage Digital Power Line Carrier Channels*. Springer International Publishing, 2021. DOI: 10.1007/978-3-030-58365-1.

[154] N. Meddings, M. Heinrich, F. Overney *et al.*, 'Application of electrochemical impedance spectroscopy to commercial li-ion cells: A review,' *Journal of Power Sources*, vol. 480, p. 228 742, Dec. 2020. DOI: 10.1016/j.jpowsour.2020.228742.

[155] P. Iurilli, C. Brivio and V. Wood, 'On the use of electrochemical impedance spectroscopy to characterize and model the aging phenomena of lithium-ion batteries: A critical review,' *Journal of Power Sources*, vol. 505, p. 229 860, Sep. 2021. DOI: 10.1016/j.jpowsour.2021.229860.

[156] Autolab Application Note EC08, 'Basic overview of the working principle of a potentiostat/galvanostat (pgstat) - electrochemical cell setup,' *Metrohm Autolab. BV*, pp. 1–3, 2011.

[157] A. C. Lazanas and M. I. Prodromidis, 'Electrochemical impedance spectroscopy-a tutorial,' *ACS Measurement Science Au*, vol. 3, no. 3, pp. 162–193, Mar. 2023. DOI: 10.1021/acsmeasuresciau.2c00070.

[158] T. Dobbelaere, P. M. Vereecken and C. Detavernier, 'A USB-controlled potentiostat/galvanostat for thin-film battery characterization,' *HardwareX*, vol. 2, pp. 34–49, 2017. DOI: 10.1016/j.ohx.2017.08.001.

[159] D. Andre, M. Meiler, K. Steiner, C. Wimmer, T. Soczka-Guth and D. Sauer, 'Characterization of high-power lithium-ion batteries by electrochemical impedance spectroscopy. i. experimental investigation,' *Journal of Power Sources*, vol. 196, no. 12, pp. 5334–5341, Jun. 2011. DOI: 10.1016/j.jpowsour.2010.12.102.

[160] Rohde & Schwarz, *ZNA user manual*, version 23, 2022.

[161] P. J. Pupalaikis, *S-Parameters for Signal Integrity*. Cambridge University Press, Jan. 2020. DOI: 10.1017/9781108784863.

[162] 3GPP, 'Technical specification group radio access network; nr; user equipment (ue) radio transmission and reception; part 2: Range 2 standalone (release 17),' 3rd Generation Partnership Project (3GPP), Technical Specification (TS) 38.101-2, 2022, Version 17.5.0. [Online]. Available: https://www.3gpp.org/ftp/Specs/archive/38_series/38.101-2/38101-2-h50.zip.

[163] National Instruments Corporation, *NI RFmx Demod 21.3 manual*, Oct. 2021.

[164] National Instruments Corporation, *NI RFSG 21.3 manual*, Oct. 2021.

[165] P. S. Sausen, A. Sausen, M. D. Campos, L. F. Sauthier, A. C. Oliveira and R. R. E. Junior, 'Power line communication applied in a typical brazilian urban power network,' *IEEE Access*, vol. 9, pp. 72 844–72 856, 2021. DOI: 10.1109/access.2021.3078697.

[166] M. F. Niri, T. M. Bui, T. Q. Dinh, E. Hosseinzadeh, T. F. Yu and J. Marco, 'Remaining energy estimation for lithium-ion batteries via gaussian mixture and markov models for future load prediction,' *Journal of Energy Storage*, vol. 28, p. 101 271, 2020. DOI: 10.1016/j.est.2020.101271.

[167] C. Jiaqi, A. R. Ruddle and Y. X. Teo, 'Predicting the RF impedance of cells in series for automotive traction battery applications,' in *2017 International Symposium on Electromagnetic Compatibility - EMC EUROPE*, IEEE, 2017, pp. 1–6. DOI: 10.1109/emceurope.2017.8094621.

[168] Y. X. Teo, J. Chen and A. R. Ruddle, 'Predicting the RF impedance of cells in parallel for automotive traction battery applications,' in *2019 International Symposium on Electromagnetic Compatibility - EMC EUROPE*, IEEE, 2019, pp. 438–443. DOI: 10.1109/emceurope.2019.8871903.

[169] F. J. Cañete, K. Dostert, S. Galli *et al.*, *Power Line Communications, Noise and Interferences*. Wiley, Apr. 2016, ch. Channel Characterization, pp. 152–154. DOI: 10.1002/9781118676684.

[170] P. Gallion, 'Basics of incoherent and coherent digital optical communications,' in *Undersea Fiber Communication Systems*, Elsevier, 2016, pp. 55–117. DOI: 10.1016/b978-0-12-804269-4.00003-9.

[171] IEEE, *IEEE standard for broadband over power line networks: Medium access control and physical layer specifications*, 2020. DOI: 10.1109/ieeestd.2021.9329263.

[172] V. A. Marcis, A. Praneeth, L. Patnaik and S. S. Williamson, 'Analysis of CT-CV charging technique for lithium-ion and NCM 18650 cells over temperature range,' in *2020 IEEE International Conference on Industrial Technology (ICIT)*, IEEE, 2020. DOI: 10.1109/icit45562.2020.9067186.

[173] H. A. Latchman, S. Katar, L. W. Yonge and S. Gavette, *Homeplug AV and IEEE 1901*. John Wiley & Sons, Inc., Mar. 2013. DOI: 10.1002/9781118527535.

[174] KiCad Development Team. 'Kicad EDA, Schematic capture & PCB design software.' (15th Dec. 2022), [Online]. Available: https://www.kicad.org/ (visited on 15/12/2022).

Appendix A

Source Code

The source code for the circuits and the programs developed during this research are embedded as attachments in this PDF. Accessing these files requires a compatible PDF reader, such as Firefox 107. The files may be found in the list of attachments or by clicking on the red hyperlinks below. Additionally, these files can be downloaded from the Warwick Research Archive Portal at https://wrap.warwick.ac.uk.

A.1 Series-through Lithium-ion Cell Holder

Click on the following link or find the attached file named cell-holder-series.zip. The project files are compatible with KiCad 6.0.5 [174]. The terms of use and distribution are included in the LICENCE file within the archive.

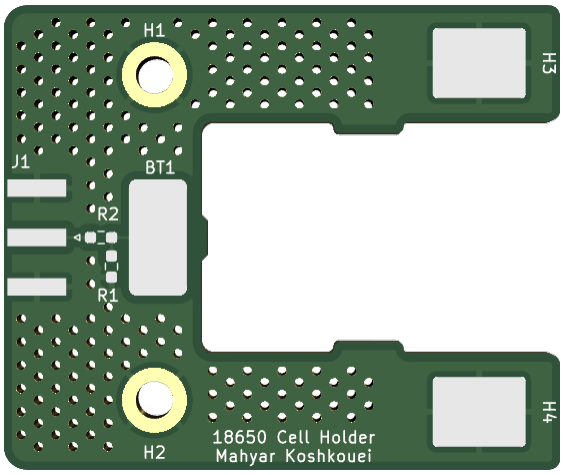

Figure A.1: Preview of Li-ion series-through cell holder layout in KiCad. Used in Chapter 5.

A.2 Shunt-through Lithium-ion Cell Holder

Click on the following link or find the attached file named cell-holder-shunt.zip. The project files are compatible with KiCad 6.0.5 [174]. The terms of use and distribution are included in the LICENCE file within the archive.

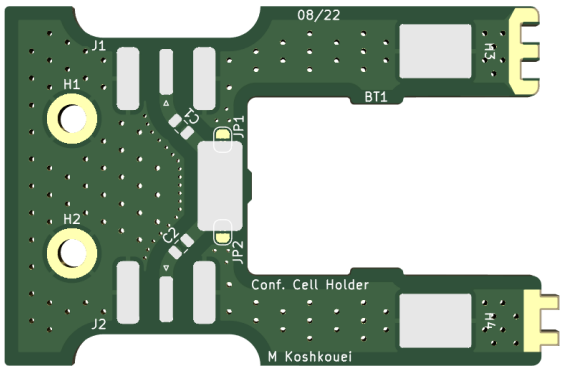

Figure A.2: Preview of Li-ion shunt-through cell holder layout in KiCad. Used in Chapter 6.

A.3 Program for testing PLC QAM using NI PXIe-5840 VST

This program was exclusively written for this research and used in Chapters 5 and 6 to output data modulated with quadrature amplitude modulation (QAM) to test power line communication (PLC) through Li-ion cells, using a NI PXIe-5840 vector signal transceiver (VST). This program requires proprietary libraries from NI, including NI RFSG, and NI RFmx. The Microsoft Visual Studio 2022 project file is included and has these library dependencies configured. The functions used in this program may not be compatible with other VSTs. The terms of use and distribution are included in the LICENCE file within the archive.

Click on the following link or find the attached file named QAM-VST-Error.zip.